



**A SIMPLE MODEL FOR FINE STRUCTURE
TRANSITIONS IN ALKALI-METAL
NOBLE-GAS COLLISIONS**

THESIS

Joseph A. Cardoza, Captain, USAF
AFIT-ENP-MS-15-M-079

**DEPARTMENT OF THE AIR FORCE
AIR UNIVERSITY**

AIR FORCE INSTITUTE OF TECHNOLOGY

Wright-Patterson Air Force Base, Ohio

**DISTRIBUTION STATEMENT A
APPROVED FOR PUBLIC RELEASE; DISTRIBUTION UNLIMITED.**

The views expressed in this document are those of the author and do not reflect the official policy or position of the United States Air Force, the United States Department of Defense or the United States Government. This material is declared a work of the U.S. Government and is not subject to copyright protection in the United States.

AFIT-ENP-MS-15-M-079

A SIMPLE MODEL FOR FINE STRUCTURE TRANSITIONS IN
ALKALI-METAL NOBLE-GAS COLLISIONS

THESIS

Presented to the Faculty
Department of Engineering Physics
Graduate School of Engineering and Management
Air Force Institute of Technology
Air University
Air Education and Training Command
in Partial Fulfillment of the Requirements for the
Degree of Master of Science in Applied Physics

Joseph A. Cardoza, BS
Captain, USAF

March 2015

DISTRIBUTION STATEMENT A
APPROVED FOR PUBLIC RELEASE; DISTRIBUTION UNLIMITED.

AFIT-ENP-MS-15-M-079

A SIMPLE MODEL FOR FINE STRUCTURE TRANSITIONS IN
ALKALI-METAL NOBLE-GAS COLLISIONS

Joseph A. Cardoza, BS
Captain, USAF

Committee Membership:

Dr. D. E. Weeks
Chair

Dr. G. P. Perram
Member

Abstract

From ranging and tracking applications, to directed energy weapons, laser technology is very important to the military. An instrumental part of laser design and characterization depends on knowledge of transition rates between various atomic energy levels. Of specific interest, is determining the transition probabilities between the $^2P_{3/2}$ and $^2P_{1/2}$ energy levels of an alkali-metal noble-gas laser, which is found in a DPAL. The probabilities of transition, caused by collisions between alkali metal and noble gas atoms, have previously been calculated using a computationally intensive quantum mechanical model. This research project aims to develop a simplified, less intensive method. This is accomplished through the use of a semi-classical approach, where the colliding atoms are modeled as having a classical, straight-line trajectory. The transition probabilities are then calculated using time-dependent perturbation theory, where the coupling between states is obtained by expressing the diabatic coupling potential as a function of time. Numerical solutions to the time-dependent perturbation equations are obtained for various forms of coupling and are compared with an approximate analytic solution.

Acknowledgements

I would sincerely like to thank my advisor, Dr. Weeks, for all of his help throughout this project. Many of the ideas in this thesis, including the topic itself, stem from his extensive collection of personal notes. He has provided many hours of his time, sharing his expertise both to assist me in finding the path most likely to succeed, as well as just to help me gain a deeper understanding of the many complex details underlying this project. This work would not have been possible without his guidance.

Joseph A. Cardoza

Table of Contents

	Page
Abstract	iv
Acknowledgements	v
List of Figures	viii
List of Tables	xi
List of Abbreviations	xii
I. Introduction	1
II. Theory	4
2.1 The Hamiltonian for a Two-Atom Interaction	4
2.2 The Diabatic Basis	6
2.3 The Adiabatic Basis and Potential Energy Surfaces	9
2.4 Adiabatic-Diabatic Transformation and Diabatic Potential Energy Surfaces	9
2.5 Semi-Classical Model for the Probability of Transition for a Single Atom	12
2.6 Time-Dependent Perturbation Theory	15
2.7 Determining Transition Rates and Probabilities	17
2.8 Approximations of the Radial Coupling Function, $V(R)$	19
2.9 Adiabaticity	24
2.10 Analytic Approximation of Transition Probability	25
III. Procedure and Numerical Methods	28
3.1 Numerical Systems	28
3.2 Selection of Method of Quadrature	30
3.3 Multivariable Quadrature - Optimization and Numerical Integration of the Rate Equation	36
3.4 Determining the Limits of Integration	40
3.5 Calculations Using $V_{RG}(t)$ and the Analytic Form of the Rate Equation	42
3.6 Special Considerations for Integration When Using $V_{QM}(R)$	42
IV. Results	46
4.1 Results Overview	46
4.2 Constants and Approximation Parameters	46

	Page
4.3 Comparison of Numerically Integrated $V_{RG}(t)$ and Analytic $V_{RG}(t)$	48
4.4 Comparison of Numerically Integrated $V_{RG}(t)$ and Numerically Integrated $V_{RG}(R)$	51
4.5 Comparison of Numerically Integrated Rectangular-Gaussian $V_{RG}(R)$ and Numerically Integrated Quantum Mechanical $V_{QM}(R)$	51
V. Discussion	57
5.1 Comparison with Experimental Data - Support for Validity of Potential Energy Surfaces	57
5.2 Choice of Energy Level for Conservation of Energy in $V_{QM}(R)$	57
5.3 Scaling V_0 , L , and W to Make the Numerical Results for $V_{RG}(R)$ Match Experimental Results	62
VI. Conclusion	75
6.1 Conclusion	75
Bibliography	78

List of Figures

Figure		Page
1	4-level RbHe diabatic potential energy surfaces related to the corresponding 3-level Rb surfaces	2
2	3-Level Adiabatic potential energy surfaces for RbHe	10
3	3-Level Diabatic potential energy surfaces for RbHe	11
4	Alkali-Metal and Noble-Gas Classical Collision Model	12
5	Coupling function.....	15
6	Rectangular Gaussian Approximation, $V_{RG}(R)$	20
7	Rectangular Gaussian Approximation, $V_{RG}(t)$	21
8	Rectangular Gaussian Approximation, $V_{RG}(t)$, with $v = \frac{1}{2}\bar{v}$	22
9	Rectangular Gaussian Approximation, $V_{RG}(t)$, with $v = 2\bar{v}$	23
10	Adiabaticity for Various Velocities and Temperatures of RbHe - Constant Time Scaling	25
11	Adiabaticity for Various Velocities and Temperatures of RbHe - Variable Time Scaling	26
12	Trapezoidal Rule and Romberg Method Convergence - Single Precision	31
13	Trapezoidal Rule and Romberg Method Convergence - Double Precision	32
14	Verification of Limits and Convergence Across Impact Parameters	43
15	Verification of Limits and Convergence Across Velocities	44
16	Radial Coupling Functions $V_{QM}(R)$ and Approximations $V_{RG}(R)$, All Atomic Species	47
17	Ln(Probability) vs Adiabaticity, Analytic vs. Numeric $V_{RG}(t)$, K.....	49

Figure		Page
18	Ln(Probability) vs Adiabaticity, Analytic vs. Numeric $V_{RG}(t)$, Rb	50
19	Ln(Probability) vs Adiabaticity, Analytic vs. Numeric $V_{RG}(t)$, Cs	50
20	Ln(Probability) vs Adiabaticity, Numeric $V_{RG}(t)$ vs. Numeric $V_{RG}(R)$, K	52
21	Ln(Probability) vs Adiabaticity, Numeric $V_{RG}(t)$ vs. Numeric $V_{RG}(R)$, Rb	52
22	Ln(Probability) vs Adiabaticity, Numeric $V_{RG}(t)$ vs. Numeric $V_{RG}(R)$, Cs	53
23	Ln(Probability) vs Adiabaticity, Numeric $V_{RG}(R)$ vs. Numeric $V_{QM}(R)$, K	54
24	Ln(Probability) vs Adiabaticity, Numeric $V_{RG}(R)$ vs. Numeric $V_{QM}(R)$, Rb	54
25	Ln(Probability) vs Adiabaticity, Numeric $V_{RG}(R)$ vs. Numeric $V_{QM}(R)$, Cs	55
26	Ln(Probability) vs Adiabaticity, Numeric $V_{RG}(R)$ with Energy Conservation	56
27	Ln(Probability) vs Adiabaticity, Numeric $V_{RG}(R)$ vs. Experiment and Full Quantum Approach, K	58
28	Ln(Probability) vs Adiabaticity, Numeric $V_{RG}(R)$ vs. Experiment and Full Quantum Approach, Rb	58
29	Ln(Probability) vs Adiabaticity, Numeric $V_{RG}(R)$ vs. Experiment and Full Quantum Approach, Cs	59
30	Conservation of Energy and Turning Points	60
31	Resulting Transition Probabilities for Various Choices of Conserved Energy Level	61
32	$V_{RG}(R)$ Radial Coupling Function with Scaled Fit Parameter, V_0	63
33	Effect of Scaling the $V_{RG}(R)$ Radial Coupling Fit Parameter, V_0 , for KHe, KNe, and KAr	64

Figure		Page
34	Effect of Scaling the $V_{RG}(R)$ Radial Coupling Fit Parameter, V_0 , for RbHe, RbNe, and RbAr	64
35	Effect of Scaling the $V_{RG}(R)$ Radial Coupling Fit Parameter, V_0 , for CsHe, CsNe, and CsAr	65
36	Effect of Scaling the $V_{RG}(R)$ Radial Coupling Fit Parameter, V_0 , for All M+Ng Pairs	66
37	$V_{RG}(R)$ Radial Coupling Function with Scaled Fit Parameter, L	67
38	Effect of Scaling the $V_{RG}(R)$ Radial Coupling Fit Parameter, L , for KHe, KNe, and KAr	68
39	Effect of Scaling the $V_{RG}(R)$ Radial Coupling Fit Parameter, L , for RbHe, RbNe, and RbAr	68
40	Effect of Scaling the $V_{RG}(R)$ Radial Coupling Fit Parameter, L , for CsHe, CsNe, and CsAr	69
41	Effect of Scaling the $V_{RG}(R)$ Radial Coupling Fit Parameter, L , for All M+Ng Pairs	70
42	$V_{RG}(R)$ Radial Coupling Function with Scaled Fit Parameter, W	71
43	Effect of Scaling the $V_{RG}(R)$ Radial Coupling Fit Parameter, W , for KHe, KNe, and KAr	72
44	Effect of Scaling the $V_{RG}(R)$ Radial Coupling Fit Parameter, W , for RbHe, RbNe, and RbAr	72
45	Effect of Scaling the $V_{RG}(R)$ Radial Coupling Fit Parameter, W , for CsHe, CsNe, and CsAr	73
46	Effect of Scaling the $V_{RG}(R)$ Radial Coupling Fit Parameter, W , for All M+Ng Pairs	74
47	Ln(Probability) vs Adiabaticity - All Methods and All M+Ng Pairs	76

List of Tables

Table		Page
1	Standard values for floating point number representation	29
2	Summary of Calculations Completed and Data Compiled	46
3	Atomic constants and approximations	48
4	Values of Approximation Parameter X_{max}	49

List of Abbreviations

Abbreviation	Page
COIL	Chemical Oxygen Iodine Laser 1
ABL	Airborne Laser 1
DPAL	Diode-Pumped Alkali Laser 1
M	Alkali Metal 4
Ng	Noble Gas 4

A SIMPLE MODEL FOR FINE STRUCTURE TRANSITIONS IN ALKALI-METAL NOBLE-GAS COLLISIONS

I. Introduction

Lasers have been of great interest to the Air Force for many years, with applications including ranging, tracking, targeting, high power laser weapons, and countermeasures. These lasers can generally be broken down into two broad categories based on the lasing medium. These categories are solid state and gas phase. Current gas phase lasers tend to have the benefits of higher beam quality and better thermal properties (heat dissipation), as compared to solid state lasers. Historically, gas phase lasers have been pumped by chemical reactions, such as in the Chemical Oxygen Iodine Laser (COIL). The COIL was invented by the Air Force Weapons Laboratory (now Air Force Research Laboratory) in 1977, and was used aboard the Airborne Laser (ABL).

Current gas-phase laser research interests include the Diode-Pumped Alkali Laser (DPAL), which has the advantage of being electrically pumped by diode lasers. This allows the DPAL to be much smaller, lighter, and less complex than the COIL. A DPAL primarily consists of a gas chamber, a laser diode pump, and mirrors and other optics. The gas within the chamber consists primarily of a noble gas, such as helium, along with a relatively small amount of an evaporated alkali metal, such as rubidium. It is commonly a three-state laser system, where arrays of diode lasers pump electrons in the alkali metal atoms from the ground atomic energy level, $^2S_{1/2}$, to the $^2P_{3/2}$ excited atomic energy level (see right side of Figure 1). Through collisions

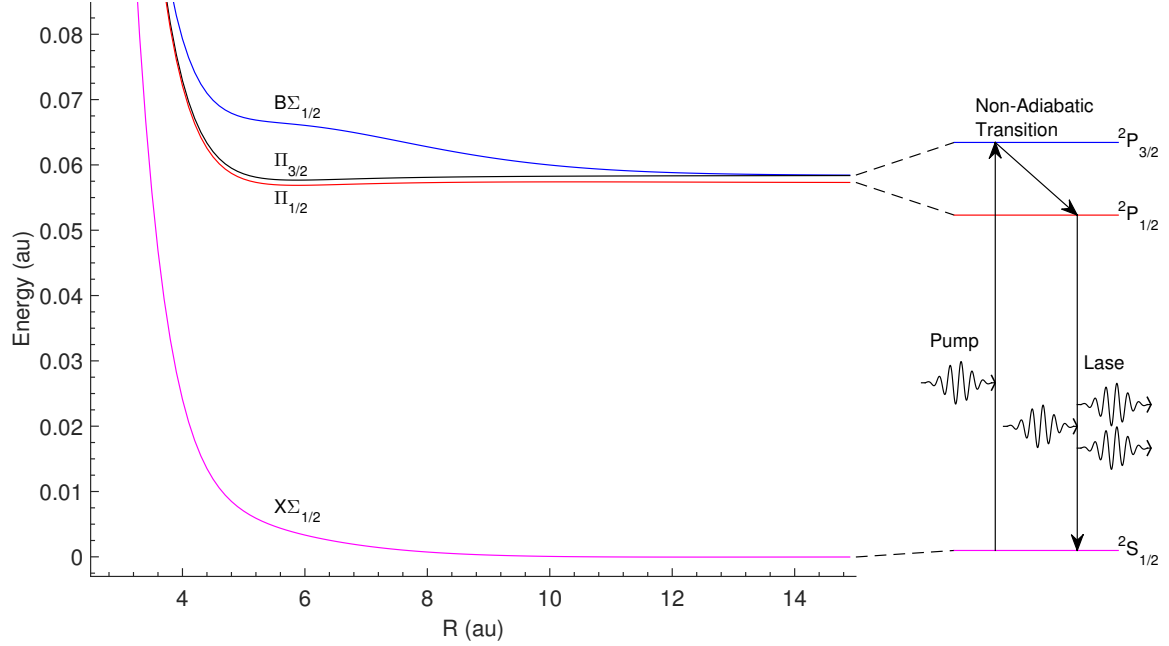


Figure 1. Adiabatic potential energy surfaces for RbHe.

with the noble gas buffer atoms, the excited electrons in the alkali metal relax to the $^2P_{1/2}$ level, creating a population inversion between the $^2P_{1/2}$ and the $^2S_{1/2}$ levels.

This thesis focuses on the collisional de-excitation of alkali metal atoms in a gas-phase lasing medium. As the evaporated metal and noble gas atoms approach each other during a collision, the energy levels of the atoms undergo a complex interaction. The alkali metal's atomic energy levels, which are constant in the asymptotic limit (at large atomic separations), become varying functions of the atomic separation (R), as shown on the left side of Figure 1.

A key requirement for developing and characterizing laser technology is knowledge of the transition rates of electrons between their various atomic energy levels. Unfortunately, a direct analytic approach to determine these rates quickly becomes too complicated to solve exactly for all but the simplest systems. In response to this challenge, numerical techniques have been developed to solve more complicated systems, however these methods are computationally intensive. For this project, a

semi-classical model that is intended to reduce the computational overhead is designed. The system consists of a collision between a noble gas atom and an alkali metal atom, and is intended to describe the collisional de-excitation in a gas-phase laser. The simplified semi-classical model used approximates the dynamics of the noble gas atom using a straight line trajectory, and leads to the development of a multivariable rate integral which is then used to determine fine-structure transition rates of the alkali atoms. The integration of this integral is primarily performed numerically, using an adaptive Romberg integration routine written in C. An analytic approximation of the transition rate integral is also described and compared to the numeric methods.

Previous work on the fine structure transitions of alkali atoms as they collide with noble gas atoms includes a full quantum mechanical calculation of transition rates based on wave packet propagation on potential energy surfaces [5]. Comparisons with these full quantum mechanical calculations as well as comparisons with experimental results, facilitated by a compilation of experimental data [3], will be used to check the validity of the simplified model.

II. Theory

2.1 The Hamiltonian for a Two-Atom Interaction

The Hamiltonian that governs the dynamics of the Alkali Metal (M) + Noble Gas (Ng) system is given by

$$\hat{H} = \hat{T}_{N_{\text{rad}}} + \hat{T}_{N_{\text{ang}}} + \hat{T}_e + \hat{V}_{NN} + \hat{V}_{eN} + \hat{V}_{ee} + \hat{V}_{SO} \quad (1)$$

The individual terms of this Hamiltonian are:

- Nuclear Radial Kinetic Energy

$$\hat{T}_{N_{\text{rad}}} = \frac{\hat{P}_R^2}{2\mu_{MN_g}} \quad (2)$$

where \hat{P}_R is the radial momentum operator conjugate to the internuclear separation $R = |\vec{R}_M - \vec{R}_{Ng}|$, and μ_{MN_g} is the nuclear reduced mass.

- Nuclear Angular Kinetic Energy

$$\hat{T}_{N_{\text{ang}}} = \frac{\hat{L}^2}{2\mu_{MN_g} |\vec{R}_M - \vec{R}_{Ng}|^2} \quad (3)$$

where \hat{L} is the angular momentum operator, and \vec{R}_M and \vec{R}_{Ng} are the nuclear position vectors for the alkali metal and noble gas respectively.

- Electronic Kinetic Energy

$$\hat{T}_e = \sum_{i=1}^{Z_M+Z_{Ng}} \frac{\hat{P}_i^2}{2m_e} \quad (4)$$

where Z is the atomic number, and m_e is the mass of the electron.

- Nuclear-Nuclear Potential Energy

$$\hat{V}_{NN} = \frac{e^2}{4\pi\epsilon_0} \frac{Z_M Z_{Ng}}{\left| \vec{R}_M - \vec{R}_{Ng} \right|} \quad (5)$$

where e is the magnitude of the electron charge, and ϵ_0 is the permittivity of free space

- Electronic-Nuclear Potential Energy

$$\hat{V}_{eN} = - \sum_{i=1}^{Z_M+Z_{Ng}} \frac{e^2}{4\pi\epsilon_0} \left(\frac{Z_M}{\left| \vec{R}_M - \vec{r}_i \right|} + \frac{Z_{Ng}}{\left| \vec{R}_{Ng} - \vec{r}_i \right|} \right) \quad (6)$$

where lower case \vec{r} denote electronic position vectors.

- Electronic-Electronic Potential Energy

$$\hat{V}_{ee} = \sum_{i>j}^{Z_M+Z_{Ng}} \frac{e^2}{4\pi\epsilon_0} \frac{1}{\left| \vec{r}_i - \vec{r}_j \right|} \quad (7)$$

- Electron Spin Orbit Coupling

$$\hat{V}_{SO} = \xi(r) \hat{\ell} \cdot \hat{s} \quad (8)$$

where ξ is the spin-orbit coupling function, $\hat{\ell}$ is the electron's orbital angular momentum, and \hat{s} is the electron's spin angular momentum.

The Hamiltonian can be simplified by defining the following combination of terms,

$$\hat{H}_{MNg} \equiv \hat{T}_e + \hat{V}_{NN} + \hat{V}_{eN} + \hat{V}_{ee} \quad (9)$$

which leaves the simplified form of the Hamiltonian for the M+Ng interaction as

$$\hat{H} = \hat{T}_{N_{\text{rad}}} + \hat{T}_{N_{\text{ang}}} + \hat{H}_{MNg} + \hat{V}_{SO} \quad (10)$$

2.2 The Diabatic Basis

The diabatic basis is a mixed representation consisting of the radial coordinate and the angular momentum,

$$\left| \begin{array}{cc} R & J \quad j \\ & \Omega \quad \omega \end{array} \right\rangle \quad (11)$$

where R is the internuclear separation, J is the total angular momentum, Ω is the projection of J onto the internuclear axis, j is the electronic angular momentum, and ω is the projection of j onto the internuclear axis. The $^2P_{3/2}$ and $^2P_{1/2}$ alkali atom energy levels correspond to a total of six eigenstates in this basis. With R omitted for clarity, the eigenstates are

$$^2P_{1/2} \Rightarrow \left\{ \begin{array}{l} \left| \begin{array}{cc} J & 1/2 \\ 1/2 & 1/2 \end{array} \right\rangle \\ \left| \begin{array}{cc} J & 1/2 \\ -1/2 & -1/2 \end{array} \right\rangle \end{array} \right. \quad ^2P_{3/2} \Rightarrow \left\{ \begin{array}{l} \left| \begin{array}{cc} J & 3/2 \\ 3/2 & 3/2 \end{array} \right\rangle \\ \left| \begin{array}{cc} J & 3/2 \\ 1/2 & 1/2 \end{array} \right\rangle \\ \left| \begin{array}{cc} J & 3/2 \\ -1/2 & -1/2 \end{array} \right\rangle \\ \left| \begin{array}{cc} J & 3/2 \\ -3/2 & -3/2 \end{array} \right\rangle \end{array} \right. \quad (12)$$

For the M+Ng system considered here, $\Omega = \omega$ in each of these eigenstates. This is because the projection of the orbital nuclear angular momentum onto the internuclear axis is zero ($\hat{J} = \hat{L} + \hat{j}$, $J_z = L_z + j_z = j_z$, with $L_z = 0$).

Since there are six basis vectors, the matrix representation of the Hamiltonian in this basis will yield a 6×6 matrix. Fortunately, this 6×6 matrix is approximately block diagonal with two 3×3 blocks [5]. These blocks separate the positive and negative values of $\Omega = \omega$, and only one of these needs to be considered (see [5] for the full 6×6 matrix representation). Considering only the three basis vectors having positive momentum projections, the 3×3 matrix representations of the terms of the M+Ng Hamiltonian in Equation 10 are given by

$$\mathbb{T}_{N_{\text{rad}}} = \frac{-\hbar^2}{2\mu_{MNg}} \begin{matrix} \left\langle \begin{matrix} J & 3/2 \\ 3/2 & 3/2 \end{matrix} \right| & \left\langle \begin{matrix} J & 3/2 \\ 1/2 & 1/2 \end{matrix} \right| & \left\langle \begin{matrix} J & 1/2 \\ 1/2 & 1/2 \end{matrix} \right| \end{matrix} \begin{bmatrix} \frac{d^2}{dR^2} & 0 & 0 \\ 0 & \frac{d^2}{dR^2} & 0 \\ 0 & 0 & \frac{d^2}{dR^2} \end{bmatrix} \begin{matrix} \left| \begin{matrix} J & 3/2 \\ 3/2 & 3/2 \end{matrix} \right\rangle \\ \left| \begin{matrix} J & 3/2 \\ 1/2 & 1/2 \end{matrix} \right\rangle \\ \left| \begin{matrix} J & 1/2 \\ 1/2 & 1/2 \end{matrix} \right\rangle \end{matrix} \quad (13)$$

$$\begin{aligned}
\mathbb{T}_{N_{\text{ang}}} &= \frac{-\hbar^2}{2\mu_{MNg}R^2} \begin{matrix} & \left| \begin{matrix} J & 3/2 \\ 3/2 & 3/2 \end{matrix} \right\rangle & \left| \begin{matrix} J & 3/2 \\ 1/2 & 1/2 \end{matrix} \right\rangle & \left| \begin{matrix} J & 1/2 \\ 1/2 & 1/2 \end{matrix} \right\rangle \\ \left\langle \begin{matrix} J & 3/2 \\ 3/2 & 3/2 \end{matrix} \right| & \left[\begin{array}{ccc} J(J+1) - \frac{3}{4} & -[3(J - \frac{1}{2})(J + \frac{3}{2})]^{1/2} & 0 \\ -[3(J - \frac{1}{2})(J + \frac{3}{2})]^{1/2} & J(J+1) + \frac{13}{4} & 0 \\ 0 & 0 & J(J+1) + \frac{3}{4} \end{array} \right] \\ \left\langle \begin{matrix} J & 3/2 \\ 1/2 & 1/2 \end{matrix} \right| & \\ \left\langle \begin{matrix} J & 1/2 \\ 1/2 & 1/2 \end{matrix} \right| & \end{matrix}
\end{aligned}
\tag{14}$$

(using the fact that $\hat{L} = \hat{J} - \hat{j}$ and $\hat{L}^2 = \hat{J}^2 + \hat{j}^2 - 2\hat{J} \cdot \hat{j}$).

$$\begin{aligned}
\mathbb{H}_{MNg} + \mathbb{V}_{SO} &= \begin{matrix} & \left| \begin{matrix} J & 3/2 \\ 3/2 & 3/2 \end{matrix} \right\rangle & \left| \begin{matrix} J & 3/2 \\ 1/2 & 1/2 \end{matrix} \right\rangle & \left| \begin{matrix} J & 1/2 \\ 1/2 & 1/2 \end{matrix} \right\rangle \\ \left\langle \begin{matrix} J & 3/2 \\ 3/2 & 3/2 \end{matrix} \right| & \left[\begin{array}{ccc} \Pi + \frac{\xi}{2} & 0 & 0 \\ 0 & \frac{1}{3}(2\Sigma + \Pi) + \frac{\xi}{2} & -\frac{\sqrt{2}}{3}(\Sigma - \Pi) \\ 0 & -\frac{\sqrt{2}}{3}(\Sigma - \Pi) & \frac{1}{3}(\Sigma + 2\Pi) - \xi \end{array} \right] \\ \left\langle \begin{matrix} J & 3/2 \\ 1/2 & 1/2 \end{matrix} \right| & \\ \left\langle \begin{matrix} J & 1/2 \\ 1/2 & 1/2 \end{matrix} \right| & \end{matrix}
\end{aligned}
\tag{15}$$

2.3 The Adiabatic Basis and Potential Energy Surfaces

The adiabatic basis vectors corresponding to the $^2P_{1/2}$ and $^2P_{3/2}$ atomic energy levels are given by

$$P_{1/2} \Rightarrow \left\{ \begin{array}{c} |\Pi_{1/2}\rangle \end{array} \right. \quad P_{3/2} \Rightarrow \left\{ \begin{array}{c} |\Sigma_{1/2}\rangle \\ |\Pi_{3/2}\rangle \end{array} \right. \quad (16)$$

In this basis, the 3×3 matrix representation of the electronic M+Ng Hamiltonian is given by the diagonal matrix

$$\mathbb{H}_{MNg} + \mathbb{V}_{SO} = \begin{array}{c} \langle \Pi_{3/2} | \\ \langle \Sigma_{1/2} | \\ \langle \Pi_{1/2} | \end{array} \begin{array}{c} |\Pi_{3/2}\rangle \quad |\Sigma_{1/2}\rangle \quad |\Pi_{1/2}\rangle \\ \left[\begin{array}{ccc} \Pi_{3/2} & 0 & 0 \\ 0 & \Sigma_{1/2} & 0 \\ 0 & 0 & \Pi_{1/2} \end{array} \right] \end{array} \quad (17)$$

Because there are no off-diagonal terms in this matrix, the adiabatic electronic M+Ng Hamiltonian does not contribute to mixing between eigenstates. The components of this matrix have been previously calculated using a many-body numerical approach [1] to yield adiabatic electronic potential energy surfaces, shown for RbHe in Figure 2. Note that these are the upper states from the surfaces shown in Figure 1 for a DPAL.

2.4 Adiabatic-Diabatic Transformation and Diabatic Potential Energy Surfaces

As stated, the potential energy surfaces have been calculated in the adiabatic basis [1], but the time-dependent perturbation theory method that will be used requires

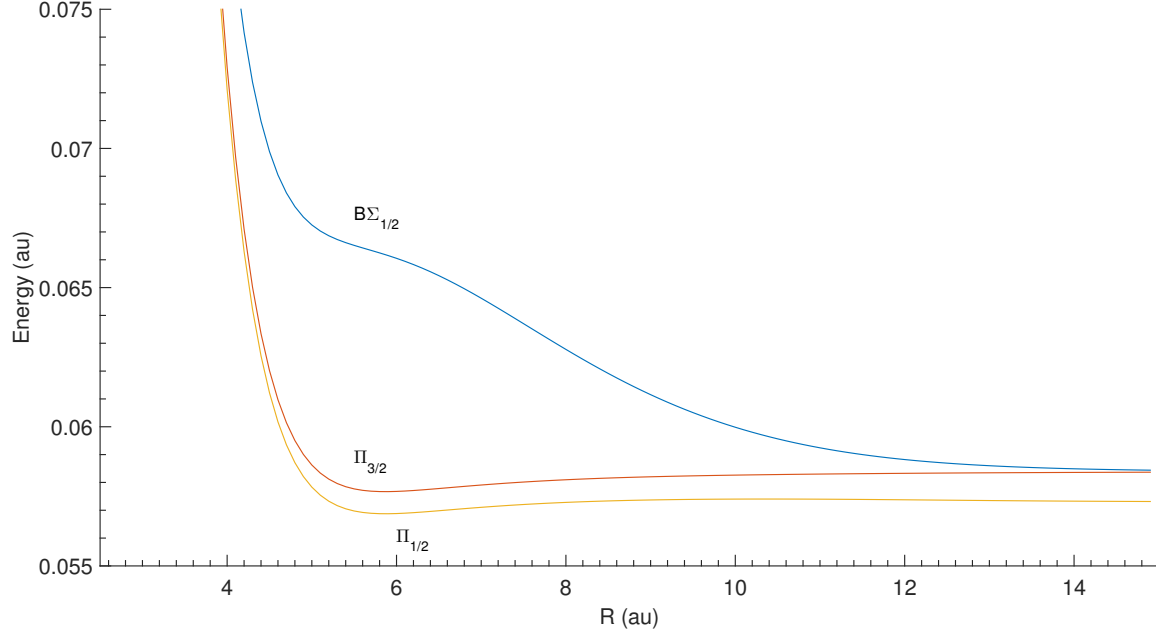


Figure 2. Adiabatic potential energy surfaces for RbHe.

the electronic Hamiltonian to be represented in the diabatic basis. What is required is a unitary adiabatic-diabatic transformation, such that

$$\mathbb{H}_{\text{diabatic}} = \mathbb{U}^\dagger \mathbb{H}_{\text{adiabatic}} \mathbb{U} \quad (18)$$

where \mathbb{U} is the unitary adiabatic-diabatic transformation matrix. This transformation is found in [5] by diagonalizing $\mathbb{H}_{\text{diabatic}}$ to find its eigenvectors, then matching those eigenvectors to the diagonal elements of $\mathbb{H}_{\text{adiabatic}}$. This gives the elements of $\mathbb{H}_{\text{adiabatic}}$ in terms of the diagonalized elements of $\mathbb{H}_{\text{diabatic}}$ as

$$\begin{aligned} \Pi_{3/2} &= \Pi + \frac{\xi}{2} \\ \Sigma_{1/2} &= \frac{1}{4} \left(-\xi + 2(\Sigma + \Pi) + \sqrt{9\xi^2 + 4\xi(\Sigma - \Pi) + 4(\Sigma - \Pi)^2} \right) \\ \Pi_{1/2} &= \frac{1}{4} \left(-\xi + 2(\Sigma + \Pi) - \sqrt{9\xi^2 + 4\xi(\Sigma - \Pi) + 4(\Sigma - \Pi)^2} \right) \end{aligned} \quad (19)$$

These solutions are then inverted to obtain the diabatic electronic Hamiltonian (given by Equation 15) in terms of the known adiabatic electronic Hamiltonian eigenvalues.

The transformations are

$$\begin{aligned}
\Sigma &= \frac{2\Pi_{1/2} - \Pi_{3/2} + 2\Sigma_{1/2}}{3} + \frac{1}{3} \sqrt{\Pi_{1/2}^2 + 2\Pi_{1/2}\Pi_{3/2} - 2\Pi_{3/2}^2 - 4\Pi_{1/2}\Sigma_{1/2} + 2\Pi_{3/2}\Sigma_{1/2} + \Sigma_{1/2}^2} \\
\Pi &= \frac{1}{6} \left(\Pi_{1/2} + 4\Pi_{3/2} + \Sigma_{1/2} - \sqrt{\Pi_{1/2}^2 + 2\Pi_{1/2}\Pi_{3/2} - 2\Pi_{3/2}^2 - 4\Pi_{1/2}\Sigma_{1/2} + 2\Pi_{3/2}\Sigma_{1/2} + \Sigma_{1/2}^2} \right) \\
\xi &= \frac{1}{3} \left(-\Pi_{1/2} + 2\Pi_{3/2} - \Sigma_{1/2} + \sqrt{\Pi_{1/2}^2 + 2\Pi_{1/2}\Pi_{3/2} - 2\Pi_{3/2}^2 - 4\Pi_{1/2}\Sigma_{1/2} + 2\Pi_{3/2}\Sigma_{1/2} + \Sigma_{1/2}^2} \right)
\end{aligned} \tag{20}$$

With this information, the diabatic electronic potential energy surfaces can be found from the diagonal terms of the diabatic electronic Hamiltonian matrix (Equation 15). The surfaces for RbHe are shown in Figure 3.

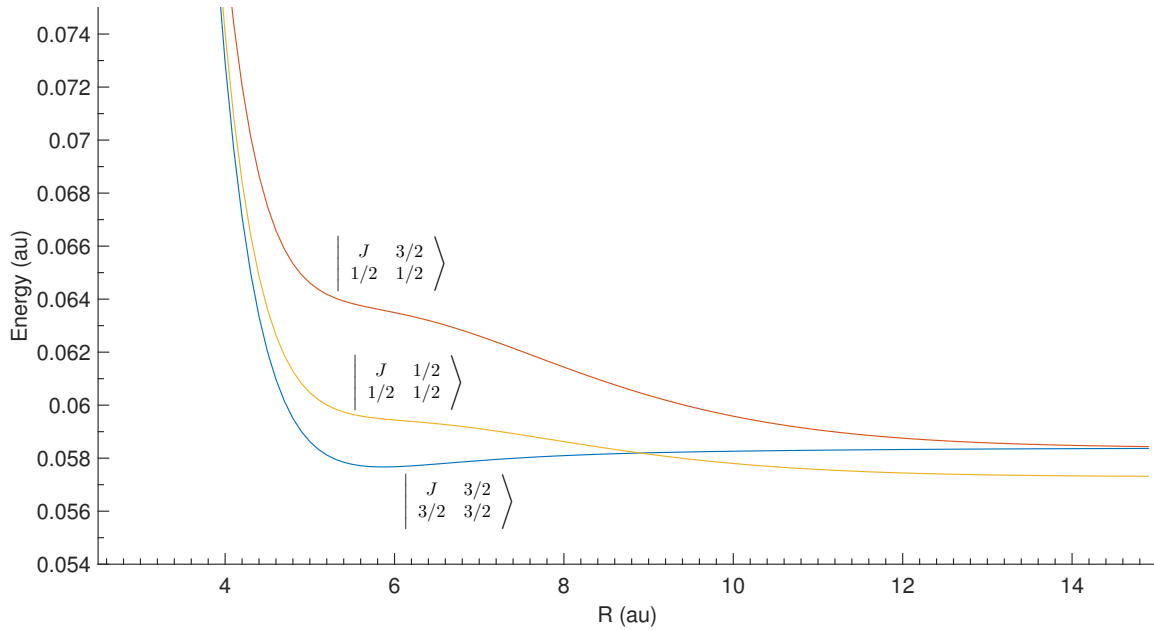


Figure 3. Diabatic potential energy surfaces for RbHe.

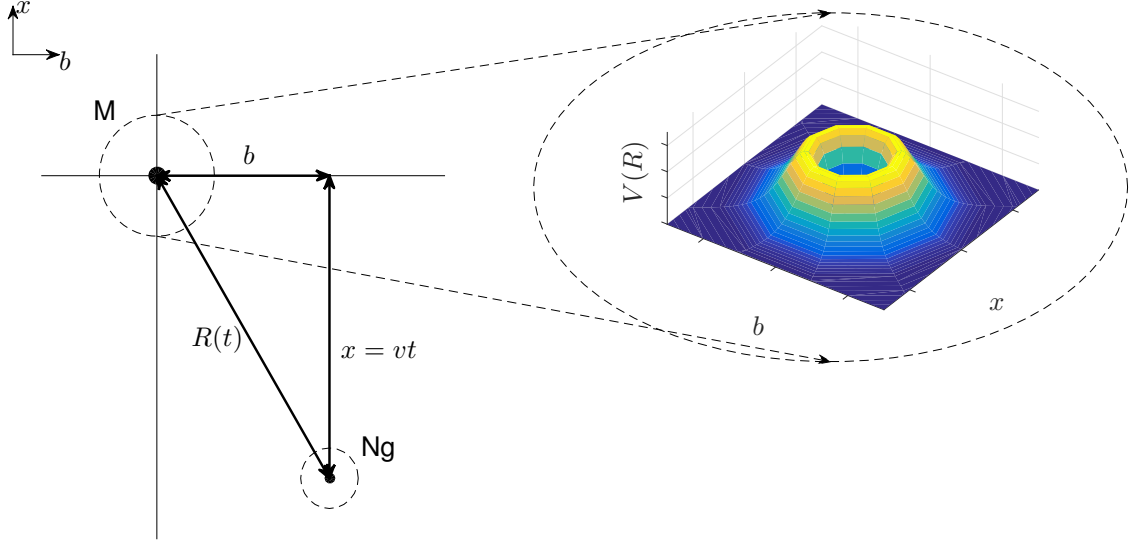


Figure 4. Classical collision between an alkali Metal atom, M, and a noble gas atom, Ng. (The inset plot displays the radial coupling function potential for rubidium and helium).

2.5 Semi-Classical Model for the Probability of Transition for a Single Atom

In order to simplify the full quantum mechanical calculations of the fine structure transition rates [5], several approximations are made to the Hamiltonian matrices in Equations 13, 14, and 15. This is accomplished through the introduction of the semi-classical, two-atom collision model. In this model, an alkali metal atom and a noble gas atom are taken to be point particles. Their locations are described by a two-dimensional Cartesian coordinate system that is centered on the alkali metal and is stationary in the alkali metal's rest frame (see Figure 4). The noble gas atom starts at $x = -\infty$, and travels in a straight line in the positive x direction at a constant velocity, v . The collision is characterized by an impact parameter b . Due to rotational symmetry around the x -axis, only one plane needs to be considered, leaving the rotation to be accounted for through a later integration, and reducing the

problem to a two-dimensional problem. The distance between the particles is given as $R = \sqrt{b^2 + (vt)^2}$. As R changes, the alkali metal's electronic energy states are perturbed in a quantum mechanical interaction through the radial coupling function, $V(R)$. In this simplified model, the classical motion of the atoms is unaffected by the interaction.

To be feasible, this model must account for all terms in the Hamiltonian (Equations 13, 14, and 15). The tracking of these terms as they relate the full quantum approach to the semi-classical approach is not mathematically rigorous, but is instead based on reasonableness arguments. Of course, a quantum mechanical process cannot be fully described in classical terms, but the goal is to distill the system down to its most important elements to make its implementation more practical and to make its inner workings more transparent. Ultimately, the justification for any model is determined by its ability to predict experimental results. Following this reasoning, the classical model replaces the nuclear radial kinetic energy term (Equation 13) through its linear velocity parameter. It also replaces the diagonal elements of the nuclear angular kinetic energy term (Equation 14) through the combination of linear velocity and impact parameter. This leaves the off-diagonal terms of the nuclear angular Hamiltonian matrix and the electronic Hamiltonian matrix. Next, note that the transitions of interest are between the $\left| \begin{smallmatrix} J & 3/2 \\ 1/2 & 1/2 \end{smallmatrix} \right\rangle$ state, which corresponds to the $^2P_{3/2}$ atomic energy level, and the $\left| \begin{smallmatrix} J & 1/2 \\ 1/2 & 1/2 \end{smallmatrix} \right\rangle$ state, which corresponds to the $^2P_{1/2}$ atomic energy level. The mixing of these states is responsible for the establishment of a population inversion in the $^2P_{1/2}$ energy level. This means that the Coriolis coupling within the $^2P_{3/2}$ energy level, between the $\left| \begin{smallmatrix} J & 3/2 \\ 3/2 & 3/2 \end{smallmatrix} \right\rangle$ and $\left| \begin{smallmatrix} J & 3/2 \\ 1/2 & 1/2 \end{smallmatrix} \right\rangle$ states, is not of interest and is therefore neglected. This Coriolis coupling is represented by the off-diagonal elements of the nuclear angular kinetic energy Hamiltonian (Equation 14), which can be ignored, now leaving only the electronic Hamiltonian matrix. Without

the Coriolis coupling, there is no other mixing with the $\left| \begin{smallmatrix} J & 3/2 \\ 3/2 & 3/2 \end{smallmatrix} \right\rangle$ state. This allows the first row and column of the Hamiltonian to be disregarded, which leaves only a 2×2 matrix that governs fine structure transitions,

$$\mathbb{H}_{FS} = \begin{array}{c} \left| \begin{smallmatrix} J & 3/2 \\ 1/2 & 1/2 \end{smallmatrix} \right\rangle \quad \left| \begin{smallmatrix} J & 1/2 \\ 1/2 & 1/2 \end{smallmatrix} \right\rangle \\ \left\langle \begin{smallmatrix} J & 3/2 \\ 1/2 & 1/2 \end{smallmatrix} \right| \quad \left\langle \begin{smallmatrix} J & 1/2 \\ 1/2 & 1/2 \end{smallmatrix} \right| \end{array} \begin{bmatrix} \frac{1}{3}(2\Sigma + \Pi) + \frac{\xi}{2} & -\frac{\sqrt{2}}{3}(\Sigma - \Pi) \\ -\frac{\sqrt{2}}{3}(\Sigma - \Pi) & \frac{1}{3}(\Sigma + 2\Pi) - \xi \end{bmatrix} \quad (21)$$

The off-diagonal elements of the fine structure transition matrix, \mathbb{H}_{FS} , in Equation 21 are given by

$$V(R) = \frac{\sqrt{2}}{3}(\Sigma - \Pi) \quad (22)$$

where $V(R)$ is the radial coupling function, which mixes the $\left| \begin{smallmatrix} J & 3/2 \\ 1/2 & 1/2 \end{smallmatrix} \right\rangle$ and $\left| \begin{smallmatrix} J & 1/2 \\ 1/2 & 1/2 \end{smallmatrix} \right\rangle$ states. A positive $V(R)$ is arbitrarily chosen, since the magnitude of $V(R)$ is the quantity of interest. The radial coupling surface for RbHe is shown in Figure 5. The assumption of a straight line trajectory effectively treats the diagonal elements of \mathbb{H}_{FS} as constants and yields time-dependent off-diagonal terms,

$$\mathbb{H}_{FS}(t) = \begin{array}{c} \left| {}^2P_{3/2} \right\rangle \quad \left| {}^2P_{1/2} \right\rangle \\ \left\langle {}^2P_{3/2} \right| \quad \left\langle {}^2P_{1/2} \right| \end{array} \begin{bmatrix} E_{3/2} & V(R(t)) \\ V(R(t)) & E_{1/2} \end{bmatrix} \quad (23)$$

where the time dependence enters through $R(t)$ as determined by the straight line trajectories. The time dependent Hamiltonian in Equation 23 can be used with time-

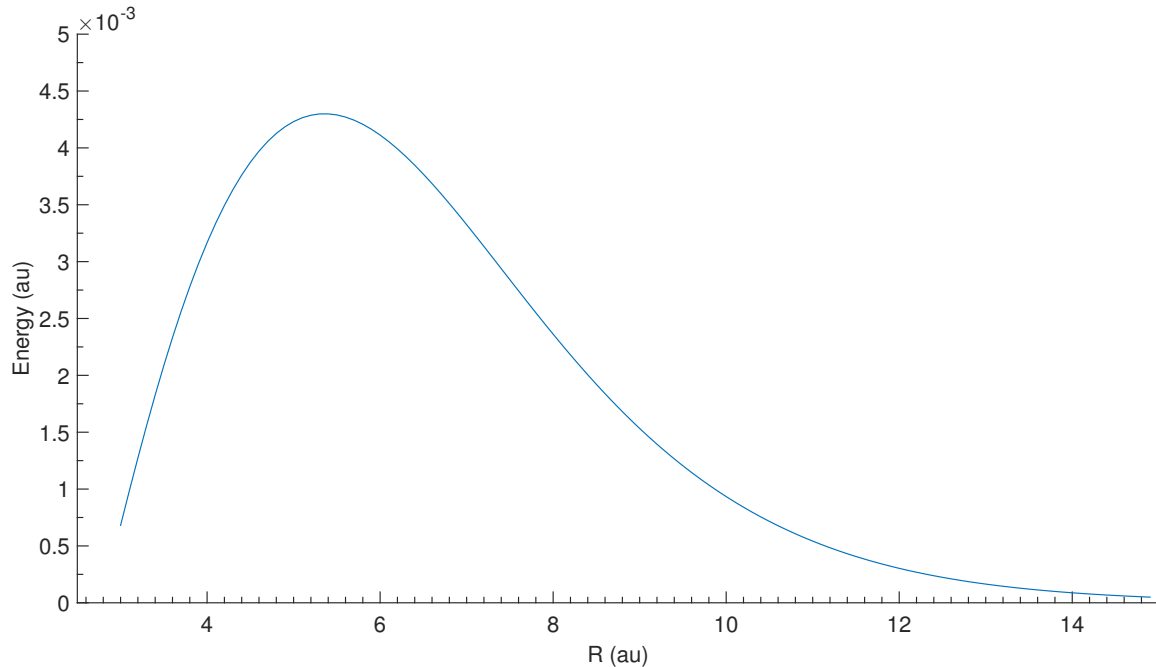


Figure 5. The radial function that couples the adiabatic and diabatic potential energy surfaces for RbHe.

dependent perturbation theory (Section 2.6) to determine the probability of a fine structure transition during a collision.

2.6 Time-Dependent Perturbation Theory

Paralleling the development of time-independent perturbation theory in [4], suppose there are two stationary state wave functions, $\psi_{1/2}$, corresponding to the $^2P_{1/2}$ atomic energy level, and $\psi_{3/2}$, corresponding to the $^2P_{3/2}$ atomic energy level. These could be the two upper states of a DPAL. Considering just these two atomic energy levels, and a single electron in the $^2P_{3/2}$ energy level, the full wave function is

$$\Psi(r, t) = C_{1/2}\psi_{1/2}(r)e^{-iE_{1/2}t/\hbar} + C_{3/2}\psi_{3/2}(r)e^{-iE_{3/2}t/\hbar} \quad (24)$$

where $C_{1/2}$ and $C_{3/2}$ are normalization constants. With the electron starting in the upper state, the probability of finding the electron in each state is

$$\begin{aligned} |C_{1/2}|^2 &= 0 \\ |C_{3/2}|^2 &= 1 \end{aligned} \tag{25}$$

Now, if these are truly stationary states, then this system is of no interest because transitions between the $^2P_{3/2}$ and $^2P_{1/2}$ energy levels are required to establish a population inversion, and without the population inversion there would be no gain in the laser. So instead consider that $C_{1/2}$ and $C_{3/2}$ are functions of time. This corresponds to adding a time-dependent perturbation to the original time-independent Hamiltonian, H^0 ,

$$H = H^0 + H'(t) \tag{26}$$

Solving the Schrödinger equation with this Hamiltonian gives

$$\begin{aligned} \dot{C}_{1/2} &= -\frac{i}{\hbar} H'_{\frac{1}{2}, \frac{3}{2}} e^{-i\Delta t} C_{3/2} \\ \dot{C}_{3/2} &= -\frac{i}{\hbar} H'_{\frac{3}{2}, \frac{1}{2}} e^{-i\Delta t} C_{1/2} \\ \Delta &\equiv \frac{E_{3/2} - E_{1/2}}{\hbar} \end{aligned} \tag{27}$$

which are exact solutions. To apply the time-dependent perturbation, start with the zeroth order approximation

$$\begin{aligned} C_{1/2}^{(0)}(t) &= 0 \\ C_{3/2}^{(0)}(t) &= 1 \end{aligned} \tag{28}$$

which corresponds to the electron remaining in its original state. Next, applying the first order correction by combining Equations 27 and 28, and solving gives

$$C_{1/2}^{(1)}(t) = -\frac{i}{\hbar} \int_0^t H'_{\frac{1}{2}, \frac{3}{2}}(t') e^{-i\Delta t'} dt' \tag{29}$$

which means that the probability that the electron changed energy levels is

$$\left| C_{1/2}^{(1)}(t) \right|^2 = \left| -\frac{i}{\hbar} \int_0^t H'_{\frac{1}{2}, \frac{3}{2}}(t') e^{-i\Delta t'} dt' \right|^2 \quad (30)$$

2.7 Determining Transition Rates and Probabilities

When applied to the classical model, Equation 30 provides the single-atom transition probability, P_0 , as

$$P_0(b, v) = \left| \frac{i}{\hbar} \int_{-\infty}^{\infty} V(R(b, v, t)) e^{-i\Delta t} dt \right|^2 \quad (31)$$

where the limits have been adjusted to model the noble gas atom approaching from a distance $x = -\infty$ where V is negligible, interacting with the alkali metal, then proceeding on to $x = \infty$ where V is negligible again. This equation is the probability that an electron in a single alkali metal atom will transition between electronic energy levels during a collision. This equation only accounts for a single collision possessing a single velocity and a single impact parameter. This probability will be integrated across velocity and impact parameter, but first some relationships must be described.

The experimental data that the results of this thesis will be compared against were recorded as collision cross sections, $\sigma(T)$, which are functions of temperature [3]. In a hard sphere collision model, the collision cross sections can be found through their relationship with the number of collisions, N , in a cylindrical volume,

$$\begin{aligned} N &= \text{Volume} \times \text{Density} \\ &= (\bar{v} t \sigma) \times n \end{aligned} \quad (32)$$

where \bar{v} is the mean velocity, t is the elapsed time, and n is the number of atoms per unit volume. Defining a rate coefficient, K , as the number of collisions per unit of

time, per particle number density gives

$$\begin{aligned} K &= \frac{N}{t n} \\ &= \bar{v} \sigma \end{aligned} \tag{33}$$

The collision cross section can now be found through the relation

$$\sigma = \frac{K}{\bar{v}} \tag{34}$$

The total probability is given by the ratio

$$\begin{aligned} P &= \frac{\sigma}{\sigma_{QD}} \\ &= \frac{K}{\sigma_{QD} \bar{v}} \end{aligned} \tag{35}$$

where σ_{QD} is the quantum defect collision cross section, defined as [3]

$$\sigma_{QD} = \pi (\langle r \rangle + r_{Rg})^2 \tag{36}$$

where $\langle r \rangle$ is the expectation value of the electron position, and r_{Rg} is the effective radius of the atom.

To find the rate coefficient, K , the probability for the transition of a single atom is first multiplied by velocity and then averaged over velocity using the Maxwell-Boltzmann distribution for an ideal gas,

$$K_0 = 4\pi \left(\frac{\mu}{2\pi k_B T} \right)^{3/2} \int_0^\infty v^3 e^{\left(-\frac{\mu v^2}{2k_B T} \right)} P_0(b, v) dv \tag{37}$$

where μ is the reduced mass of the M+Ng pair, k_B is the Boltzmann constant, and T is the temperature. To account for all impact parameters, b , an integration across b is performed, where a factor of 2π is included to account for the cylindrical symmetry

of the collision geometry

$$K_1 = 2\pi \int_0^\infty b K_0 db \quad (38)$$

The final rate equation becomes

$$K = 2\pi \int_0^\infty b 4\pi \left(\frac{\mu}{2\pi k_B T} \right)^{3/2} \int_0^\infty v^3 e^{\left(-\frac{\mu v^2}{2k_B T} \right)} \left| \frac{i}{\hbar} \int_{-\infty}^\infty e^{(-i\Delta t)} V(R(b, v, t)) dt \right|^2 dv db \quad (39)$$

The rate equation has units of length cubed over time, and represents the probability of transition per unit time per particle number density.

2.8 Approximations of the Radial Coupling Function, $V(R)$

Besides using the radial coupling function $V(R)$ from Equation 22 directly, two approximate forms of the radial coupling function $V(R)$ were used in this thesis. The quantum mechanically calculated $V(R)$ from Equation 22 will now be referred to as $V_{QM}(R)$. The first approximation, $V_{RG}(R)$, is a rectangle function with a Gaussian onset/offset as shown in Figure 6 and defined as

$$V_{RG}(R) = \begin{cases} V_0 & \text{if } R \leq L \\ V_0 \exp \left[-\frac{(R-L)^2}{2W^2} \right] & \text{if } R > L \end{cases} \quad (40)$$

by the three parameters of peak potential V_0 , interaction length L , and onset width W . This “rectangular-Gaussian” approximation model was adjusted to be a close match to the radial coupling potential $V_{QM}(R)$. An attempt was made to find an analytic form of the rate equation (Section 2.10) using this $V_{RG}(R)$ approximation, but it was unsuccessful. This led to the second form of approximation, $V_{RG}(t)$, which

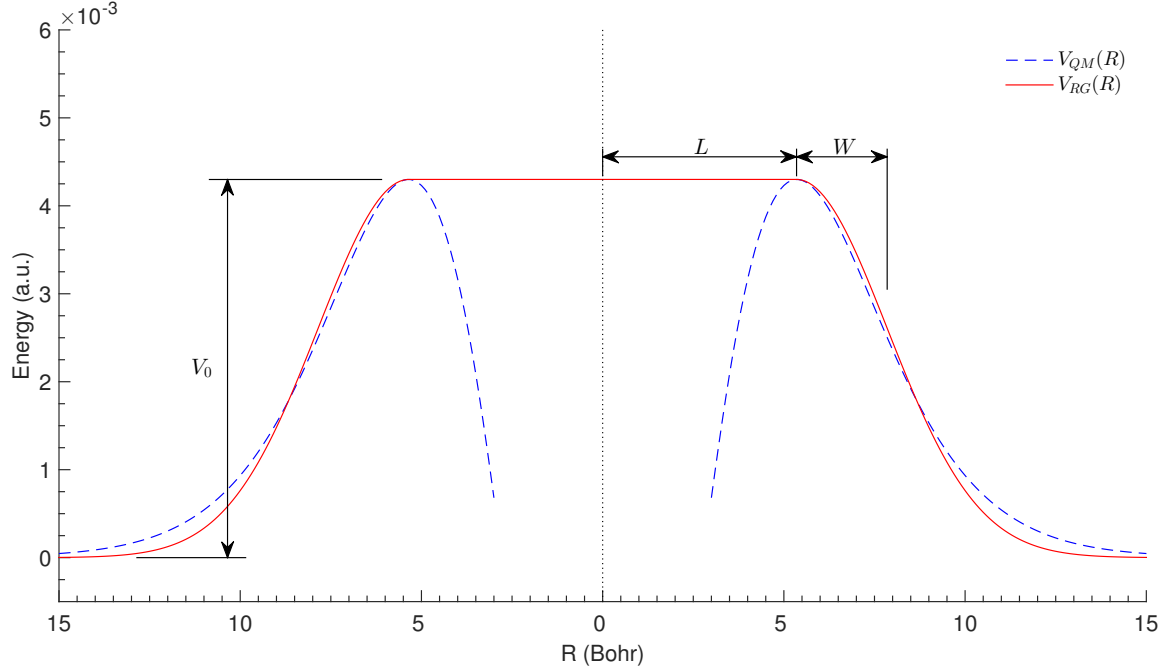


Figure 6. A slice of the rectangular Gaussian approximation, $V_{RG}(R)$, to the coupling potential, $V_{QM}(R)$. The potential and approximation are shown for RbHe, with impact parameter $b = 0$.

is shown in Figure 7 and is defined as

$$V_{RG}(t) = \begin{cases} V_0 \exp \left[-\frac{(t+\tau)^2}{2s^2} \right] & \text{if } t < -\tau \\ V_0 & \text{if } -\tau \leq t \leq \tau \\ V_0 \exp \left[-\frac{(t-\tau)^2}{2s^2} \right] & \text{if } t > \tau \end{cases} \quad (41)$$

It is found by the transformation of the explicit independent variable in $V_{RG}(R)$ from R to t through the relationship,

$$R^2(t) = b^2 + v^2 t^2 \quad \Rightarrow \quad t = \pm [(R^2 - b^2)/v^2]^{1/2} \quad (42)$$

then defining τ to be the points where $R = L$

$$\tau = \pm [(L^2 - b^2)/v^2]^{1/2} \quad (43)$$

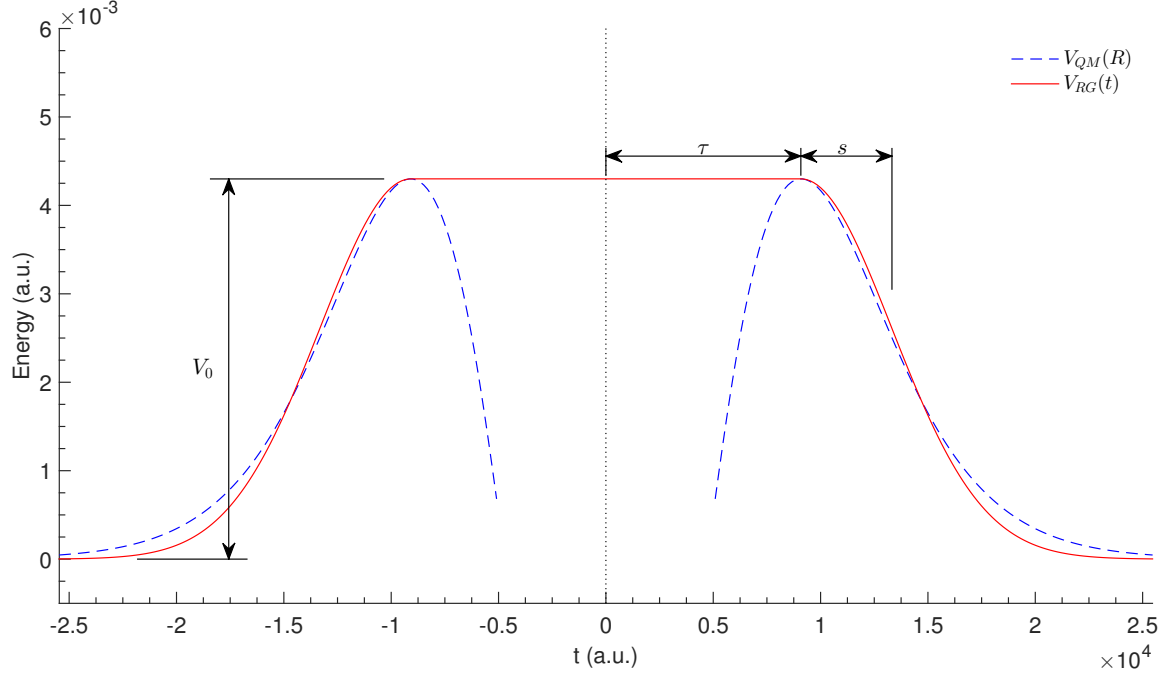


Figure 7. A slice of the rectangular Gaussian approximation, $V_{RG}(t)$, to the coupling potential, $V_{QM}(R)$. The potential and approximation are shown for RbHe, with $v = \bar{v}$ and impact parameter $b = 0$. $V_{QM}(R)$ is transformed from spatial coordinates to temporal coordinates according to the relationship $R = \sqrt{b^2 + (vt)^2} = vt$.

This has the consequence of limiting τ to values where $b < L$, which introduces an unknown approximation by eliminating grazing collisions for which $b > L$. The other main difference between $V(R)$ and $V(t)$ lies in the conversion of W to s , where W and s scale the widths of the Gaussian curves. The factor s is defined as

$$s = \frac{W}{\bar{v}} \quad (44)$$

where the mean velocity, \bar{v} , is used rather than v in order to keep this factor constant to permit an analytic integration of the rate equation, K . In temporal coordinates (which the integral containing V is in) W is effectively a function of velocity, $W(v)$, while s is not. As a consequence, $V_{RG}(R)$ maintains its similarity to $V_{QM}(R)$, while $V_{RG}(t)$ becomes compressed or extended as the relative velocity of the atoms varies (see Figures 8 and 9).

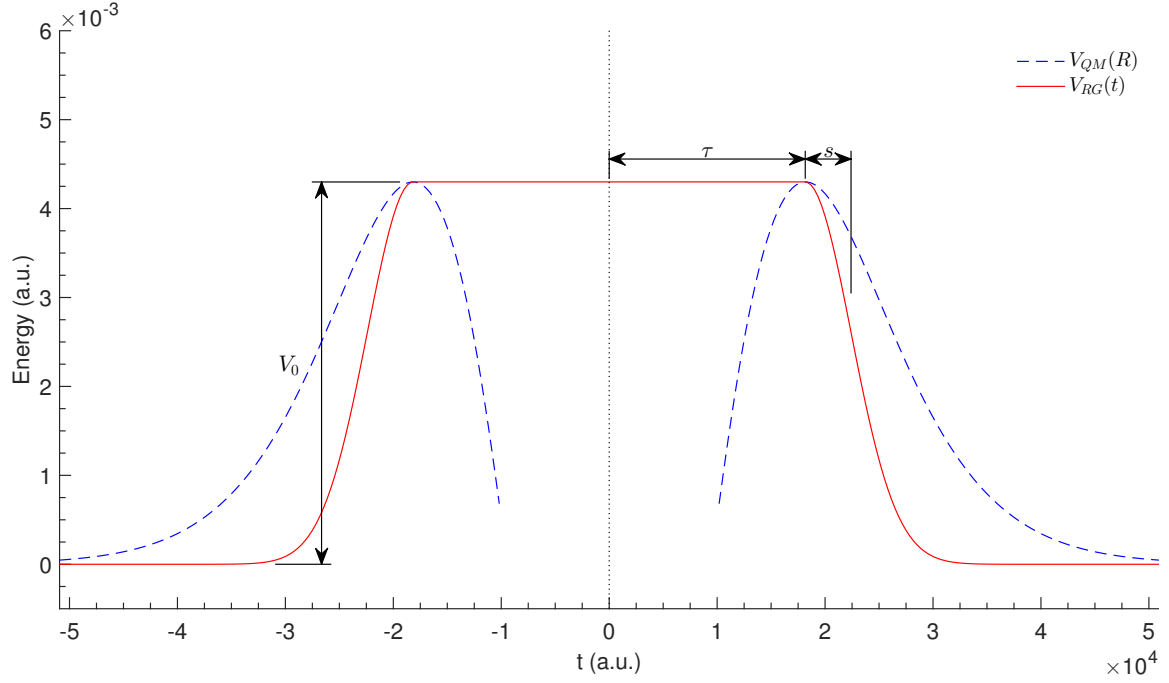


Figure 8. A slice of the rectangular Gaussian approximation, $V_{RG}(t)$, to the coupling potential, $V_{QM}(R)$. The potential and approximation are shown for RbHe, with $v = \frac{1}{2}\bar{v}$ and impact parameter $b = 0$. Notice that the scaling is maintained for everything except $s = \frac{W}{\bar{v}}$. $V_{QM}(R)$ is transformed from spatial coordinates to temporal coordinates according to the relationship $R = \sqrt{b^2 + (vt)^2} = vt$.

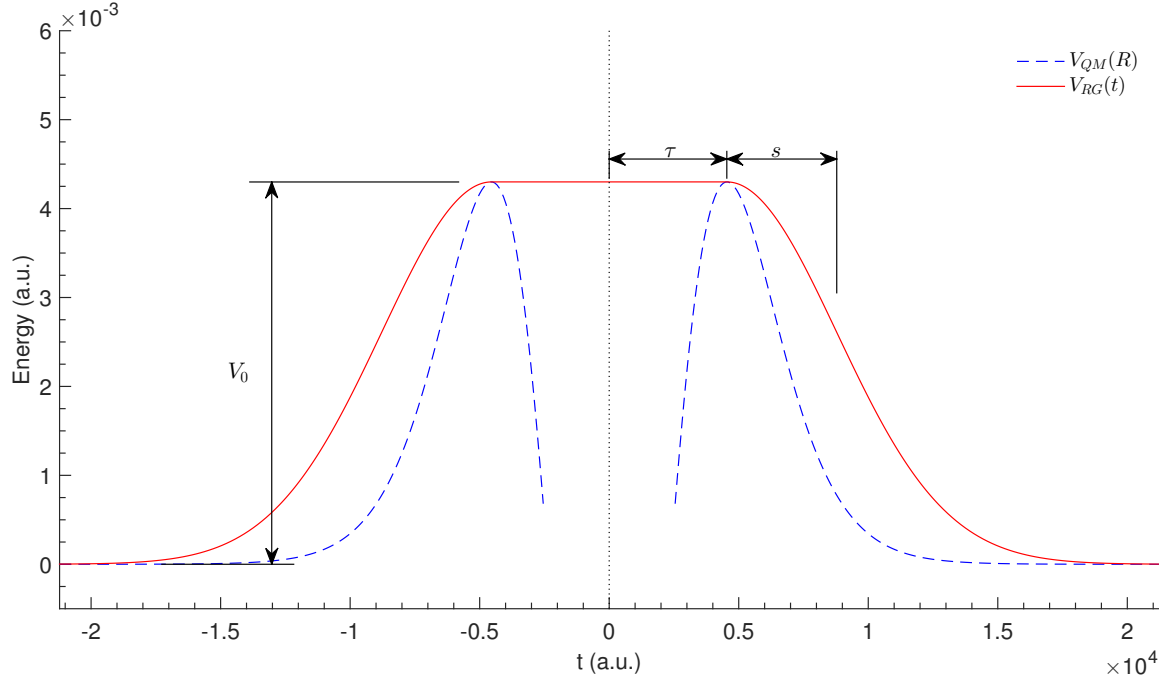


Figure 9. A slice of the rectangular Gaussian approximation, $V_{RG}(t)$, to the coupling potential, $V_{QM}(R)$. The potential and approximation are shown for RbHe, with $v = 2\bar{v}$ and impact parameter $b = 0$. Notice that the scaling is maintained for everything except $s = \frac{W}{v}$. $V_{QM}(R)$ is transformed from spatial coordinates to temporal coordinates according to the relationship $R = \sqrt{b^2 + (vt)^2} = vt$.

2.9 Adiabaticity

Adiabaticity can be defined in different ways, depending on the context, so it is important to be clear what is meant by the term. In this thesis it is defined as the ratio of two characteristic time scales, $\tau_{\text{collision}}$ and $\tau_{\text{spin-orbit}}$. As it applies to the collision between two atoms, adiabaticity, α , is defined here as

$$\begin{aligned}\alpha &= \frac{\text{Duration of Collision}}{\text{Spin-Orbit Time Scale}} \\ &= \frac{\tau_{\text{collision}}}{\tau_{\text{spin-orbit}}}\end{aligned}\tag{45}$$

The duration of a collision is

$$\tau_{\text{collision}} = \frac{2L}{\bar{v}}\tag{46}$$

where L is the interaction length defined in Section 2.5 (with a factor of two, because it is defined as a radial interaction length), and \bar{v} is the mean relative velocity of the atoms at a given temperature. The spin-orbit time scale is given by

$$\tau_{\text{spin-orbit}} = \frac{2\pi}{\Delta}\tag{47}$$

where Δ is defined in Equation 27 as the angular frequency associated with the $^2P_{3/2}$ to $^2P_{1/2}$ energy level transition. Combining these two definitions provides the final form of the adiabaticity equation

$$\alpha = \frac{L}{\bar{v}} \frac{\Delta}{\pi}\tag{48}$$

The integrand from the equation for the probability of a transition in a single atom, Equation 31, is given by

$$V(R(b, v, t)) e^{-i\Delta t}\tag{49}$$

and is plotted in Figures 10 and 11 to illustrate the relationships between the two characteristic time scales for RbHe at various factors of mean relative velocity for various temperatures.

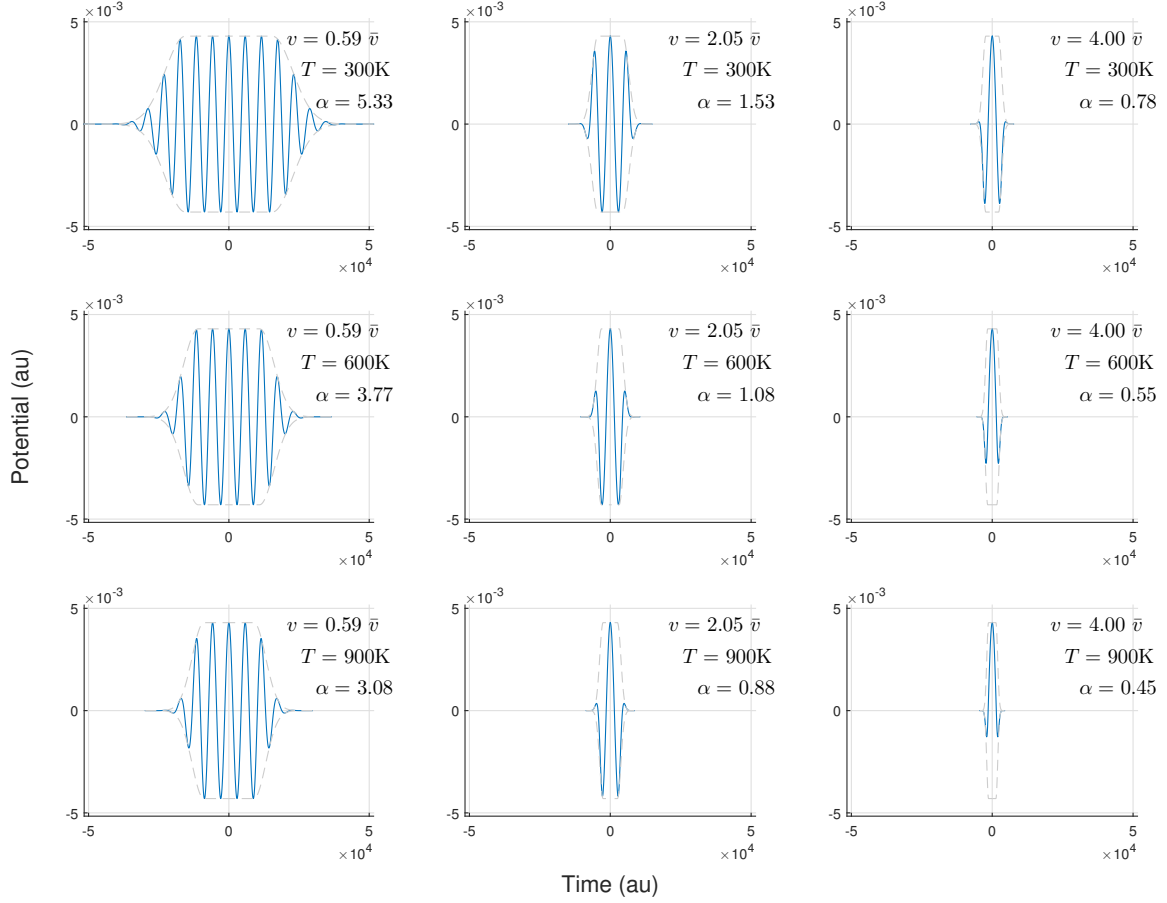


Figure 10. Adiabaticity range for a collision between rubidium and helium. Temperatures range from 300K to 900K. Velocities range from $0.59 \bar{v}$ to $4.0 \bar{v}$ (where \bar{v} is the average relative thermal velocity). The plot maintains a consistent scaling across time.

2.10 Analytic Approximation of Transition Probability

An analytic approximation for the total fine structure transition probability (Equation 35) has previously been derived [8], and the results of this derivation are used in this thesis. A short overview of this analytic approximation is given here. Combining

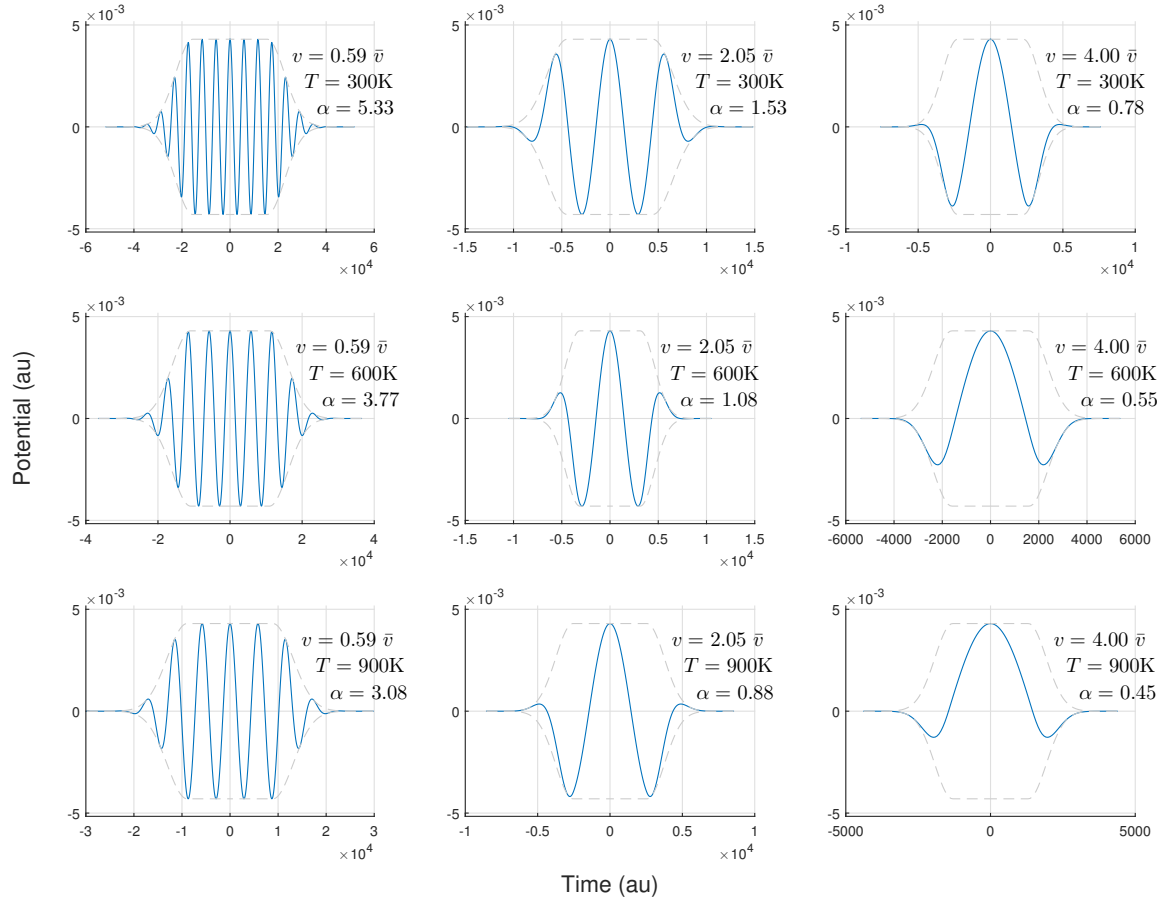


Figure 11. Adiabaticity range for a collision between rubidium and helium. Temperatures range from 300K to 900K. Velocities range from 0.59 \bar{v} to 4.0 \bar{v} (where \bar{v} is the average relative thermal velocity). Note that the scaling of the axes varies (the frequency of the oscillation is constant).

the single-collision transition probability, Equation 31, and the definition of $V_{RG}(t)$ in Equation 41 gives

$$\begin{aligned}
P_0(b, v) &= \left| \frac{i}{\hbar} \int_{-\infty}^{\infty} V(t) e^{-i\Delta t} dt \right|^2 \\
&= \frac{V_0^2}{\hbar^2} \left| \int_{-\infty}^{-\tau} dt \exp \left\{ -\frac{(t+\tau)^2}{2s^2} - i\Delta t \right\} \right. \\
&\quad + \int_{-\tau}^{\tau} dt \exp \{ -i\Delta t \} \\
&\quad \left. + \int_{\tau}^{\infty} dt \exp \left\{ -\frac{(t-\tau)^2}{2s^2} - i\Delta t \right\} \right|^2
\end{aligned} \tag{50}$$

After defining the two variables A and B ,

$$\begin{aligned}
A &= \pi^{1/2} \left(\frac{\Delta s}{\sqrt{2}} \right) \exp \left(-\frac{\Delta^2 s^2}{2} \right) \\
B &= 1 - A \operatorname{erfi} \left(\frac{\Delta s}{\sqrt{2}} \right)
\end{aligned} \tag{51}$$

and integrating, the expression can be written as,

$$P_0(b, v) = \frac{4V_0^2}{\hbar^2 \Delta^2} \{ A^2 \cos^2(\Delta \tau) + AB \cos(\Delta \tau) \sin(\Delta \tau) + B^2 \sin^2(\Delta \tau) \} \tag{52}$$

After summing over the impact parameter and taking the thermal average, as done in Section 2.7, various mathematical manipulations and approximations are applied [8] to arrive at an analytic solution for the rate coefficient, K , and the final probability is found to be

$$\begin{aligned}
P &= \frac{K}{\sigma_{QD} \bar{v}} \\
&= \left(\frac{1}{32\pi^2 \hbar^2} \right) \left(\frac{V_0^2 L'^4}{\sigma_{QD} \bar{v}^2} \right) \left(\frac{\bar{v}}{fL'} \right)^4 \left[16\pi (A^2 + B^2) \left(\frac{fL'}{V} \right)^2 \right. \\
&\quad \left. + 2\pi^{1/2} AB \exp \left\{ -\frac{4\pi}{25} \left(\frac{fL'}{\bar{v}} \right) \right\} \sin \left\{ -\frac{4\pi^{1/2}}{2^{1/4}} \left(\frac{fL'}{\bar{v}} \right) \right\} \right]
\end{aligned} \tag{53}$$

where $\left(\frac{fL'}{\bar{v}} \right)$ is the adiabaticity, using $L' = 2L$ and $f = \frac{\Delta}{2\pi}$.

III. Procedure and Numerical Methods

3.1 Numerical Systems

For any numerical routine, it is critically important to consider the numerical limitations of the computational system being used. To begin the discussion, some terminology must be defined. Floating point numbers are represented by the combination of the components,

$$S \times M \times B^{e-E} \quad (54)$$

where S is the sign bit, M is the mantissa, B is the base, e is the exponent, and E is the bias. Being a finite system, each of these components has a set number of digits allocated to its representation. As a simple, concrete example to help visualize some of the consequences of this representation, assume that we have a base 10 system with a three digit mantissa and a two digit exponent. This allows the mantissa to represent any number from 0 to 999, and allows the exponent to represent any number from 0 to 99. Adding a bias of 49 to the exponent shifts its range to the values -49 through 50. A number represented in this system would have the form $\pm 000 \times 10^{\pm 00}$. From this example, it becomes clear how the number of digits available to describe each floating point number limit the numerical precision and the range of the system.

The relative numerical precision of the system (unscaled by the exponent) is related to the machine epsilon, ϵ_m , which is defined as the smallest number that makes $1 + \epsilon_m \neq 1$ true. It is easy to see that $\epsilon_m = 0.01$ in this system, because this value of ϵ_m is the smallest number that makes the following true

$$\begin{aligned} 1 &+ \epsilon_m &\neq & 1 \\ 1 &+ 0.01 &\neq & 1 \\ (100 \times 10^{-02}) &+ (001 \times 10^{-02}) &\neq & (100 \times 10^{-02}) \end{aligned} \quad (55)$$

It is important to notice that the machine epsilon, which is determined by the mantissa, is not the same as the smallest number that the system can represent, which is determined by the exponent and bias. In the example presented here, $\epsilon_m = 10^{-02}$, but the system can represent numbers as small as 10^{-49} . The range of the system is determined by the number of digits in the exponent, which translates to the number of orders of magnitude of the base that the floating point representation can be scaled by. See Table 1 for a list of common system values used by most modern computers [2].

Table 1. Standard values used to represent floating point precision and double precision numbers in modern computers (also see Equation 54). *The value of the mantissa can effectively be more than the storage space allocated, due to normalization (see [2] for more information).

	Float	Double
Base	2	2
Mantissa Number of Digits	23(+1)*	52(+1)*
Exponent Number of Digits	8	11
ϵ_m	1.19×10^{-7}	2.22×10^{-16}
Minimum Number	1.18×10^{-38}	2.23×10^{-308}
Maximum Number	3.40×10^{38}	1.80×10^{308}

Rounding errors due to machine epsilon limitations can sometimes be minimized by changing the order that calculations are done, to minimize the addition or subtraction of numbers with highly disparate orders of magnitude. Also, to avoid errors that are caused by the use of values that approach the machine's minimum or maximum representable values, appropriate systems of units can be chosen. Here, atomic units were selected for that reason, but this may not always be necessary for modern computer systems, as long as double precision is used.

When performing a very large number of calculations, accumulation of machine error can begin to be a problem. Assuming that the error is not biased in any

particular direction, machine epsilon will accumulate in a random walk pattern, which puts the error on the order of $\sqrt{N}\epsilon_m$, where N is the number of calculations performed.

3.2 Selection of Method of Quadrature

Ideally, the number of calculations required in a numerical routine would be minimized. This both reduces the computation time and reduces the chance for the accumulation of rounding error. Due to the very large number of iterations required to solve the equations in this thesis, it was very important to find a quickly converging numerical quadrature (integration) routine. An algorithm using only the trapezoidal rule is very robust but can require many computations to achieve the required accuracy [7]. Due to this large number of computations, the accumulated machine error can begin to be significant. The upper plots in Figures 12 and 13 show the expected convergence of a trapezoidal rule routine [7], along with its actual convergence for a few sample cosine integrals. Figure 12 uses single floating point precision, and Figure 13 uses double floating point precision. Also included in the figures is the approximate machine accuracy and the theoretical accumulated machine error for floating point numbers. The figures also show the expected convergence rate of Romberg integration algorithms [7], which are described below. Note that the error accumulation shown in the figures is for a single integral. If performing calculations for a three-variable integral, the number of points required is approximately the cube of the number of points required for each single-variable integral, assuming similar functions for each variable.

Romberg integration routines build upon the strength of trapezoidal rule algorithms but converge much more quickly. The Romberg method combines multiple iterations of the trapezoidal rule algorithm. With each iteration of the trapezoidal rule algorithm, the integrand is calculated at an increasing number of points. The

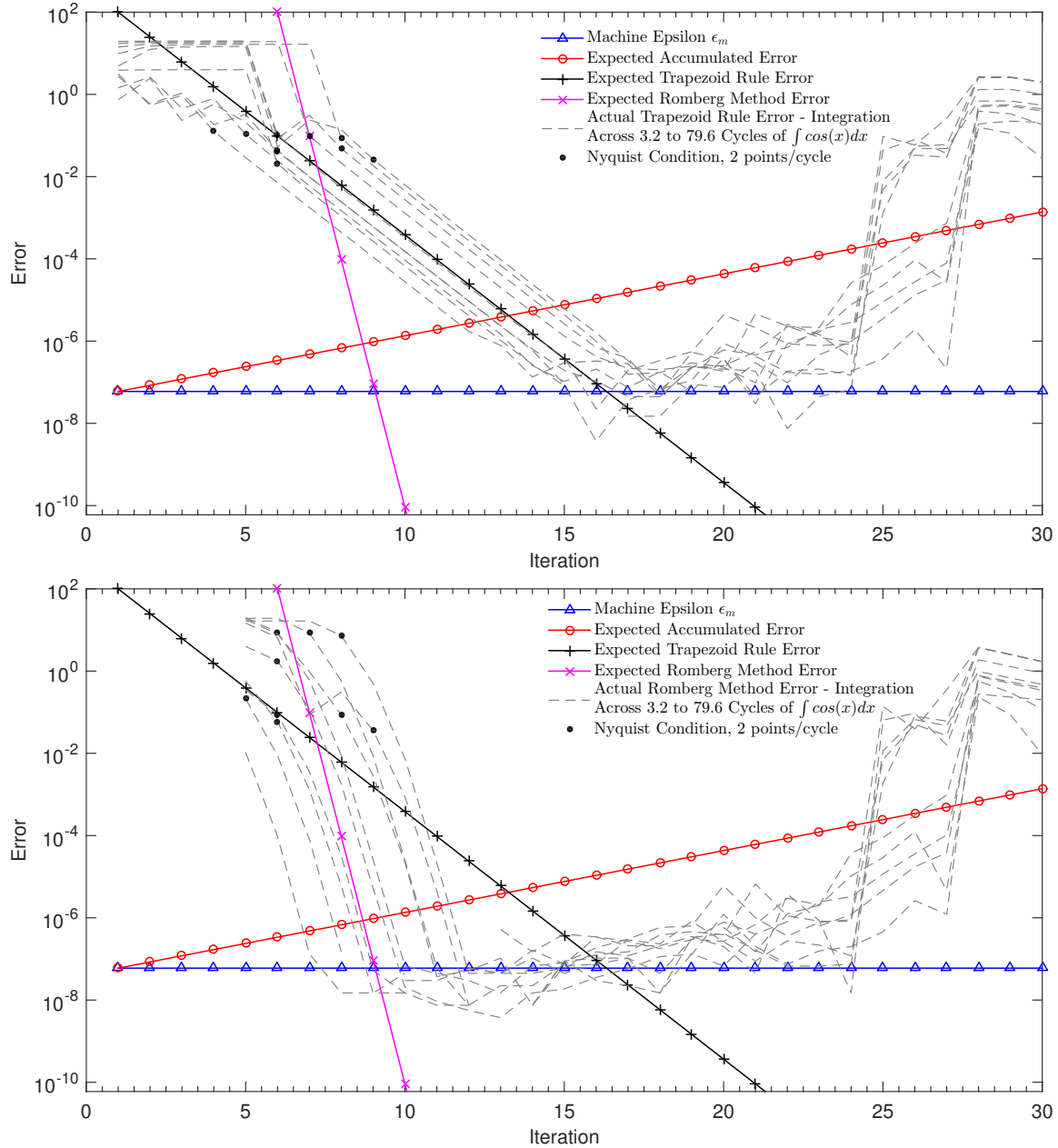


Figure 12. Single-precision convergence for numerical integration using the trapezoidal rule (top) and the Romberg method (bottom). The dashed lines show the actual error in a few sample cosine integrals, while the solid lines show theoretical error. The number of points where the integrand is evaluated, N , is related to the number of iterations, j , by the formula $N = 2^{j-1} + 1$. The black dots mark the points where the integrand is calculated for at least two points per cycle. Notice that both routines crash around $j = 25$ iterations. This is likely related to the fact that this is where the spacing between points has the same order of magnitude as ϵ_m .

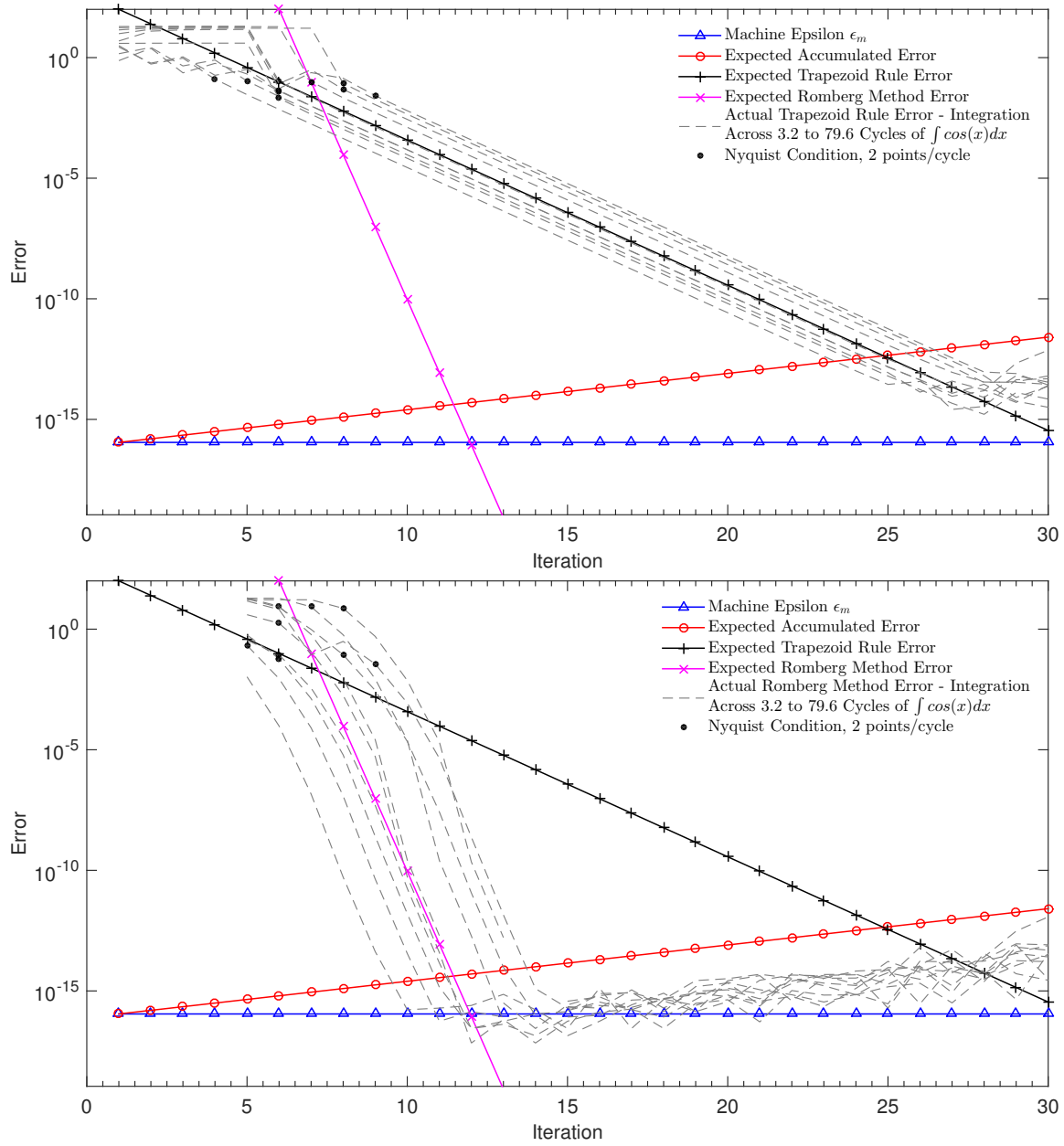


Figure 13. Double-precision convergence for numerical integration using the trapezoidal rule (top) and the Romberg method (bottom). The dashed lines show the actual error in a few sample cosine integrals, while the solid lines show theoretical error. The number of points where the integrand is evaluated, N , is related to the number of iterations, j , by the formula $N = 2^{j-1} + 1$. The black dots mark the points where the integrand is calculated for at least two points per cycle.

Romberg method uses the results of the trapezoidal rule iterations in a weighted extrapolation to determine a more accurate solution. The lower plots of Figures 12 and 13 show the actual convergence of a Romberg routine. This Romberg routine uses the same cosine integrals as used by the trapezoidal rule algorithm in the upper plots. To aid comparison, the lower plots also show the same theoretical information as the upper plots. Notice that, by converging faster, less accumulated machine error accrues, and the Romberg routine is able to achieve a couple of orders of magnitude of higher precision as compared to the trapezoidal rule, before machine limits dominate the result. This effect is most pronounced in the plots with double precision.

Numerical Recipes in C [7] includes an iterative, adaptive Romberg integration routine that the code used in this thesis was based on. For the first iteration, it calculates the value of the integrand at the limits of integration. For the second iteration, it finds the midpoint between the limits of integration, and calculates the integrand there. It continues for subsequent iterations, finding the midpoints between each pair of adjacent points from the previous iteration, and calculating the integrand at each of these midpoints. After each iteration it sums the results, and multiplies by the step size, combining the new result with the result from the previous iteration. In this way, the calculations at points from previous iterations are not wasted, but are instead combined with calculations from new iterations so that the solution can be refined without having to re-accomplish previous work. The total number of points, N , after j iterations is

$$N_j = 2^{j-1} + 1 \tag{56}$$

So far, this just describes an iterative trapezoidal rule algorithm. The Romberg method expands upon and refines the trapezoidal rule algorithm by applying Richardson extrapolation (also known as Richardson's deferred approach to the limit). Richardson extrapolation combines increasingly precise approximations of the integral in a

way that cancels low order error terms [2] [7]. As long as the error estimate is small, then this increased order of the error estimate translates to an increase in convergence rate. Richardson extrapolation is based on the formula

$$I_j^i = \frac{4^i I_j^{i-1} - I_{j-1}^{i-1}}{4^i - 1} \quad (57)$$

which forms the table

$$\begin{array}{cccccc} I_1^0 & & & & & \\ I_2^0 & I_2^1 & & & & \\ I_3^0 & I_3^1 & I_3^2 & & & \\ I_4^0 & I_4^1 & I_4^2 & I_4^3 & & \\ I_5^0 & I_5^1 & I_5^2 & I_5^3 & I_5^4 & \\ \vdots & \vdots & \vdots & \vdots & \vdots & \ddots \end{array} \quad (58)$$

The Romberg method is seeded by the $I_j^{i=0}$, which are the results of successive iterations of the trapezoidal rule algorithm,

$$I_j^{i=0} = \frac{b-a}{2N_j} \sum_{k=1}^{N_j} (f(x_{k+1}) + f(x_k)) \approx I = \int_a^b f(x) dx \quad (59)$$

with each increasing value of i being the next iteration of the Richardson extrapolation. Accuracy of values in the table increases towards the bottom and to the right. When the difference between $I_{jmax}^{i_{max}-1}$ and $I_{jmax}^{i_{max}}$ is smaller than the convergence error condition, then the process ends and $I_{jmax}^{i_{max}}$ is given as the solution to the integral. For example, from the table above,

$$\text{if } (|I_5^3 - I_5^4| < \text{Convergence Error Condition}), \text{ then set } I = I_5^4 \quad (60)$$

where the (relative) convergence error condition is, for example,

$$\text{Convergence Error Condition} = |I_5^4| \times 10^{-6} \quad (61)$$

Due to the oscillatory nature of the integrals used in this thesis, another very important convergence condition was imposed in addition to the relative error requirement. The convergence error check was only performed after the number of total points equaled at least two points per cycle of the oscillating integrand. The requirement for having at least two points of integration per cycle of oscillation is based on the Nyquist sampling theorem from digital signal processing, which states that a continuous wave cannot be sampled at a discrete set of points unless the sample rate is at least twice the rate of the sampled signal [6]. To visualize this requirement, the large dots in Figures 12 and 13 mark the points where this condition is satisfied. Before adding this condition to the code, convergence tests required a much more strict relative error condition, which in turn required much more computation time. Furthermore, even with the stricter error conditions, convergence was very erratic and had to be carefully manually verified. With this “Nyquist condition” included, the code was much more robust, and convergence error conditions could be chosen based on finding a balance between speed and precision. The value chosen for the relative error to end the integration loops was normally set to 10^{-6} , but due to some very high oscillations requiring many more integration points and in turn requiring much more computation time, chosen values ranged from 10^{-4} to 10^{-6} . As will be discussed in more detail, there were many considerations and optimizations implemented that took the computation time down to minutes or hours, from what was originally approximated to have possibly taken months on a standard desktop computer. From what has already been presented, it can be seen that having a very large number

of calculations would build up accumulated error that could possibly dominate the results, bringing any conclusions into question.

Notice that the number of points (see Equation 56) quickly increases as the number of iterations is increased. The number of points where the integrand is calculated begins with 2 points in the first iteration, reaches 17 points after 5 iterations, only 513 points by 10 iterations, then 16,385 after 15 iterations, and a cumbersome 1,048,577 points by 21 iterations. Due to time constraints, the code used in this thesis was designed to report the inability to converge if convergence was not achieved by 25 iterations, or 16,777,217 points. When convergence was not reached by 25 iterations, the convergence error condition was relaxed, starting from a relative error of 10^{-6} . All atomic species were able to converge with at least a 10^{-4} relative error bound.

3.3 Multivariable Quadrature - Optimization and Numerical Integration of the Rate Equation

The multidimensional integral for the rate is given by Equation 39,

$$K = 2\pi \int_0^\infty b \, 4\pi \left(\frac{\mu}{2\pi k_B T} \right)^{3/2} \int_0^\infty v^3 e^{\left(-\frac{\mu v^2}{2k_B T} \right)} \left| \frac{i}{\hbar} \int_{-\infty}^\infty e^{(-i\Delta t)} V(R(b, v, t)) dt \right|^2 dv db$$

This equation is challenging to integrate for three primary reasons; (1) because the integrand may extend across many periods of oscillation, (2) because it is a multivariable integral with three variables of integration, and (3) because some of the integration limits extend to infinity. The techniques described below were used in combination with fairly standard C-programming optimization techniques.

The problem of integrating across many cycles of oscillation was solved by using the adaptive Romberg integration routine along with a sufficiently large number of points of evaluation of the integrand. The fact that the Romberg method converges

relatively quickly, combined with the fact that the routine is adaptive, meaning that only the minimum number of points required for convergence are used, is very important. There are other methods of numerical quadrature that are designed specifically for highly oscillatory functions, and a short detour was made during this research to see if they could be feasible here. Unfortunately, it was not clear if the methods found could handle multivariable integration and/or infinite limits. Due to time constraints and the excessive time required to learn, code, and test the various alternate methods, the search was abandoned before a definitive answer was found. Alternate methods may have provided faster computation times, but they were ultimately unnecessary. The Romberg method is very robust and stable, and works very well for the calculations performed for this thesis, as long as certain considerations are made, as described throughout this section.

Splitting Multidimensional Integral Into Nested Single-Variable Integrals.

To numerically integrate a multivariable integral, the integral must first be broken up into separate, nested integrals. It is already clear that there is a difficult balance to be made between making sure that the integrand is calculated at enough points to get an accurate and precise solution, and using so many points that the computation time becomes excessive or the machine error begins to dominate. One way to minimize the number of computations required is by carefully choosing the way that the multivariable integral, Equation 39, is separated into single-variable integrals. Equation 39 was separated as follows:

$$I_3(b, v) = \left| \frac{i}{\hbar} \int_{-\infty}^{\infty} e^{(-i\Delta t)} V(R(b, v, t)) dt \right|^2 \quad (62)$$

is the innermost integral, representing the probability of transition for a single velocity, v , and for a single impact parameter, b . The middle integral can be taken to be

$$I_2(v) = 2\pi \int_0^\infty b [I_3(b, v)] db \quad (63)$$

which is the integration across all impact parameters and polar angles. This leaves

$$I_1 = 4\pi \left(\frac{\mu}{2\pi k_B T} \right)^{3/2} \int_0^\infty v^3 e^{\left(-\frac{\mu v^2}{2k_B T}\right)} [I_2(v)] dv \quad (64)$$

as the outermost integral, which averages the product of the velocity and probability across the Maxwell Boltzmann distribution.

The integrand in I_1 , being in the outermost integral, gets evaluated $2^{j_1-1} + 1$ times (see Equation 56). The integrand in I_2 must be evaluated $2^{j_2-1} + 1$ times for each evaluation of I_1 , or $(2^{j_2-1} + 1)(2^{j_1-1} + 1)$. The number of evaluations of I_3 is then $(2^{j_3-1} + 1)(2^{j_2-1} + 1)(2^{j_1-1} + 1)$. The integral across t contains functions of each of the integration variables within an absolute square, so it must be the innermost integral, I_3 , and be evaluated first. The integrals over b and v can be easily separated, and are therefore free to change order of integration. Since the innermost of these two integrals will be calculated the most number of times, it should require the least computation time. The integration across v is much more complex because of the Maxwell-Boltzmann distribution, which led to the assumption that it would require more computation time to evaluate, and should therefore be the outer integral, I_1 . This leaves the integration across b as the middle integral, I_2 .

Simplifying the Integrals.

The next step in preparing the integrals for numerical integration was dividing integral I_3 into trigonometric functions, by applying Euler's Formula, $e^{i\theta} = \cos(\theta) +$

$i \sin(\theta)$, then applying some algebraic and trigonometric relations to get,

$$I_3(b, v) = \frac{1}{\hbar^2} \left| i \int_{-\infty}^{\infty} \cos(\Delta t) V(R(b, v, t)) dt + \int_{-\infty}^{\infty} \sin(\Delta t) V(R(b, v, t)) dt \right|^2 \quad (65)$$

which, after more algebra, becomes

$$I_3(b, v) = \frac{1}{\hbar^2} \left[\int_{-\infty}^{\infty} \cos(\Delta t) V(R(b, v, t)) dt \right]^2 + \frac{1}{\hbar^2} \left[\int_{-\infty}^{\infty} \sin(\Delta t) V(R(b, v, t)) dt \right]^2 \quad (66)$$

The equations can be further simplified and optimized by combining constants.

Define:

$$\begin{aligned} C_3 &= \frac{1}{\hbar^2} \\ C_2 &= 2\pi \\ C_{1a} &= 4\pi \left(\frac{\mu}{2\pi k_B T} \right)^{3/2} \\ C_{1b} &= \frac{\mu}{2k_B T} \end{aligned} \quad (67)$$

$$\begin{aligned} I_3(b, v) &= C_3 \left[\int_{-\infty}^{\infty} \cos(\Delta t) V(R(b, v, t)) dt \right]^2 \\ &+ C_3 \left[\int_{-\infty}^{\infty} \sin(\Delta t) V(R(b, v, t)) dt \right]^2 \end{aligned} \quad (68)$$

Note that if $V(R(b, v, t))$ is even, then $\int_{-\infty}^{\infty} \sin(\Delta t) V(R(b, v, t)) dt$ is an odd function being integrated over a symmetric interval, so the integral goes to zero, simplifying and optimizing the rate equation even further. All of the forms of V used in this thesis were even, so the sine term was not used.

$$I_2(v) = C_2 \int_0^{\infty} b [I_3(b, v)] db \quad (69)$$

$$I_1 = C_{1a} \int_0^{\infty} v^3 e^{(-C_{1b} v^2)} [I_2(v)] dv \quad (70)$$

and the full integral, with $C_4 = C_{1a} C_2 C_3$ becomes

$$K = C_4 \int_0^\infty v^3 e^{(-C_1 b v^2)} \int_0^\infty b \left(\int_{-\infty}^\infty \cos(\Delta t) V(R(b, v, t)) dt \right)^2 db dv \quad (71)$$

3.4 Determining the Limits of Integration

Possibly the most difficult, but most important, optimization technique was the determination of suitable limits of integration. It relies on finding the values of the integration variables, beyond which no meaningful contribution was made to the final result. It should be pointed out that there are methods of dealing with infinite limits that involve a change of variable such as $x \rightarrow 1/x$, but these methods cause the oscillations of the integral to steadily increase towards infinite frequencies, so these methods are not feasible here. There are three sets of integration limits to consider in the rate equation (Equation 39), for a total of six limits. Four of these limits extend to infinity, but fortunately the integrands go to zero fairly rapidly.

For the integration across time, both limits go to infinity, but the integrand is scaled by the radial coupling function, $V(R(t))$, which goes to zero as $t \rightarrow \pm\infty$. The non-negligible range of these limits was found using the formula $x_{max} = R_{max} = L + nW$, where n is an integer, and the impact parameter $b = 0$ (b , x , R , L , and W are described in sections 2.5 and 2.8). Through trial and error, values of n ranging from 5 to 7 were found to give relative integration errors ranging on the order of 10^{-6} to 10^{-9} . The limits for t were then found using $t_{limit} = \pm \frac{x_{max}}{v}$. In addition, since the integration across time was of an even function across a symmetric interval, the limits were adjusted to run from $-t_{max}$ to zero, and the result was multiplied by two.

At first look, the required limits on b appear to be similar to the limits on x , but this is not necessarily the case. The rate that $V(R)$ tapers off turns out to have a very large effect on the time integral, and any discontinuities from ending $t = x/v$ too early have a significant impact. The range of b is not as significant because the

integral quickly becomes negligible past $b = L$ (normally). The adiabaticity and relative sizes of L and W turn out to have a significant effect on the required b range, so care must be taken in determining the limits, especially when scaling L and W (Section 5.3). The limit b_{max} was set by the formula $b_{max} = L + mW$, where m is some integer. The limits were verified by inspection, using plots similar to Figure 14 which show the probability amplitude (top) and scaled absolute square of the probability amplitude (bottom) as a function of b , for a sample of evenly spaced points across v . The verification by inspection consisted of making sure that the contribution to the total probability appeared to become insignificant, well before the limits were reached. This method was also verified with a subset of tests where the limits were extended significantly, and the result was compared to results with the original limits.

The velocity limits are the most complicated, and choosing them correctly is extremely important since they have a very large impact on computation time, due to their relationship to the number of oscillations in the integrand. The t limits go to infinity as v goes to its original lower limit of zero, since $t_{limit} = -\frac{x_{max}}{v}$. This means that, as v decreases, the number of oscillations, and in turn the number of integration points required, increases quickly. The upper limit on v is important, but not as critical. These limits were found by solving for the values of v , where v multiplied by the Maxwell-Boltzmann distribution dropped to 1% of its maximum value. These values were found to be

$$\begin{aligned} v_{min} &= \chi_{min} \bar{v} \\ v_{max} &= \chi_{max} \bar{v} \end{aligned} \tag{72}$$

where \bar{v} is the mean velocity, and the χ are constants, invariant with respect to temperature or atomic species. The fact that the χ were constants greatly simplified calculation of these limits for different temperatures and atomic collision partners. The integration limits for v were verified by inspection similarly to the b limits,

see Figure 15 for example. Due to the strong effect of v on the time integral (or similarly, the effect of the single-collision adiabaticity), the limits of integration over v were found to not be as easily described with the Maxwell-Boltzmann distribution as originally expected, and the χ values had to be adjusted accordingly. Velocity limits were normally set to $v_{min} = 0.1\bar{v}$ and $v_{max} = 4.0\bar{v}$. In hindsight, due to the intricate interplay of all of the variables involved, it may have been worthwhile to take the time to implement adaptive integration limits, where the limits automatically increased until no additional significant change in the final solution resulted.

3.5 Calculations Using $V_{RG}(t)$ and the Analytic Form of the Rate Equation

Even though performing calculations using the analytic form of the rate equation that was introduced in Section 2.10 is much faster and easier than performing Romberg integration on the multivariable integral of Equation 39, implementation of the analytic approximation is not completely trivial. This is because A in Equation 51 approaches zero, and the imaginary error function in B approaches infinity, as the quantity Δs increases. Although the product of these two factors is a finite number, these zeros and infinities quickly extend beyond the limits of double precision floating point numbers. Due to this fact, standard numerical software such as Matlab is unable to perform calculations for all of the atomic elements looked at in this thesis. Fortunately, Mathematica is able to extend beyond the limits of double floating point precision, and can perform the required calculations.

3.6 Special Considerations for Integration When Using $V_{QM}(R)$

When using $V_{QM}(R)$ (see Section 2.8 for description) as the radial coupling function in the rate integral, special considerations had to be made. The goal was to use $V_{QM}(R)$ with as little modification as possible, but the prior calculations of the

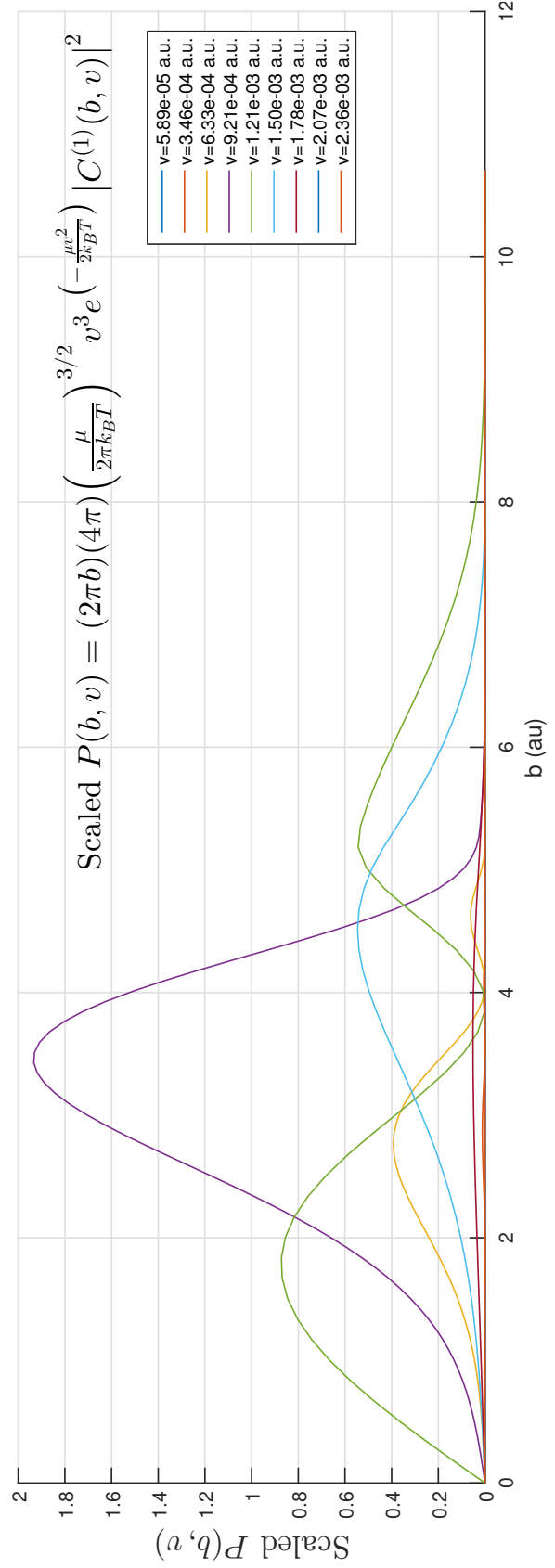
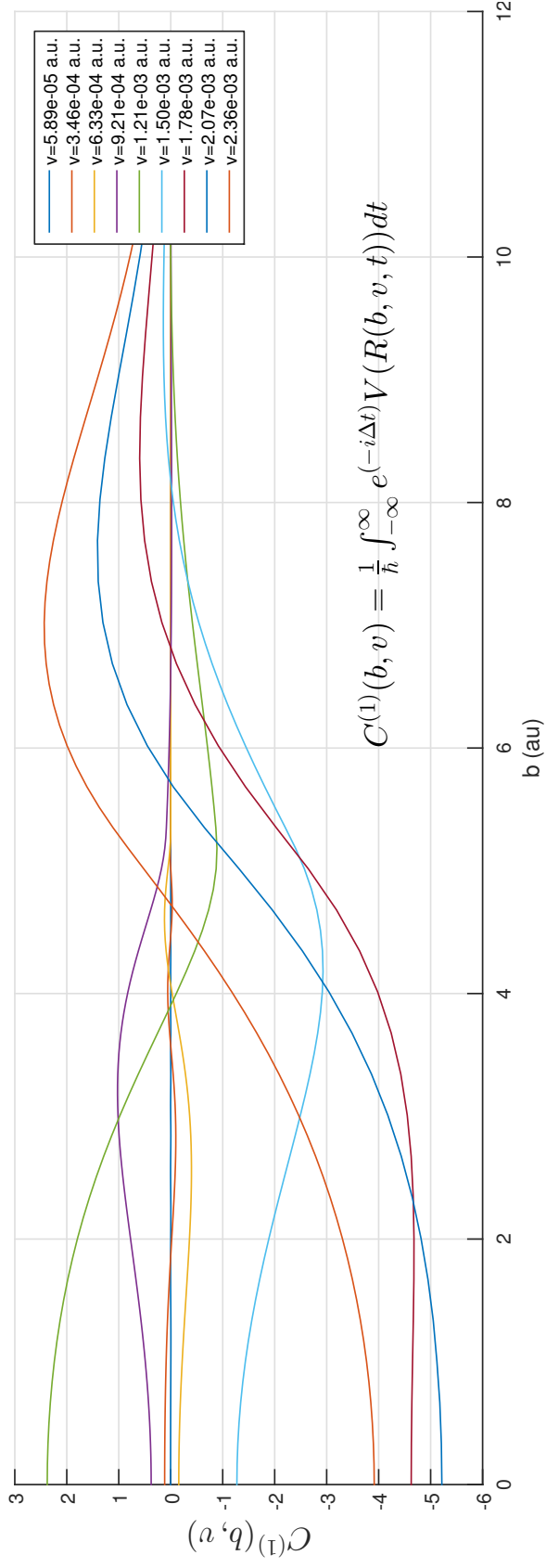


Figure 14. Verification of Limits and Convergence Across Impact Parameters. RbHe at 300K is shown.

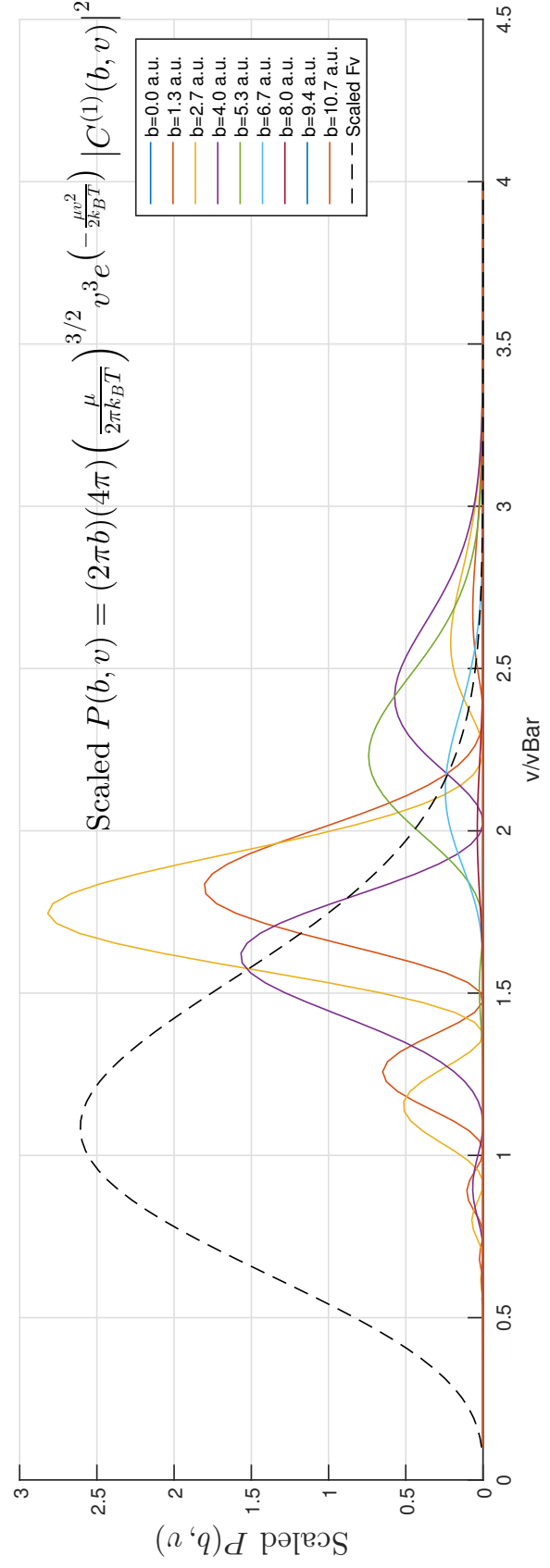
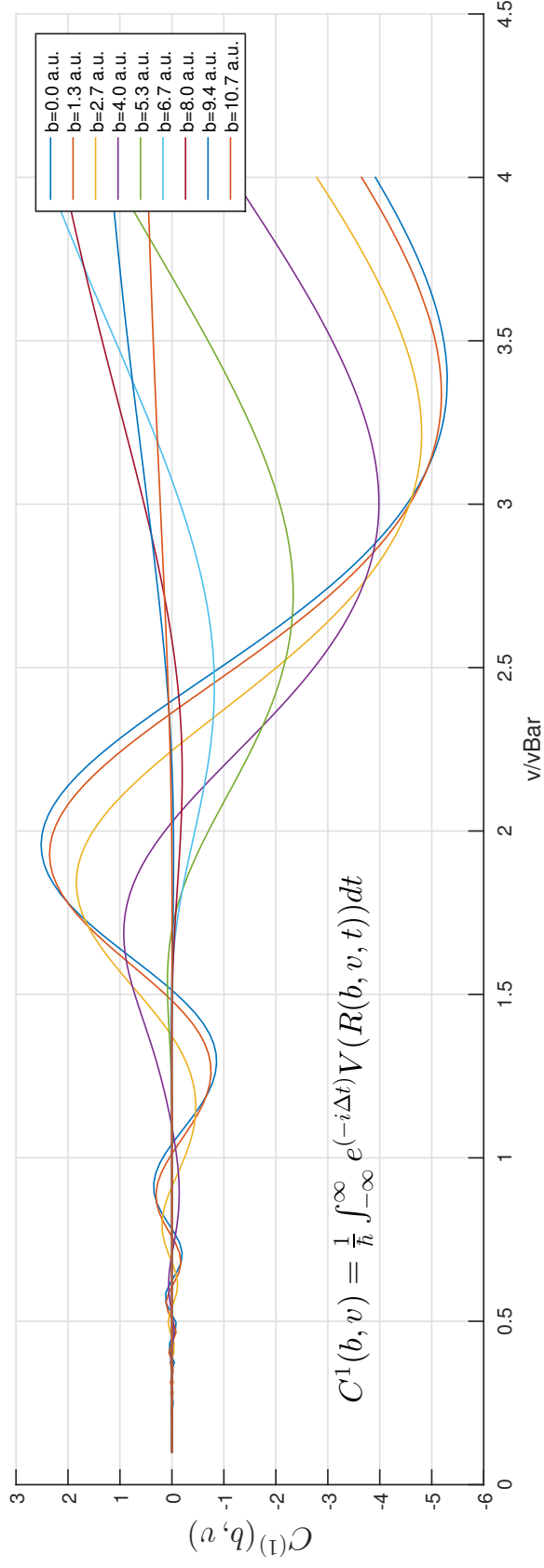


Figure 15. Verification of Limits and Convergence Across Velocities. RbHe at 300K is shown.

atomic potential energy surfaces only existed for $R > 3$ [au] (see Figure 16). To overcome this difficulty, the choice was made to introduce a turning point in the noble gas atom's trajectory where the atom's kinetic energy was equal to the potential energy of the adiabatic potential energy surface. That raised the question of which surface should be used, since the atoms are in a linear combination of different states. The choice was made to use an average of the $B\Sigma_{1/2}$ and $\Pi_{1/2}$ energy levels, which had the benefit of also resembling the ground state energy level, $X\Sigma_{1/2}$. Some of these surfaces had binding regions and therefore needed to be modified to make R a single-valued function of energy. The integration code used a lookup table to find the two nearest values of R and potential energy, then performed a linear interpolation to match the given value of kinetic energy to the turning point.

The phase of the probability amplitude in Equation 31 was set to zero at the point (time) of impact, and there was no phase discontinuity allowed throughout the duration of the interaction. This allowed the integrand in Equation 31 to be easily split into pure sine and cosine terms as before, simplifying the problem. Note that any constant phase offset applied to the oscillatory term of Equation 31 leaves the equation unchanged after taking the absolute square.

$$\begin{aligned}
P'_0(b, v) &= \left| \frac{i}{\hbar} \int_{-\infty}^{\infty} V(R(b, v, t)) e^{-i(\Delta t + \phi)} dt \right|^2 \\
&= \left| \frac{i}{\hbar} \int_{-\infty}^{\infty} V(R(b, v, t)) e^{-i\Delta t} e^{-i\phi} dt \right|^2 \\
&= \left| e^{-i\phi} \frac{i}{\hbar} \int_{-\infty}^{\infty} V(R(b, v, t)) e^{-i\Delta t} dt \right|^2 \\
&= \left| \frac{i}{\hbar} \int_{-\infty}^{\infty} V(R(b, v, t)) e^{-i\Delta t} dt \right|^2 \\
&= P_0(b, v)
\end{aligned} \tag{73}$$

IV. Results

4.1 Results Overview

Table 2 summarizes the types of calculations performed in this thesis, as well as the collisions pairs for which calculations were completed. The table also summarizes which data is compiled from other sources.

Table 2. Summary of calculations completed and data compiled. *Data from full quantum mechanical calculations covers temperatures up to approximately 400K. **Potassium experimental data inconsistent. *Data not available.**

	KHe	KNe	KAr	RbHe	RbNe	RbAr	CsHe	CsNe	CsAr
Analytic Integration, $V_{RG}(t)$	✓	✓	✓	✓	✓	✓	✓	✓	✓
Numeric Integration, $V_{RG}(t)$	✓	✓	✓	✓	✓	✓	✓	✓	✓
Numeric Integration, $V_{RG}(R)$	✓	✓	✓	✓	✓	✓	✓	✓	✓
Numeric Integration, $V_{RG}(R)$ Scaled V_0	✓	✓	✓	✓	✓	✓	✓	✓	✓
Numeric Integration, $V_{RG}(R)$ Scaled L	✓	✓	✓	✓	✓	✓	✓	✓	✓
Numeric Integration, $V_{RG}(R)$ Scaled W	✓	✓	✓	✓	✓	✓	✓	✓	✓
Numeric Integration, $V_{QM}(R)$	✓	✓	✓	✓	✓	✓	✓	✓	✓
Full Quantum Calculation* [5]	✓	✓	***	✓	✓	✓	✓	✓	✓
Experimental Data [3]	✓**	✓**	✓**	✓	✓	✓	✓	✓	***

4.2 Constants and Approximation Parameters

Table 3 lists the values of the various constants and approximations for all M+Ng pairs used in this thesis. Plots of the quantum mechanical coupling functions, $V_{QM}(R)$, along with the approximate coupling functions, $V_{RG}(R)$, for all M+Ng pairs are shown in Figure 16.

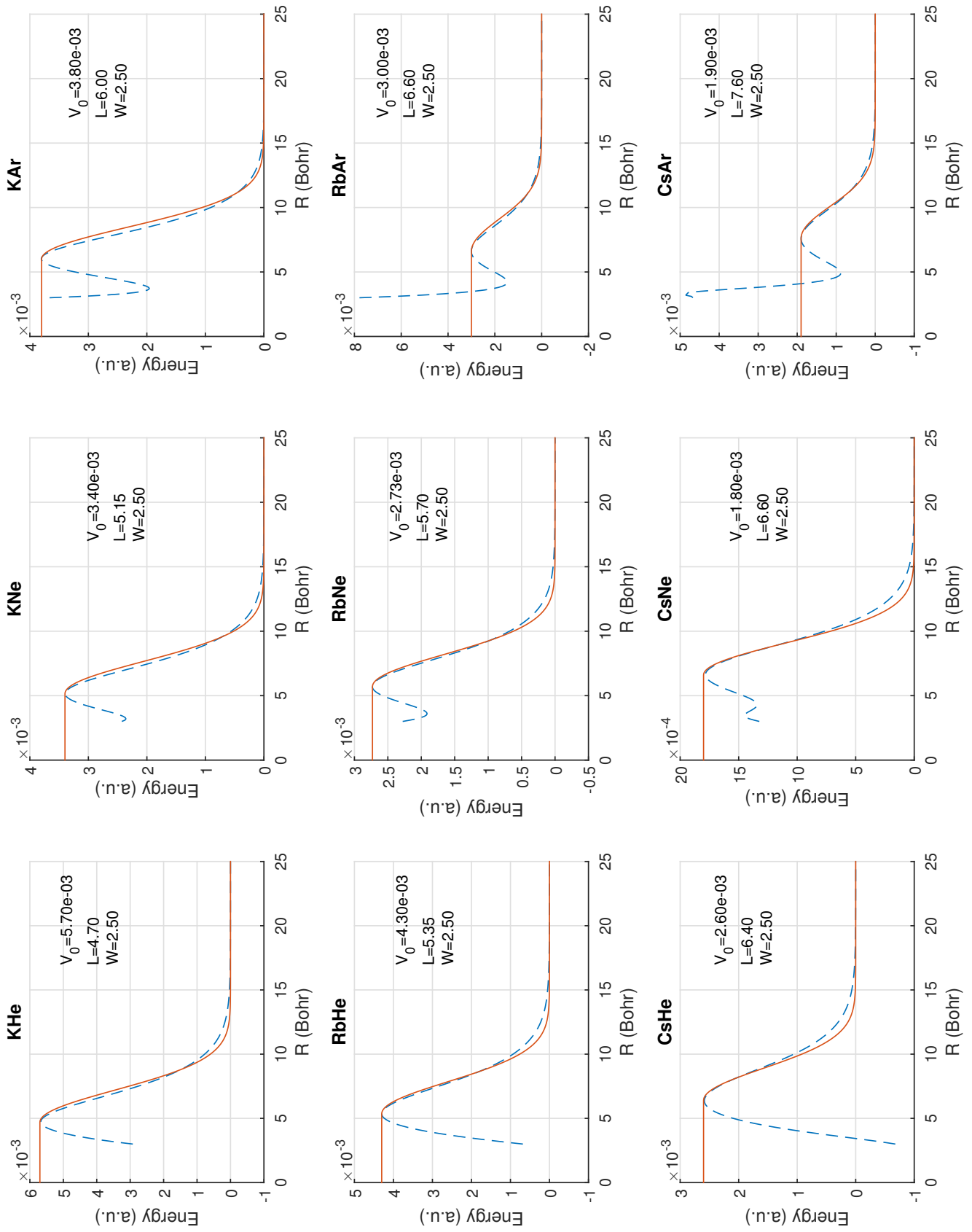


Figure 16. Radial Coupling Functions $V_{QM}(R)$ (dashed lines) and Approximations $V_{RG}(R)$ (solid lines), for All Atomic Species.

Table 3. Values used for atomic data constants and approximations. *CsAr collision cross section is estimated.

M+Ng Pair	Δ [rad/a.u. time]	Reduced Mass, μ	Collision Cross Section, σ_{QD}	L	W	V_0
KHe	2.63E-04	6.62E+03	285.3	4.7	2.5	0.0057
KNe	2.63E-04	2.43E+04	301.4	5.15	2.5	0.0034
KAr	2.63E-04	3.60E+04	342.1	6	2.5	0.0038
RbHe	1.08E-03	6.97E+03	306.4	5.35	2.5	0.0043
RbNe	1.08E-03	2.98E+04	323.2	5.7	2.5	0.00273
RbAr	1.08E-03	4.96E+04	364.2	6.6	2.5	0.003
CsHe	2.52E-03	7.08E+03	338.2	6.4	2.5	0.0026
CsNe	2.52E-03	3.19E+04	355.7	6.6	2.5	0.0018
CsAr	2.52E-03	5.60E+04	396*	7.6	2.5	0.0019

4.3 Comparison of Numerically Integrated $V_{RG}(t)$ and Analytic $V_{RG}(t)$

The results of the numerically integrated $V_{RG}(t)$ are compared with the results of calculations using the analytic integration of $V_{RG}(t)$ (see Section 2.10) in Figures 17, 18, and 19. This comparison helps provide validation for the code, as well as for the approximations made to arrive at the final analytic form. The comparison is a near perfect match for the rubidium and cesium pairs, but the results for the potassium pairs differ slightly between the analytic and numeric methods. The reason for this difference is likely related to a factor,

$$X_{max} = \frac{\Delta^2 L^2 \mu}{2k_B T} \quad (74)$$

that was introduced in [8] to simplify the analytic calculations. X_{max} was used to approximate a Meier G function in the analytic solution. This approximation is expected to hold for values of approximately $X_{max} > 30$, which holds for Rb and Cs, but not necessarily for K, see Table 4. Secondly, hypergeometric functions were approximated with a sin term multiplied by a decaying exponential. This approximation becomes much more accurate for values of approximately $X_{max} > 100$.

Table 4. Values of approximation parameter X_{max} for various M+Ng pairs at 300K and at 900K. Data in this thesis was calculated for temperatures ranging from 300K (higher adiabaticity) to 900K (lower adiabaticity).

M+Ng Pair	Δ [au]	L [au]	μ [au]	X_{max} (300K)	X_{max} (900K)
KHe	2.63E-04	4.70	6.62E+03	5.32	1.77
KNe	2.63E-04	5.15	2.43E+04	23.4	7.81
KAr	2.63E-04	6.00	3.60E+04	47.2	15.70
RbHe	1.08E-03	5.35	6.97E+03	123	41.0
RbNe	1.08E-03	5.70	2.98E+04	596	199
RbAr	1.08E-03	6.60	4.96E+04	1330	444
CsHe	2.52E-03	6.40	7.08E+03	973	324
CsNe	2.52E-03	6.60	3.19E+04	4670	1560
CsAr	2.52E-03	7.60	5.60E+04	10800	3620

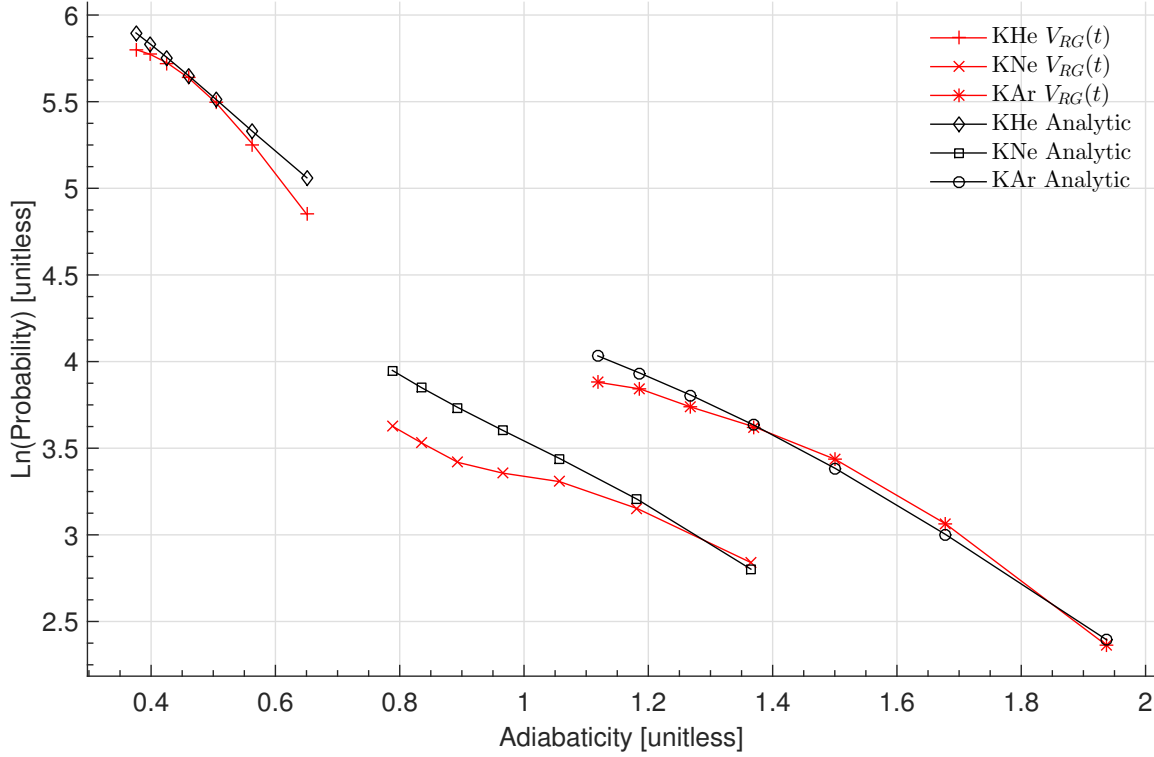


Figure 17. $\text{Ln}(\text{Probability})$ vs Adiabaticity for KHe, KNe, and KAr. Analytic vs. numeric integration of $V_{RG}(t)$.

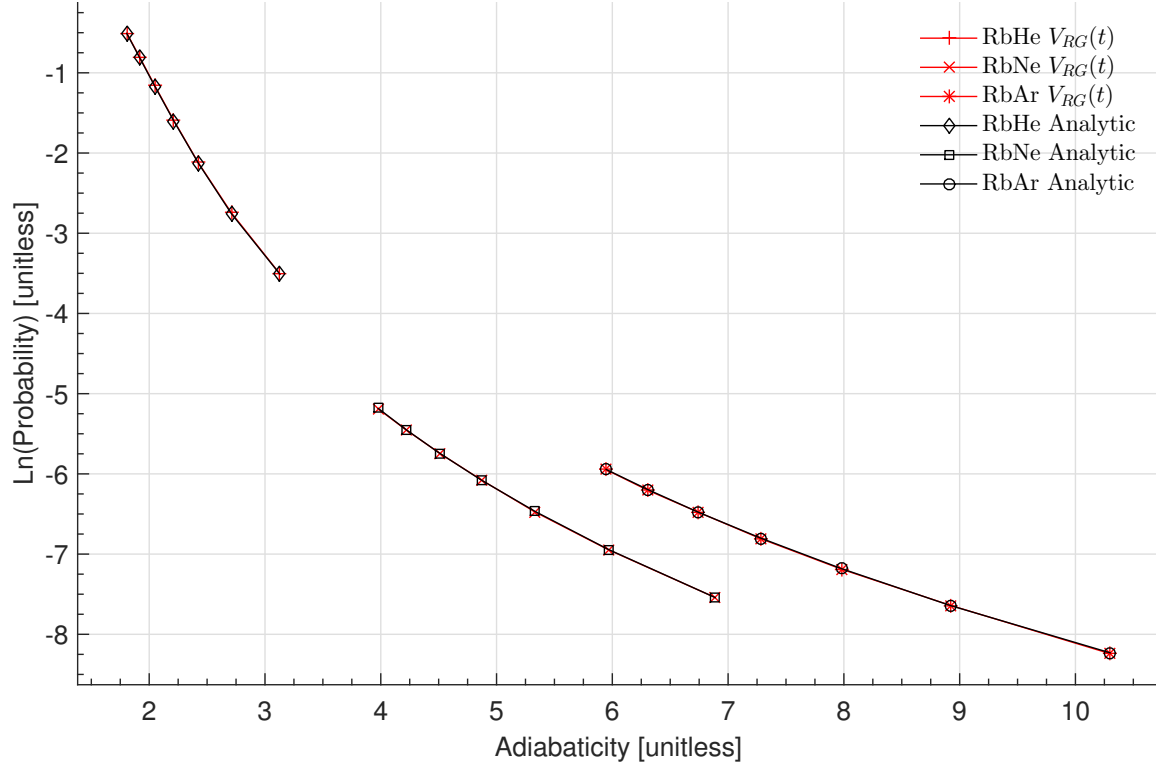


Figure 18. $\text{Ln}(\text{Probability})$ vs Adiabaticity for RbHe, RbNe, and RbAr. Analytic vs. numeric integration of $V_{RG}(t)$.

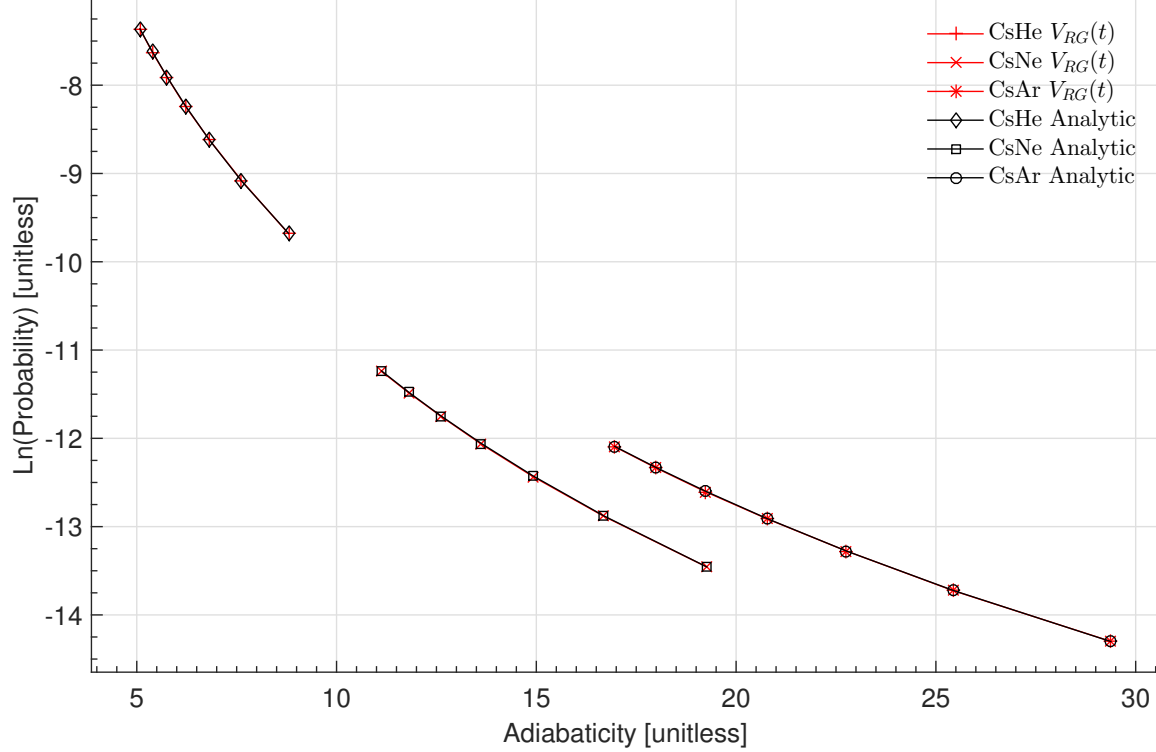


Figure 19. $\text{Ln}(\text{Probability})$ vs Adiabaticity for CsHe, CsNe, and CsAr. Analytic vs. numeric integration of $V_{RG}(t)$.

4.4 Comparison of Numerically Integrated $V_{RG}(t)$ and Numerically Integrated $V_{RG}(R)$

The results of the numerically integrated $V_{RG}(t)$ are compared with the results of the numerically integrated $V_{RG}(R)$ in Figures 20, 21, and 22. This comparison helps determine the effects of approximating the Gaussian width parameter s as W/\bar{v} . It also helps determine the effect of limiting the impact parameter range to values of $b \leq L$. The effect of integration beyond $b = L$ likely had little significance, based on observations of plots used to verify the chosen integration limits (similar to Figure 14, discussed in Section 3.4). Varying the width of the Gaussian does have a significant impact, and using a sort of thermal average width by using \bar{v} appears to be a good first choice. Although using \bar{v} does not fully account for the required transformation to go from $V_{RG}(R)$ to $V_{RG}(t)$, the shapes of the curves in the $\ln(P)$ vs. Adiabaticity plots seem to remain intact after the transformation. The \bar{v} scaling can easily be adjusted by a constant scale factor (e.g. $1.5\bar{v}$, etc.) to make the numerical results match experiment or to make $V_{RG}(t)$ match $V_{RG}(R)$ (see Section 5.3).

4.5 Comparison of Numerically Integrated Rectangular-Gaussian $V_{RG}(R)$ and Numerically Integrated Quantum Mechanical $V_{QM}(R)$

The results of the numerically integrated $V_{RG}(R)$ are compared with the results of the numerically integrated $V_{QM}(R)$ in Figures 23, 24, and 25. These plots raise what is possibly the biggest question that stemmed from the results of this thesis. That question is, why did the radial coupling surfaces that are the most likely to be the most correct produce the highest offset error? Unfortunately, the direct effects of replacing the radial coupling functions with a square Gaussian approximation are not clear here, due to the required energy conservation condition in the use of $V_{QM}(R)$ (see Section 3.6). It is possible to impose the energy conservation condition while us-

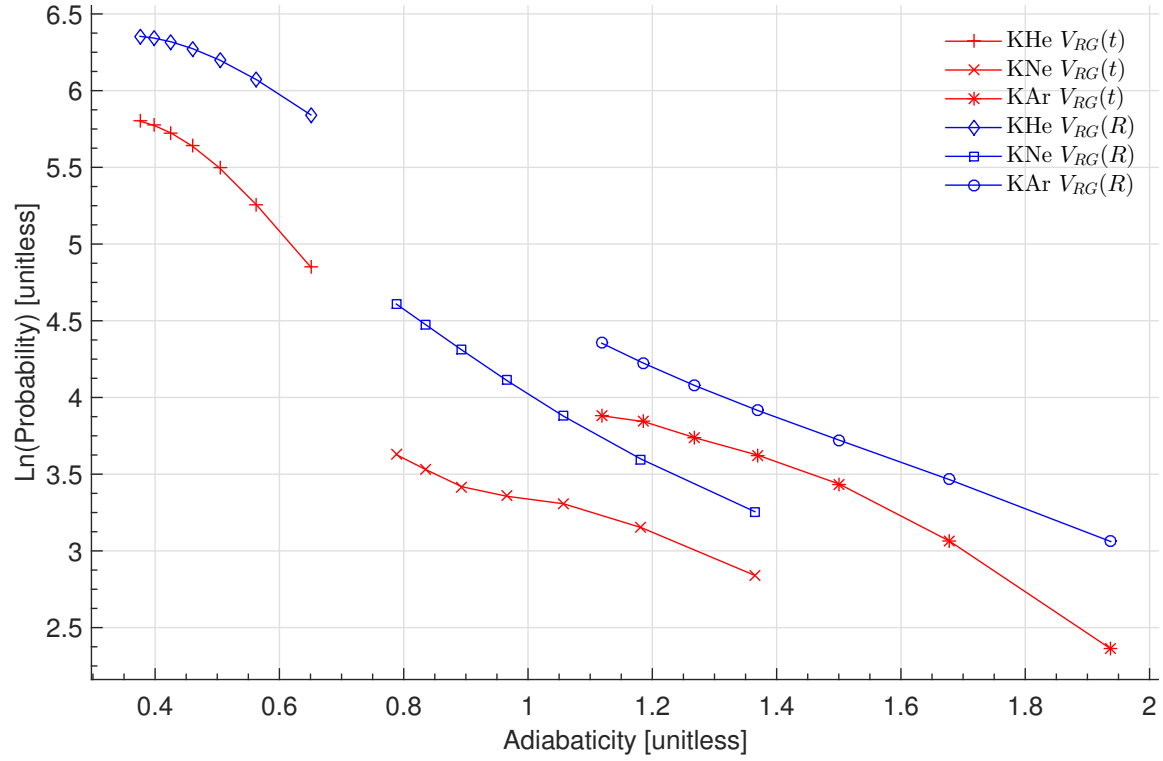


Figure 20. $\text{Ln}(\text{Probability})$ vs Adiabaticity for KHe, KNe, and KAr. Numeric integration of $V_{RG}(t)$ vs. numeric integration of $V_{RG}(R)$.

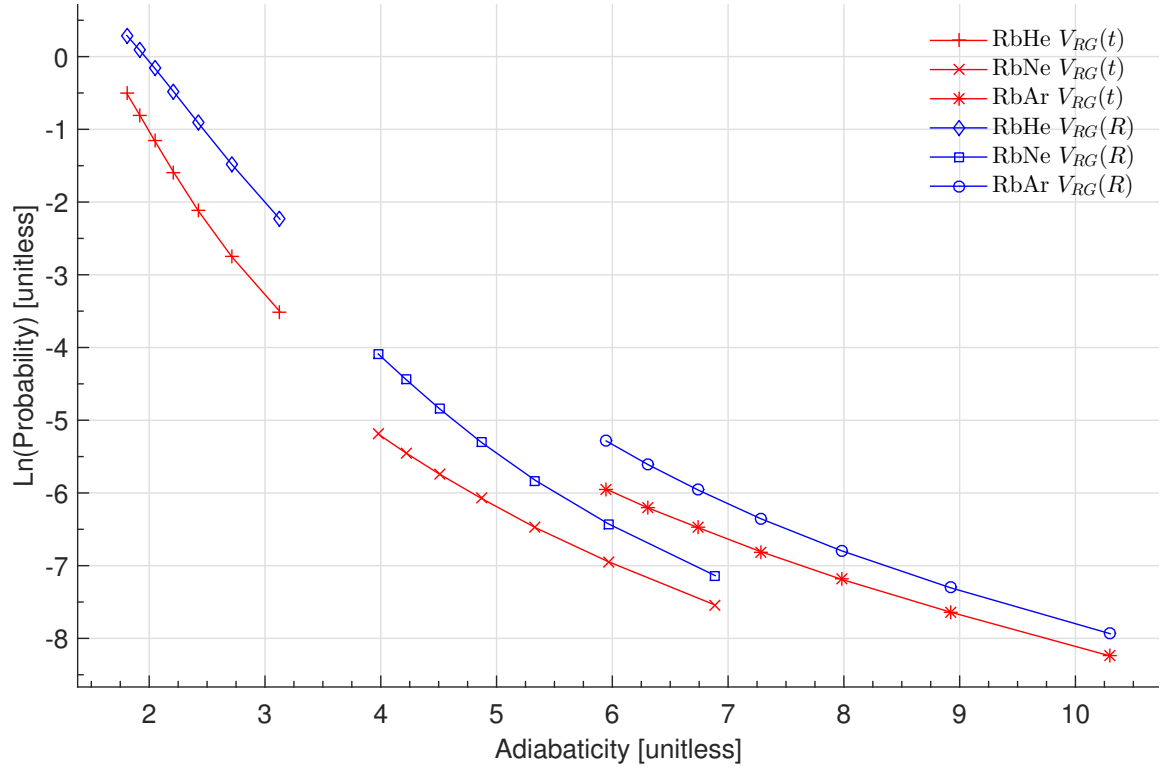


Figure 21. $\text{Ln}(\text{Probability})$ vs Adiabaticity for RbHe, RbNe, and RbAr. Numeric integration of $V_{RG}(t)$ vs. numeric integration of $V_{RG}(R)$.

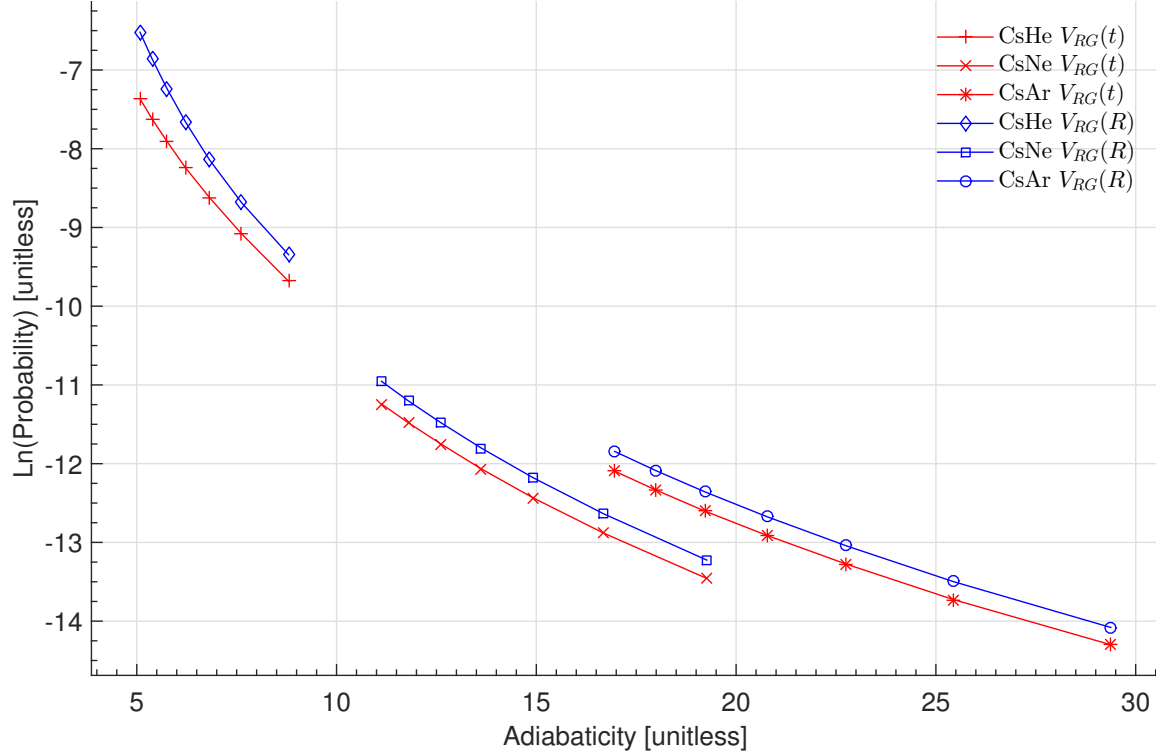


Figure 22. $\text{Ln}(\text{Probability})$ vs **Adiabaticity** for CsHe, CsNe, and CsAr. **Numeric integration of $V_{RG}(t)$ vs. numeric integration of $V_{RG}(R)$.**

ing $V_{RG}(R)$. This was not fully investigated here, but some investigation was made. As shown in Figure 26 for RbNe, the results using $V_{RG}(R)$ modified with energy conservation approach the original results using $V_{RG}(R)$ (without energy conservation) at low adiabaticities (higher velocities), and approach the results using $V_{QM}(R)$ (with energy conservation) at high adiabaticities (lower velocities). There are a vast number of possible forms of the radial coupling function $V(R)$, and the results can vary drastically based on which form is chosen. (Efforts in this thesis eventually became focused on four forms; analytic integration of $V_{RG}(t)$, numeric integration of $V_{RG}(t)$, numeric integration of $V_{RG}(R)$, and numeric integration of $V_{QM}(R)$, with the approximations matched to $V_{QM}(R)$).

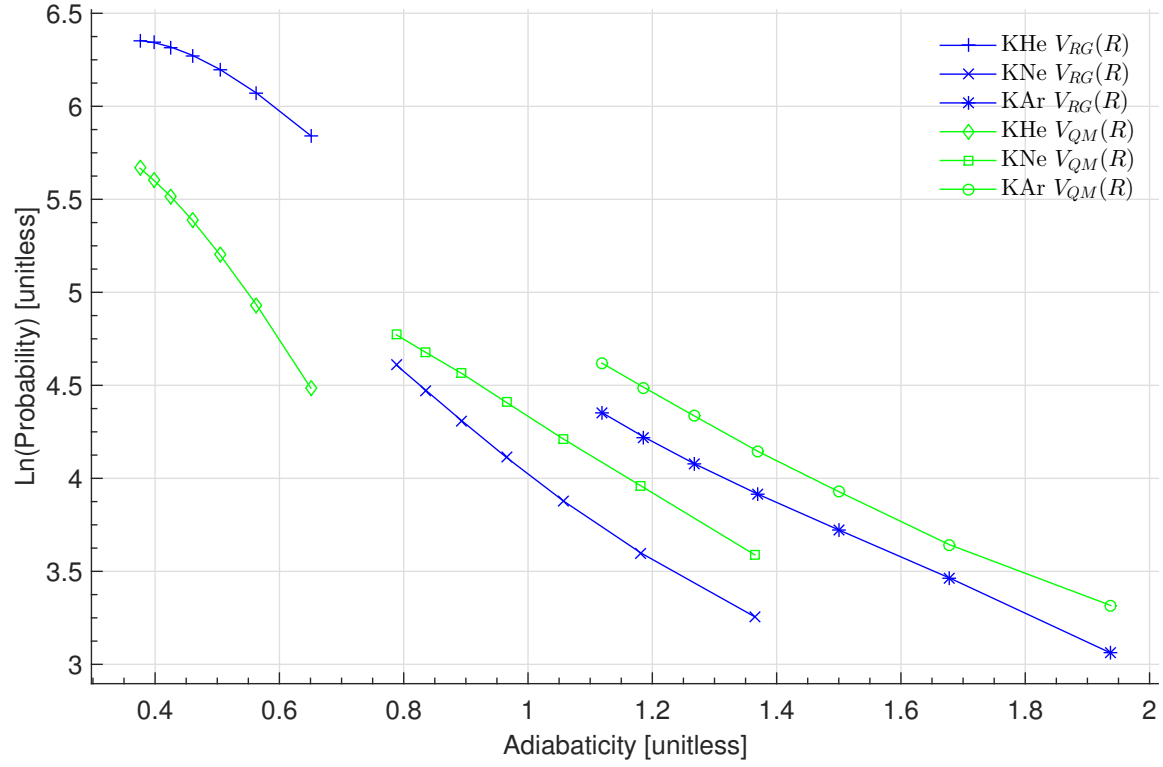


Figure 23. $\text{Ln}(\text{Probability})$ vs Adiabaticity for KHe, KNe, and KAr. Numeric integration of $V_{RG}(R)$ vs. numeric integration of $V_{QM}(R)$.

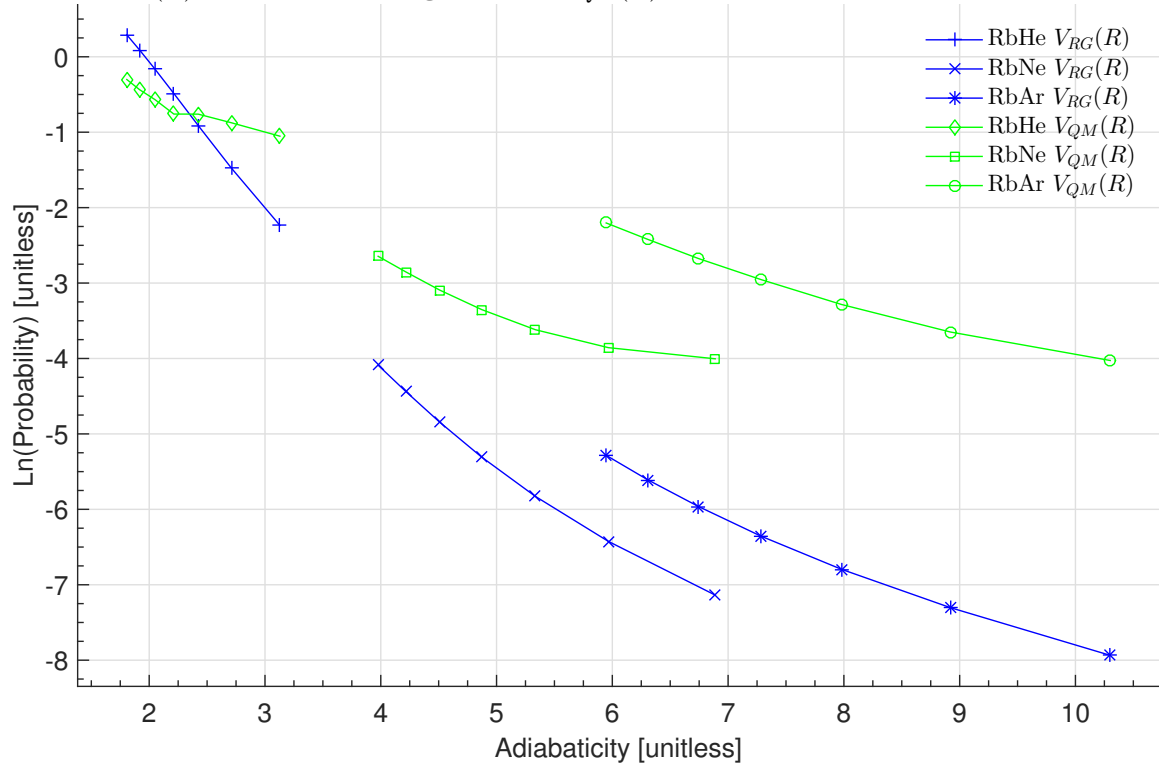


Figure 24. $\text{Ln}(\text{Probability})$ vs Adiabaticity for RbHe, RbNe, and RbAr. Numeric integration of $V_{RG}(R)$ vs. numeric integration of $V_{QM}(R)$.

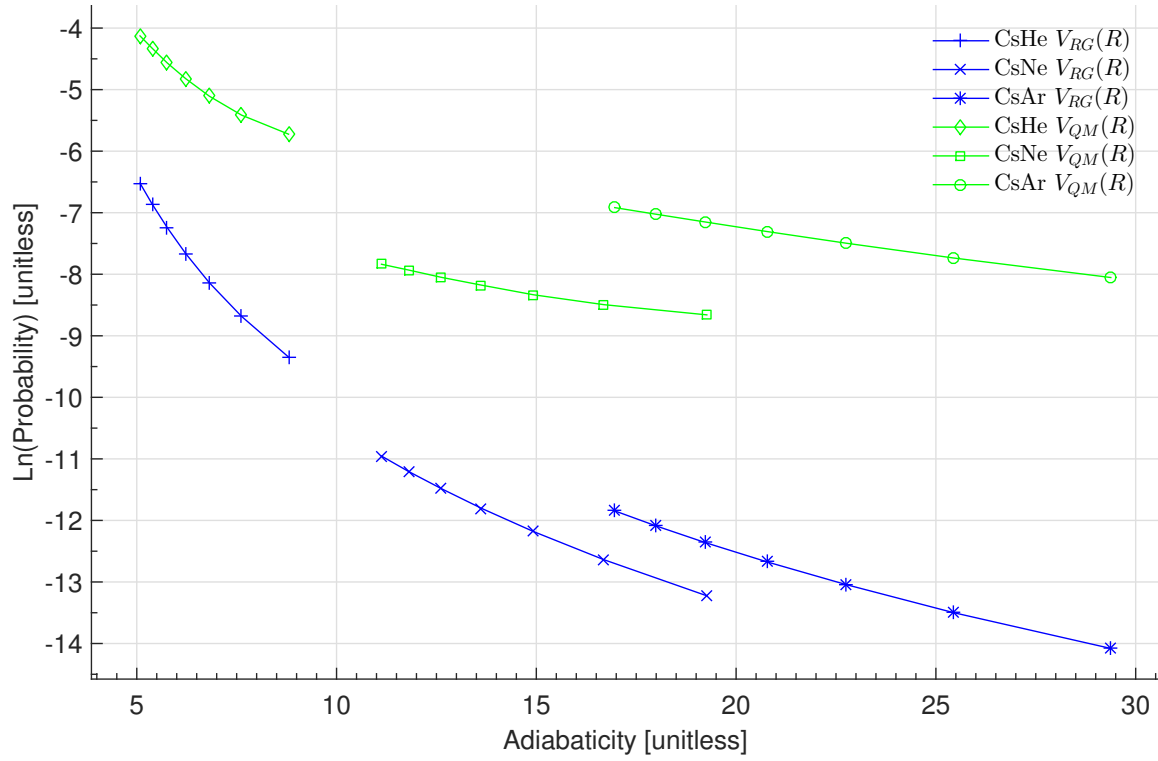


Figure 25. $\text{Ln}(\text{Probability})$ vs Adiabaticity for CsHe, CsNe, and CsAr. Numeric integration of $V_{RG}(R)$ vs. numeric integration of $V_{QM}(R)$.

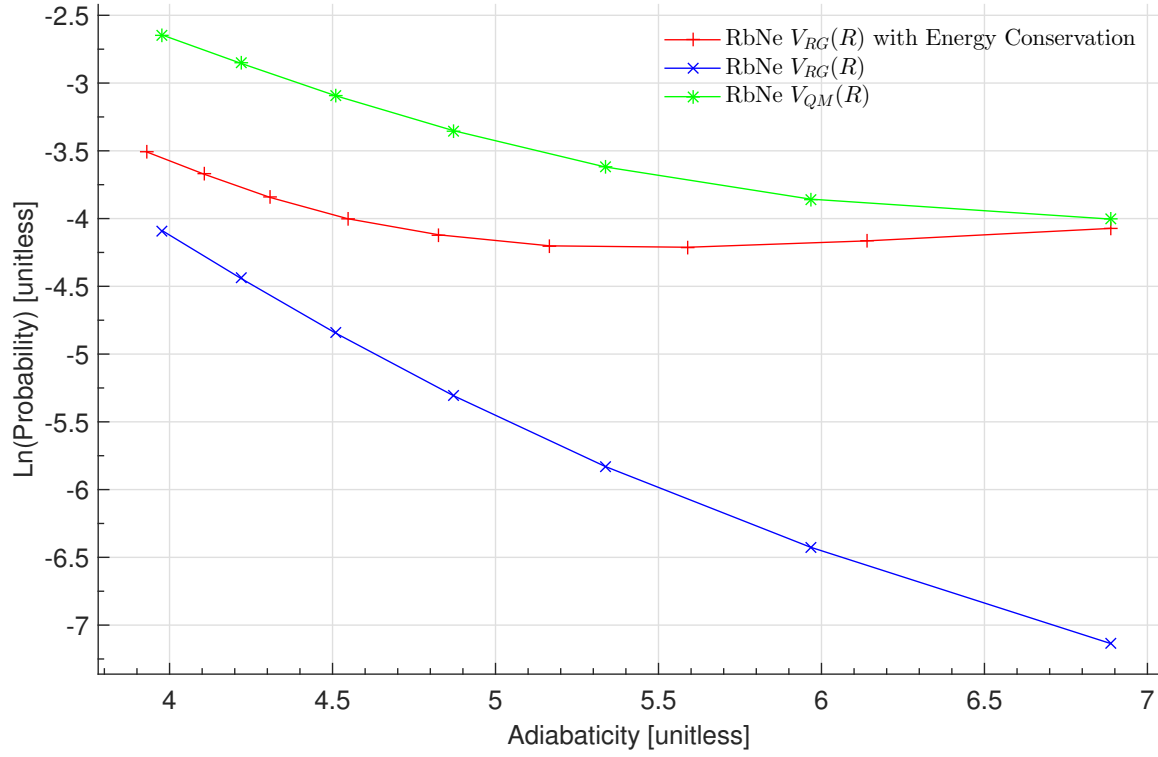


Figure 26. $\text{Ln}(\text{Probability})$ vs Adiabaticity for RbNe. Investigating the effects of the energy conservation condition by modifying the numeric integration of $V_{RG}(R)$ with energy conservation. Notice that the results using the modified $V_{RG}(R)$ approach the (unmodified) $V_{RG}(R)$ results at low adiabaticities (higher velocities), and approach the $V_{QM}(R)$ results at high adiabaticities (lower velocities).

V. Discussion

5.1 Comparison with Experimental Data - Support for Validity of Potential Energy Surfaces

As mentioned previously, the adiabatic electronic potential energy surfaces were calculated using a many-body numerical routine by Blank [1]. These surfaces were then converted to diabatic surfaces to yield adiabatic electronic potential energy surfaces, along with radial coupling functions by Lewis [5]. Lewis also calculated temperature dependent cross sections with a FORTRAN numerical routine using a full quantum mechanical approach. These cross sections can be used along with the quantum defect cross sections to predict the total probability of electronic energy level transition during a collision (see Equation 35). These full-quantum predictions can be used to validate the radial coupling surfaces that form the basis of the semi-classical model in this thesis, which in turn can provide insight into the effect of the approximations made in this thesis. This data is plotted for comparison in Figures 27, 28, and 29, for K, Rb, and Cs respectively. These figures show that a fully quantum mechanical approach to calculating the probabilities comes very close to predicting the experimental results for the potassium pairs and for the rubidium pairs, although the fit is not as good for cesium pairs. This suggests that the radial coupling functions are not a likely source for the discrepancy between the semi-classical models predictions and the experimental results.

5.2 Choice of Energy Level for Conservation of Energy in $V_{QM}(R)$

As mentioned in Section 3.6, the quantum mechanical (non-approximated) radial coupling functions $V_{QM}(R)$ did not extend to $R = 0$, which caused the introduction of a turning point based on conservation of energy. This led to the requirement to

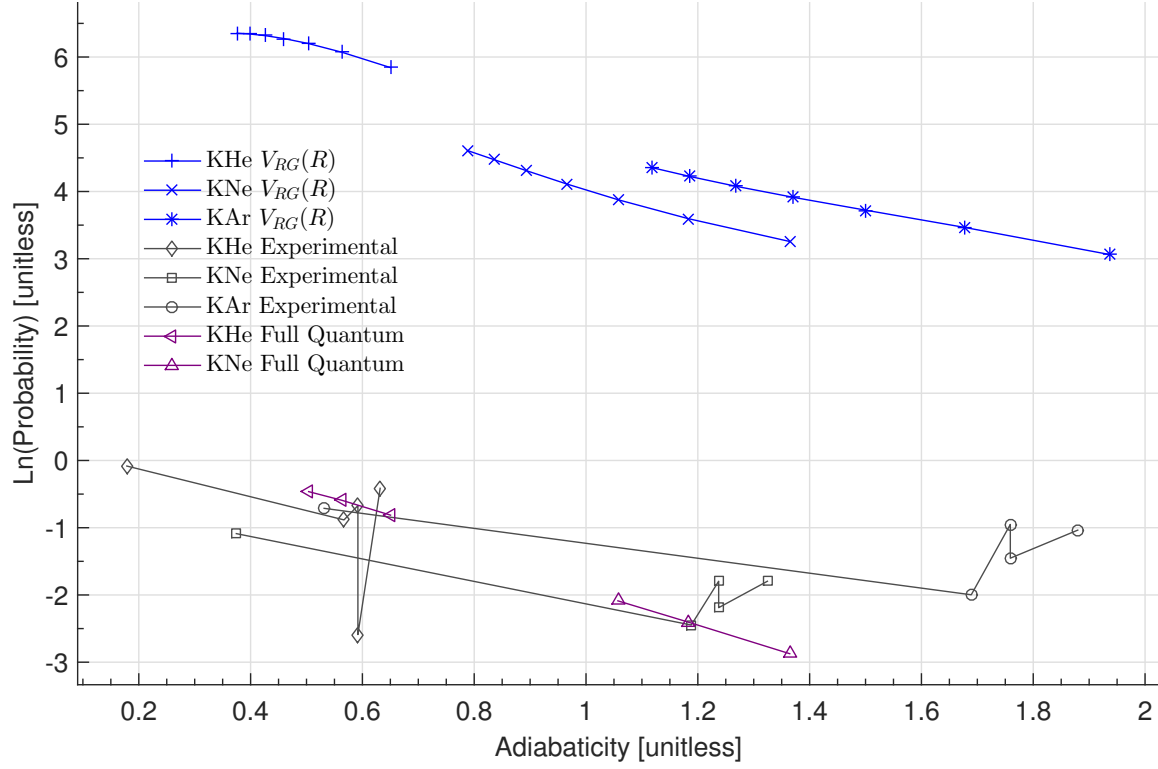


Figure 27. $\text{Ln}(\text{Probability})$ vs Adiabaticity for KHe, KNe, and KAr. Numeric integration of $V_{RG}(R)$ vs. Experimental data and Full Quantum Approach.

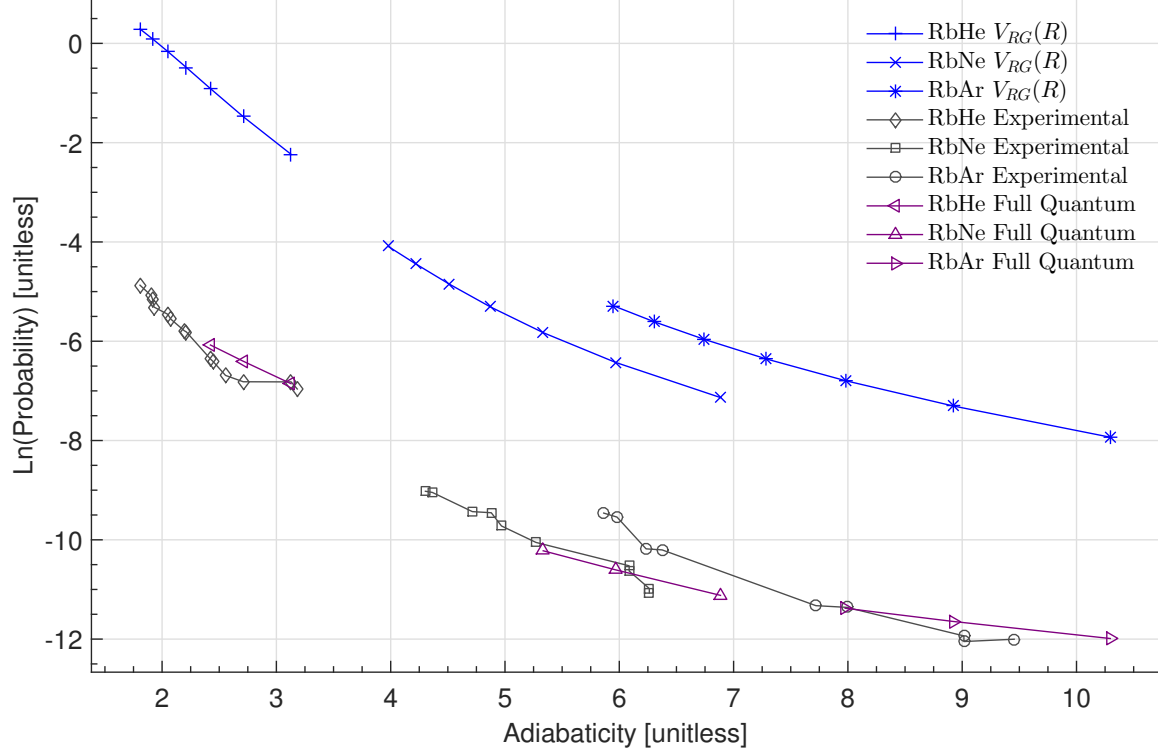


Figure 28. $\text{Ln}(\text{Probability})$ vs Adiabaticity for RbHe, RbNe, and RbAr. Numeric integration of $V_{RG}(R)$ vs. Experimental data and Full Quantum Approach.

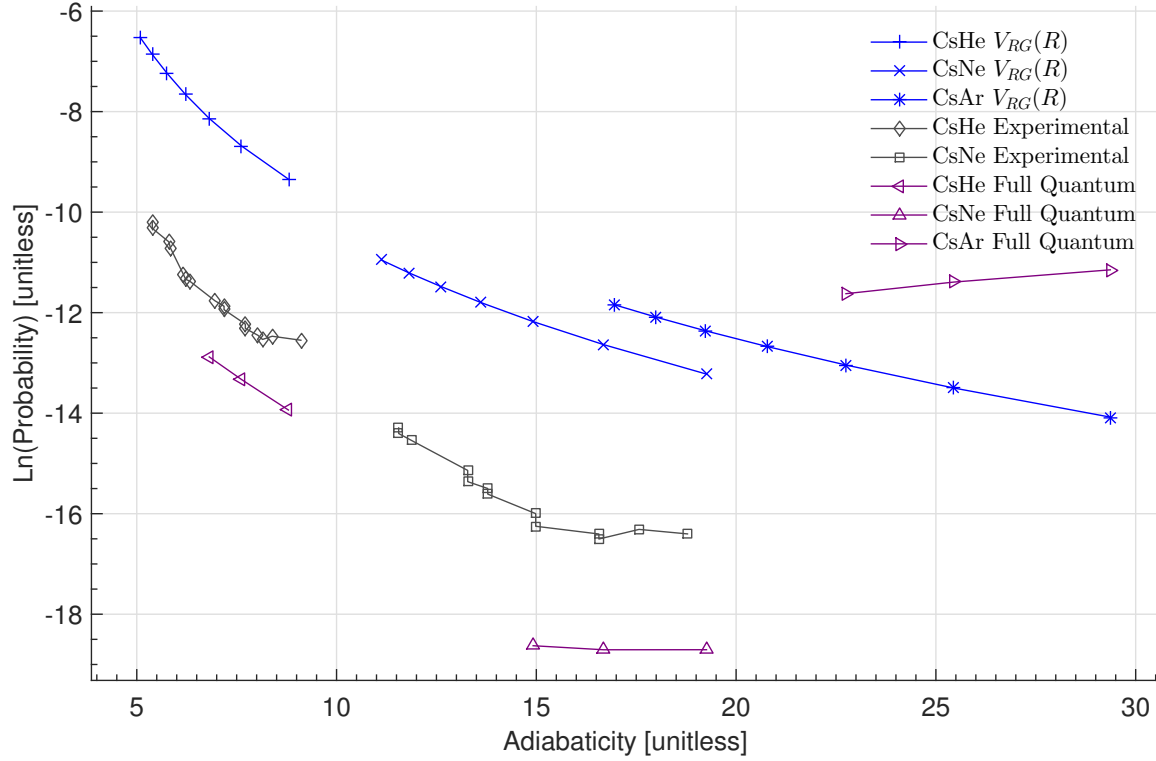


Figure 29. $\text{Ln}(\text{Probability})$ vs Adiabaticity for CsHe, CsNe, and CsAr. Numeric integration of $V_{RG}(R)$ vs. Experimental data and Full Quantum Approach.

choose which energy potential should be used. The decision was made to use an average of the $B\Sigma_{1/2}$ and $\Pi_{1/2}$ energy levels. This average also had the benefit of (loosely) resembling the ground state energy level, $X\Sigma_{1/2}$. See Figure 30 for a plot of the adiabatic electronic potential energy surfaces, along with the radial coupling functions. See Figure 31 for a plot showing the effect of the choice of energy level for rubidium and three different noble gas species. The choice of energy level did affect the shape of the plot, but it did not change the offset enough to imply that choosing the wrong surface could fully account for the discrepancy between the experimental results and the results of the semi-classical model.

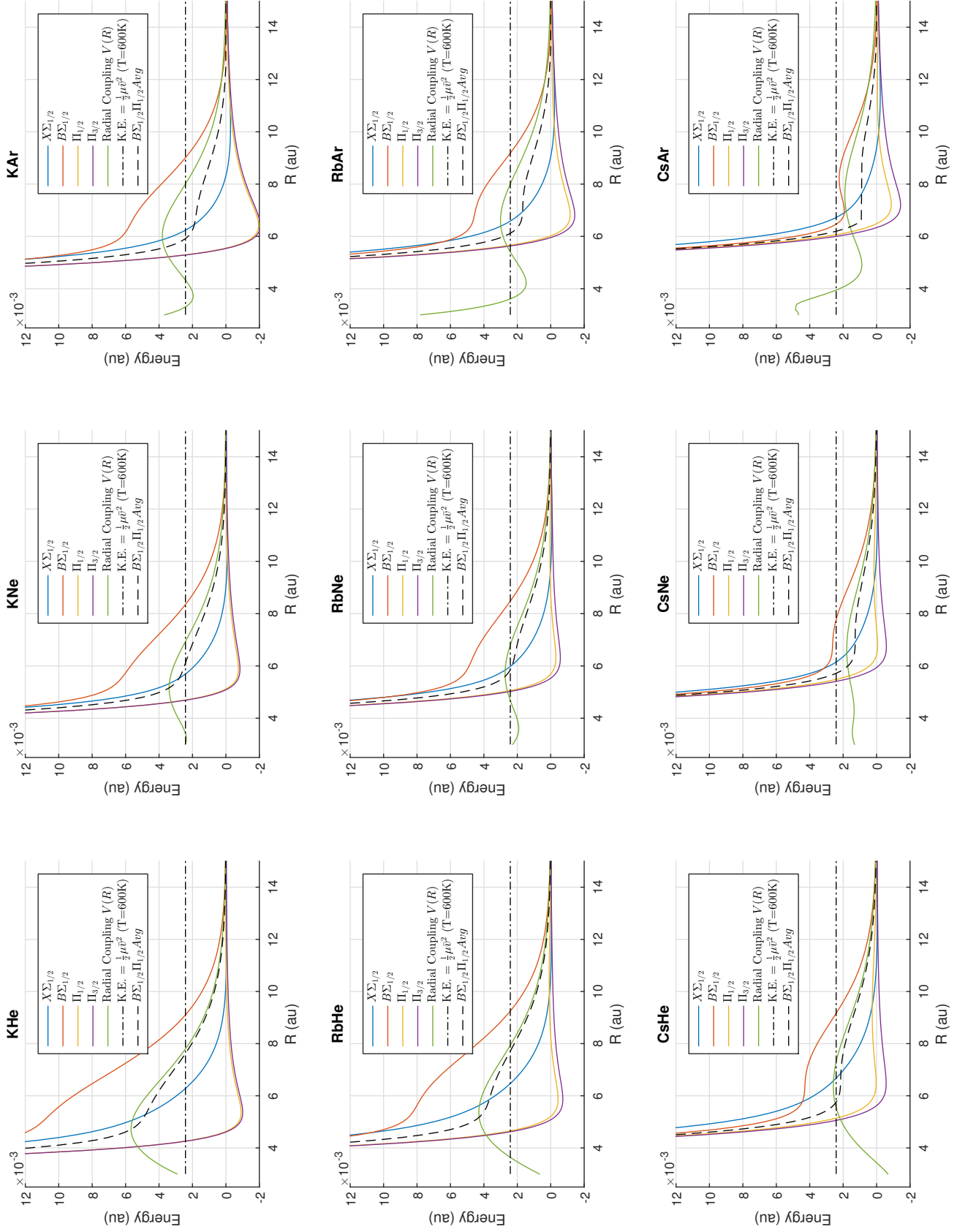


Figure 30. Energy levels of all M+Ng combinations, relative to their asymptotic limits. An average between the $B\Sigma_{1/2}$ and $\Pi_{1/2}$ energy levels was chosen to determine the turning point for rate calculations using $V_{QM}(R)$.

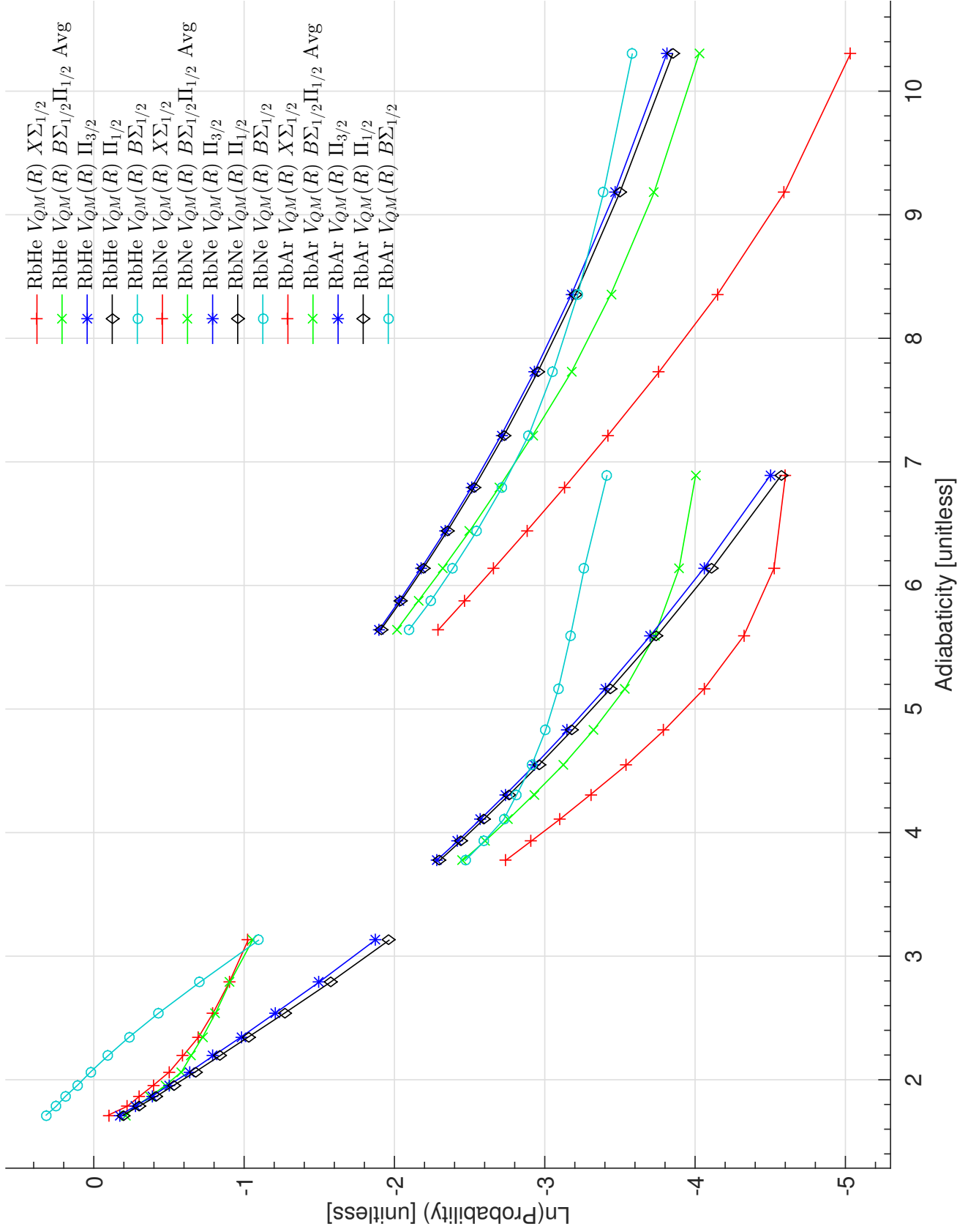


Figure 31. Resulting Transition Probabilities for Various Choices of Conserved Energy Level. RbHe results are the group of lines on the left, RbNe results are the group in the center, and RbAr are on the right side of the figure.

5.3 Scaling V_0 , L , and W to Make the Numerical Results for $V_{RG}(R)$ Match Experimental Results

The results of the probability calculations turn out to be very sensitive to the radial coupling function approximation's fit parameters W , V_0 , and L . Through trial and error, it was found that applying a scale factor of $0.12 \approx 1/8.3$ to V_0 in $V_{RG}(R)$ changed the predicted electron fine structure transition probability in a collision between rubidium and neon by a factor of approximately $0.014 \approx 1/69$. This brought the predicted results nearly in line with the experimental results. The decrease in probability was even across the calculated adiabaticity range (temperature range of 300K to 900K). This V_0 scale factor was then applied to all other M+Ng combinations, and the results are shown in Figures 33, 34, and 35, for potassium, rubidium, and cesium, respectively. The combined results for all M+Ng pairs are shown in Figure 36. The change in probability was approximately $1/69$, and was equal across all collision pairs and all adiabaticities. The scaled radial coupling function is shown in Figure 32.

Through trial and error, it was also found that applying a scale factor of $0.03 \approx 1/33$ to L in $V_{RG}(R)$ changed the predicted electron fine structure transition probability in a collision between rubidium and neon by an average factor of approximately $0.035 \approx 1/28$. This aligned the central values (at temperature = 600K, adiabaticity ≈ 5.2) of the predicted results and the experimental results. The shift in probability depended heavily on adiabaticity, α , with $\alpha(300K)$ decreasing by a factor of approximately $0.008 \approx 1/126$, while $\alpha(900K)$ decreased by a factor of approximately $0.08 \approx 1/12$. This L scale factor was then applied to all other M+Ng combinations, and the results are shown in Figures 38, 39, and 40, for potassium, rubidium, and cesium, respectively. The combined results for all M+Ng pairs are shown in Figure 41. The effects of the scaled L varied greatly across collision pair, as well as across

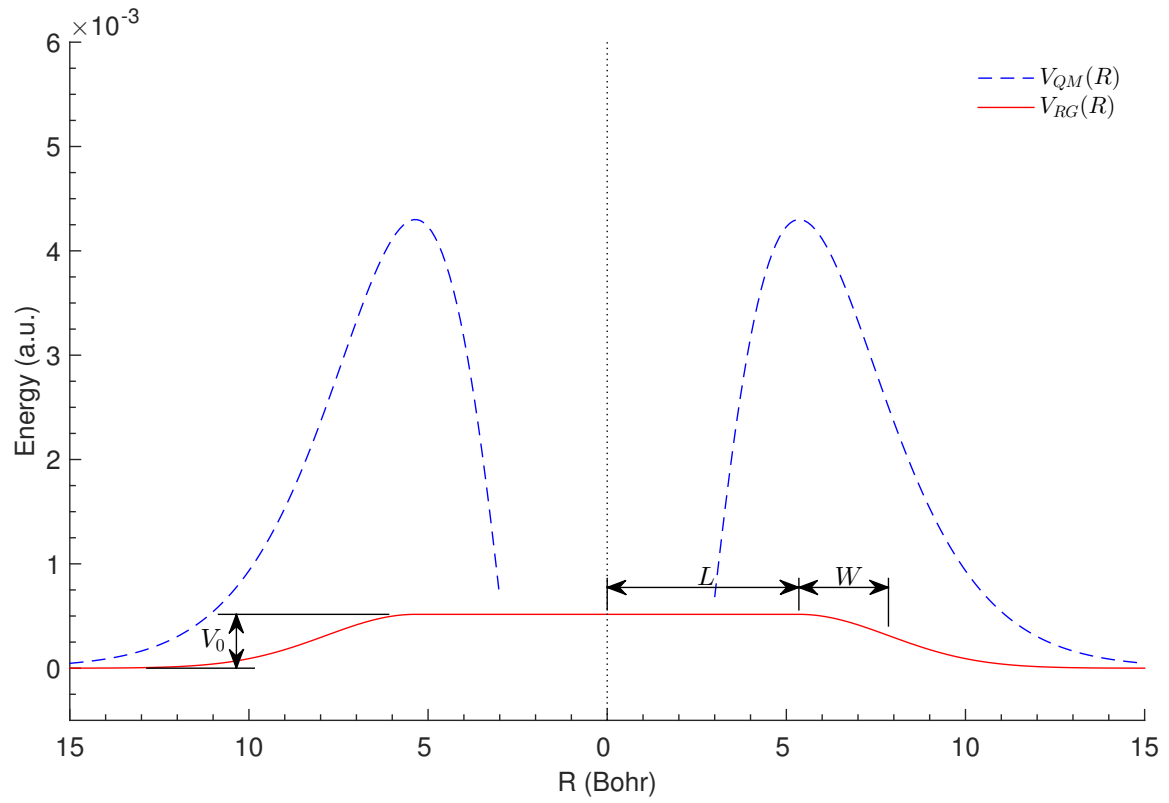


Figure 32. $V_{RG}(R)$ radial coupling function with fit parameter, V_0 , scaled by a factor of 0.12. Data is shown for RbHe, and $V_{QM}(R)$ is plotted for comparison.

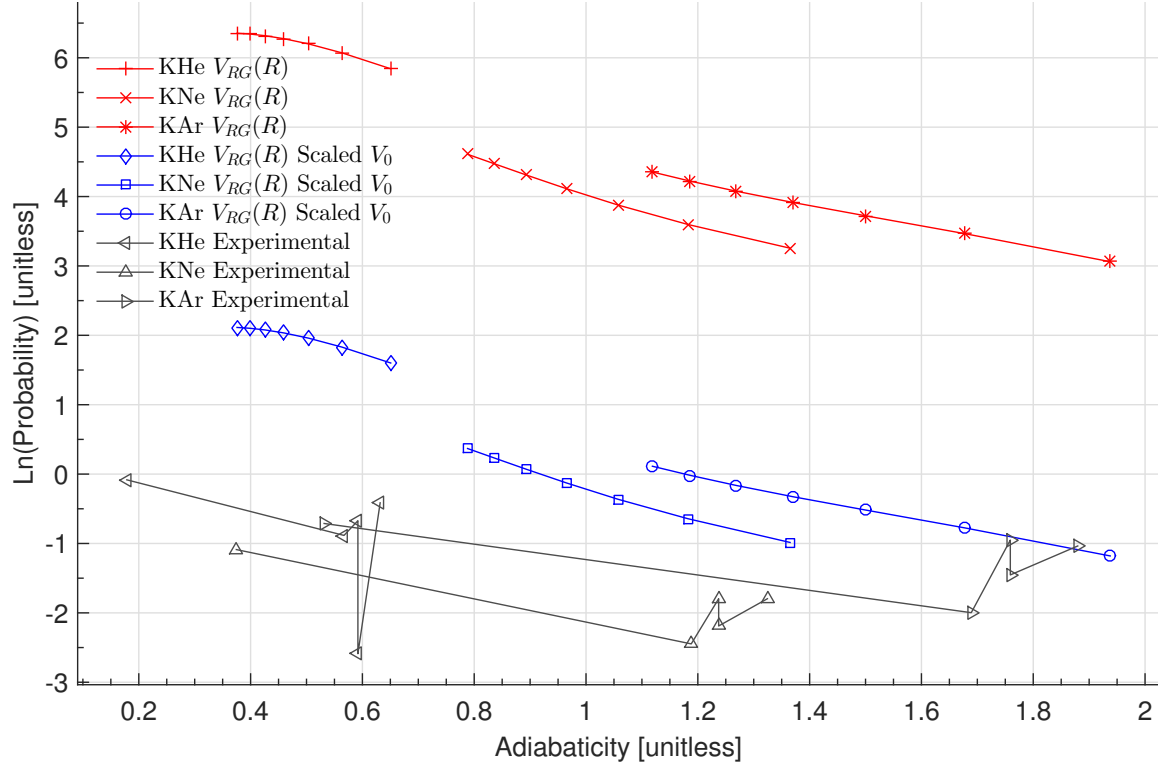


Figure 33. Scaled $V_{RG}(R)$ radial coupling fit parameter, V_0 , for KHe, KNe, and KAr. Experimental data is plotted for comparison. V_0 is scaled by a factor of 0.12.

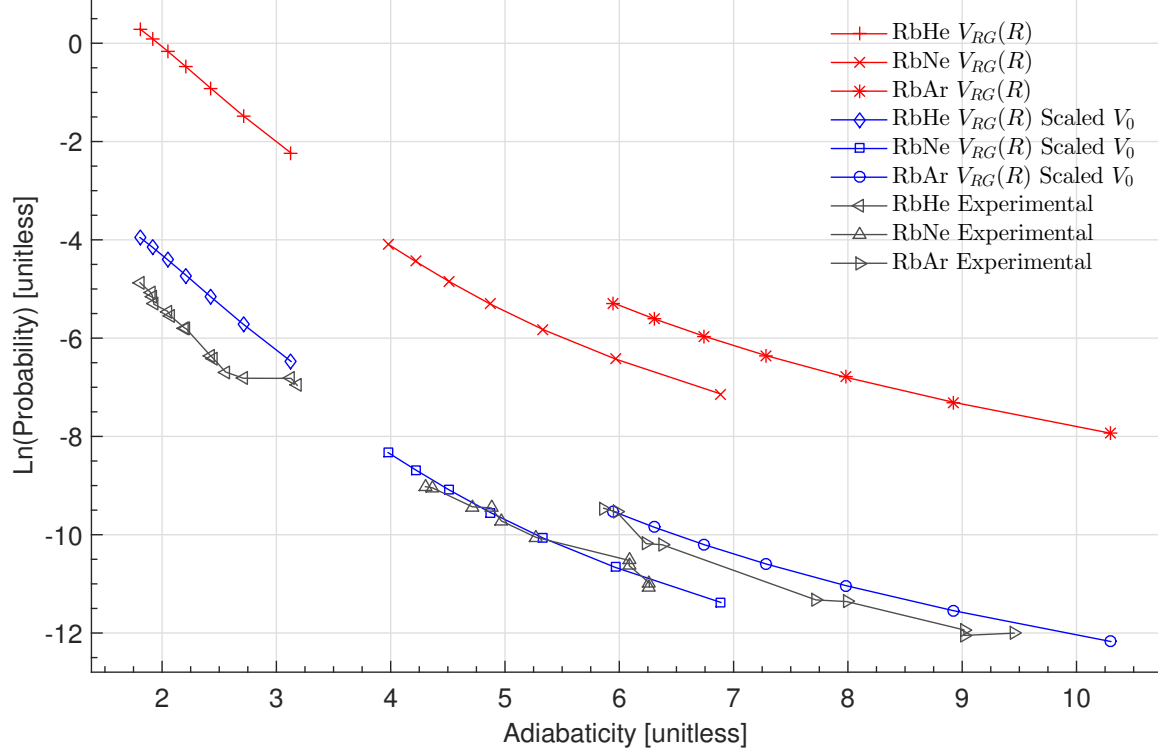


Figure 34. Scaled $V_{RG}(R)$ radial coupling fit parameter, V_0 , for RbHe, RbNe, and RbAr. Experimental data is plotted for comparison. V_0 is scaled by a factor of 0.12.

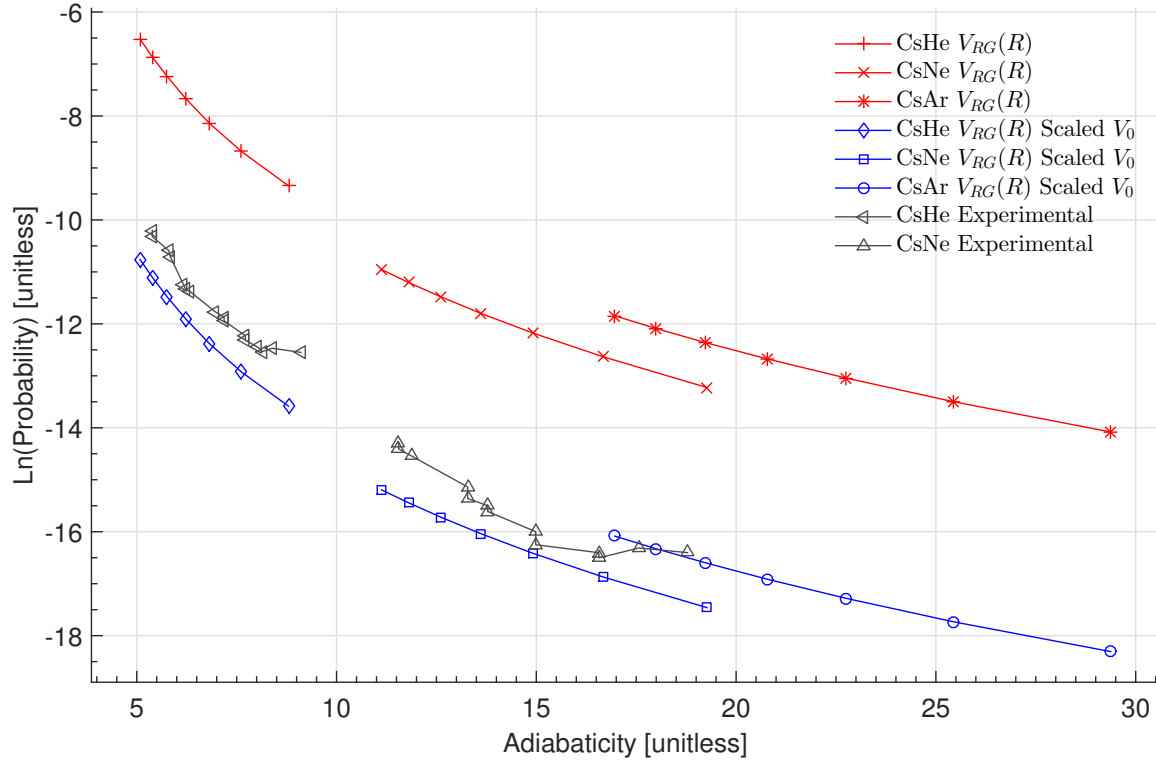


Figure 35. Scaled $V_{RG}(R)$ radial coupling fit parameter, V_0 , for CsHe, CsNe, and CsAr. Experimental data is plotted for comparison. V_0 is scaled by a factor of 0.12.

adiabaticity, with changes ranging from a factor of $1/2.4$ for KNe at 300K, to $1/187$ for CsAr at 300K. The scaled radial coupling function is shown in Figure 37.

It was then also found, through trial and error, that applying a scale factor of 2.6 to W in $V_{RG}(R)$ decreased the predicted electron fine structure transition probability in a collision between rubidium and neon by an average factor of approximately $0.013 \approx 1/78$. This brought the predicted results for RbNe nearly in line with the experimental results. The shift in probability depended on adiabaticity, with $\alpha(300K)$ decreasing by a factor of approximately $0.018 \approx 1/55$, while $\alpha(900K)$ decreased by a factor of approximately $0.009 \approx 1/111$. This scale factor was then applied to all other M+Ng combinations, and the results are shown in Figures 43, 44, and 45, for potassium, rubidium, and cesium, respectively. The results varied across collision pairs and adiabaticities, but the variation was not as large as it was for the scaling

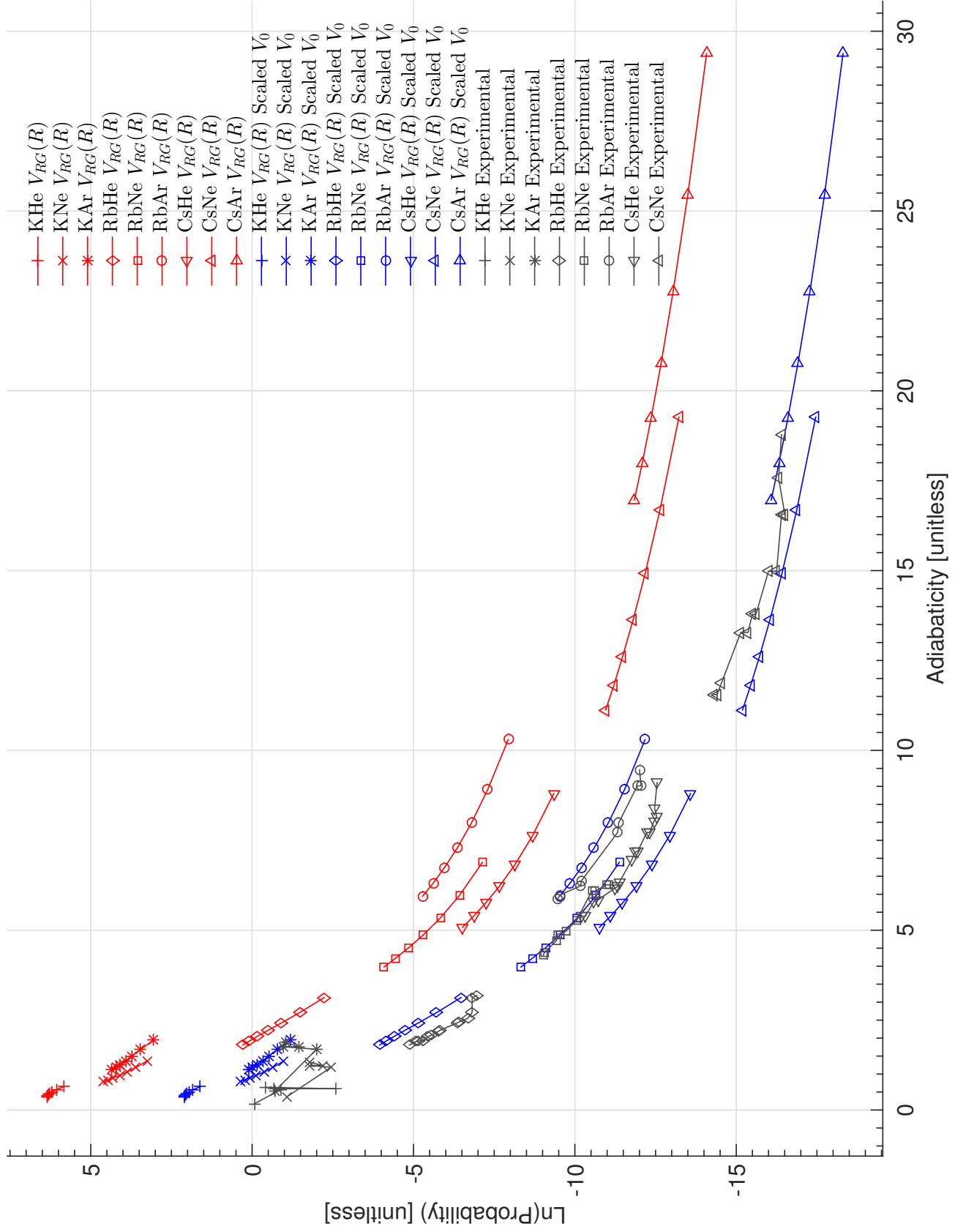


Figure 36. Scaled $V_{RG}(R)$ radial coupling fit parameter, V_0 , for all M+Ng pairs. Experimental data is plotted for comparison. V_0 is scaled by a factor of 0.12.

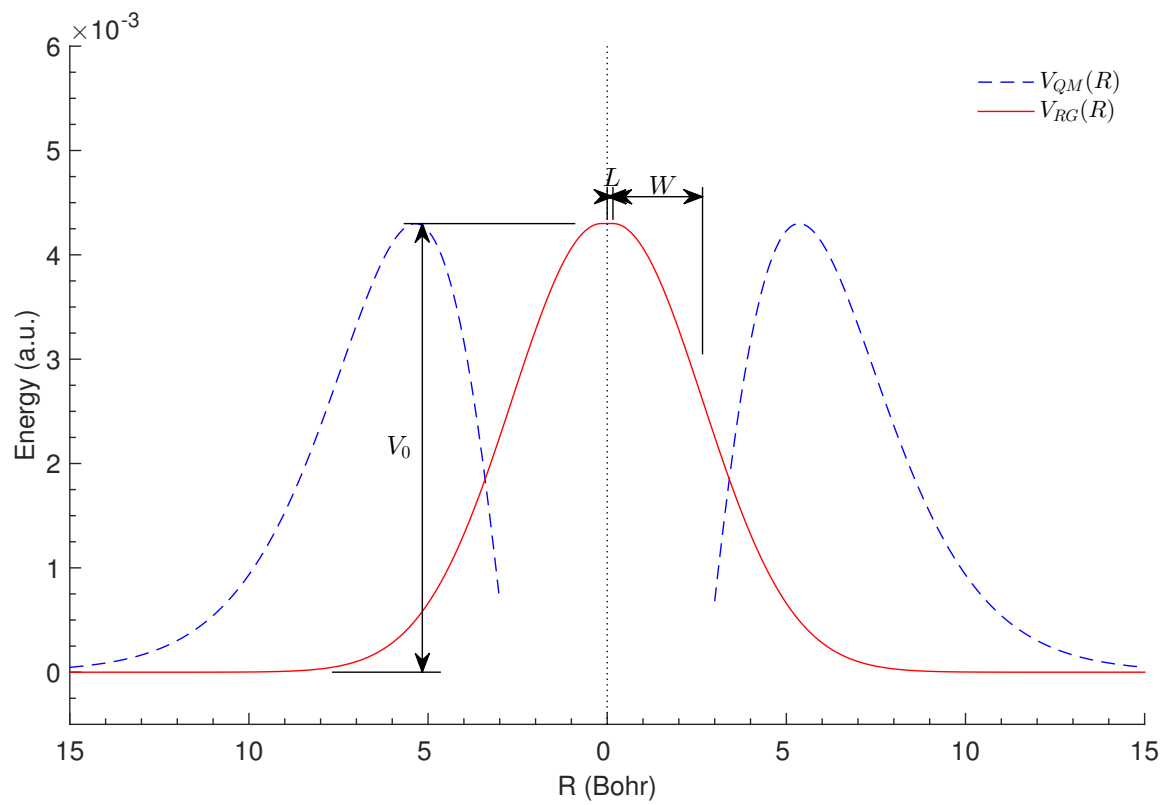


Figure 37. $V_{RG}(R)$ radial coupling function with fit parameter, L , scaled by a factor of 0.03. Data is shown for RbHe, and $V_{QM}(R)$ is plotted for comparison.

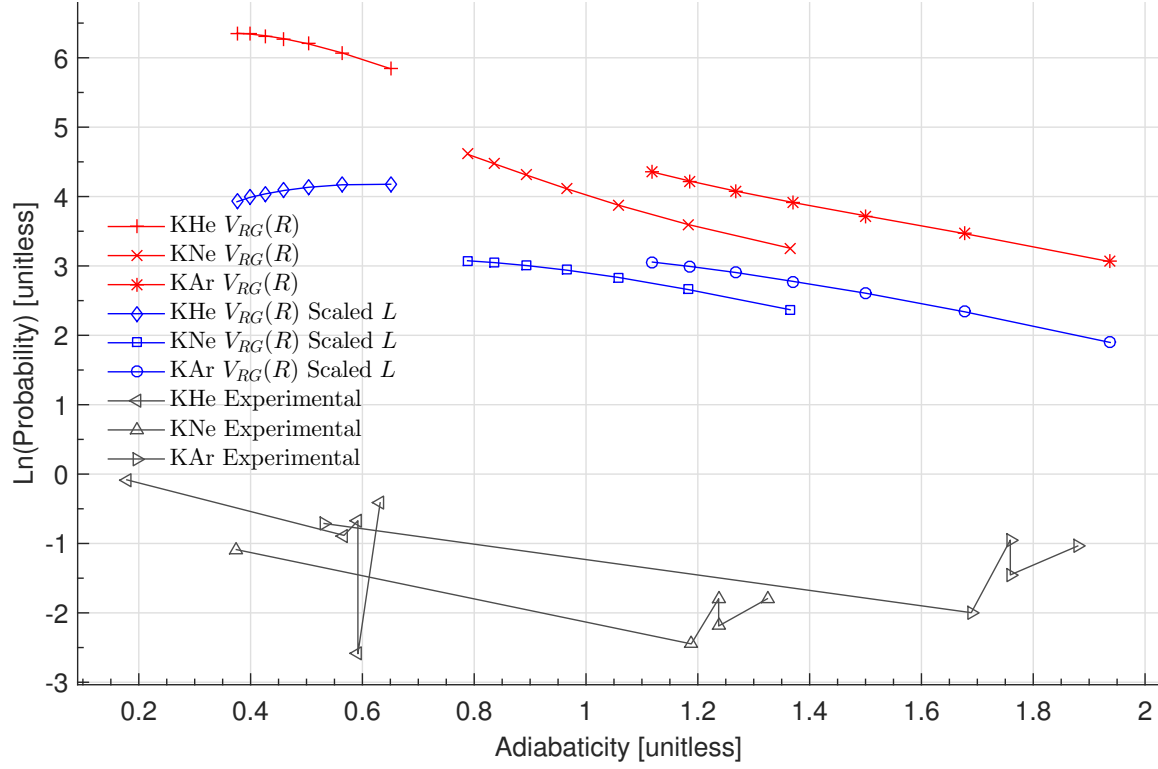


Figure 38. Scaled $V_{RG}(R)$ radial coupling fit parameter, L , for KHe, KNe, and KAr. Experimental data is plotted for comparison. L is scaled by a factor of 0.03.

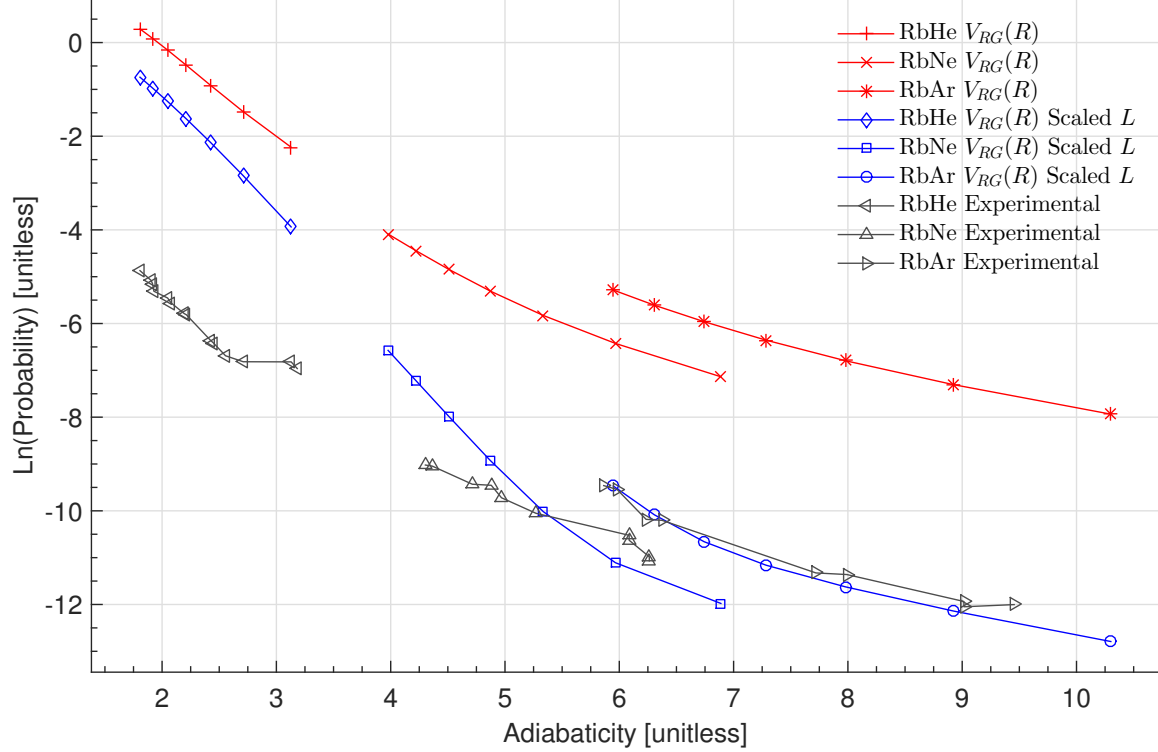


Figure 39. Scaled $V_{RG}(R)$ radial coupling fit parameter, L , for RbHe, RbNe, and RbAr. Experimental data is plotted for comparison. L is scaled by a factor of 0.03.

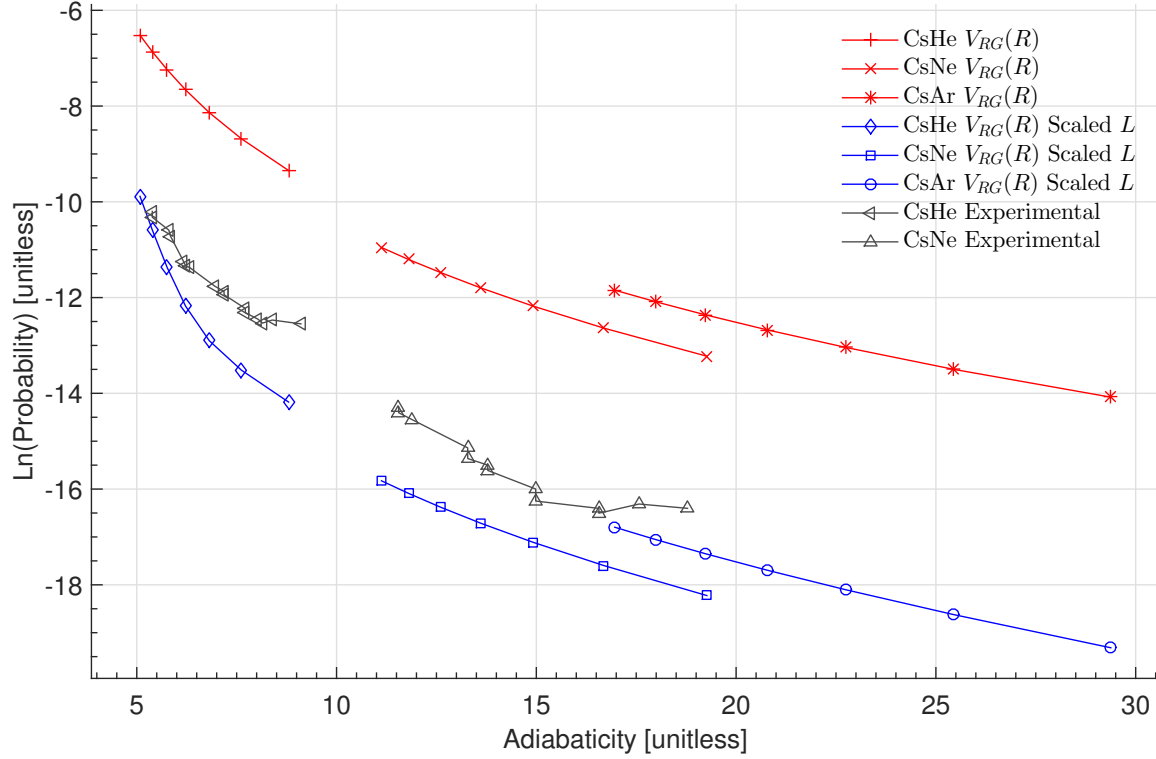


Figure 40. Scaled $V_{RG}(R)$ radial coupling fit parameter, L , for CsHe, CsNe, and CsAr. Experimental data is plotted for comparison. L is scaled by a factor of 0.03.

of L . The combined results for all M+Ng pairs are shown in Figure 46. The scaled radial coupling function is shown in Figure 42.

It is very interesting to note that different scale factors shift the transition probabilities of specific elements by different amounts, depending on the temperature (and therefore depending on the adiabaticity). This means that it should be possible to fit the predicted transition probabilities across a range of temperature (and adiabaticity) values, rather than just attempting to minimize an average error. This is currently easier said than done, due to the fact that the best-fit scale factors are currently found through guessing a value, performing a test run, checking the results, and then making another guess until the fit is satisfactory. Having the analytic approximation of $V_{RG}(t)$ may make this task easier.

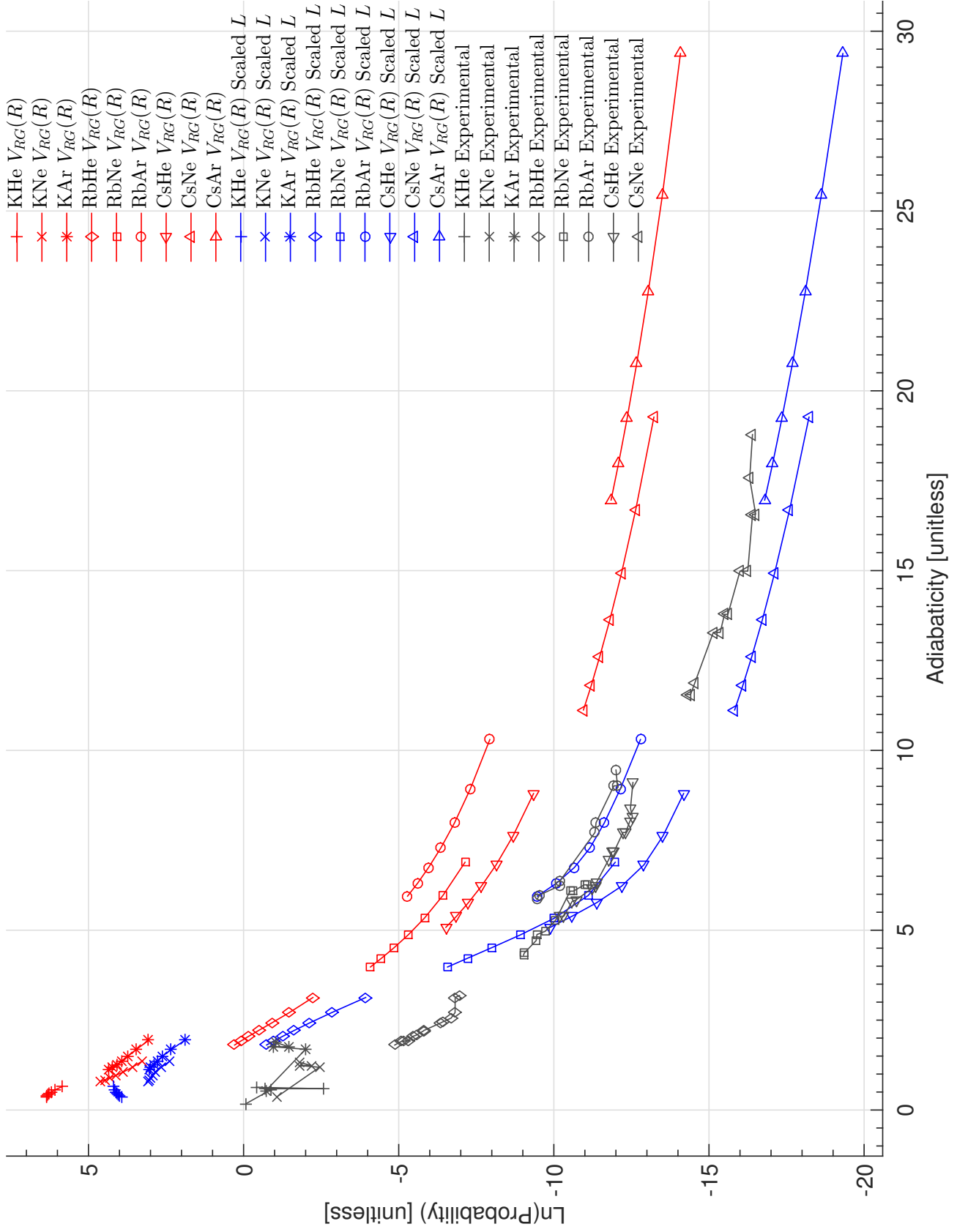


Figure 41. Scaled $V_{RG}(R)$ radial coupling fit parameter, L , for all M+Ng pairs. Experimental data is plotted for comparison. L is scaled by a factor of 0.03.

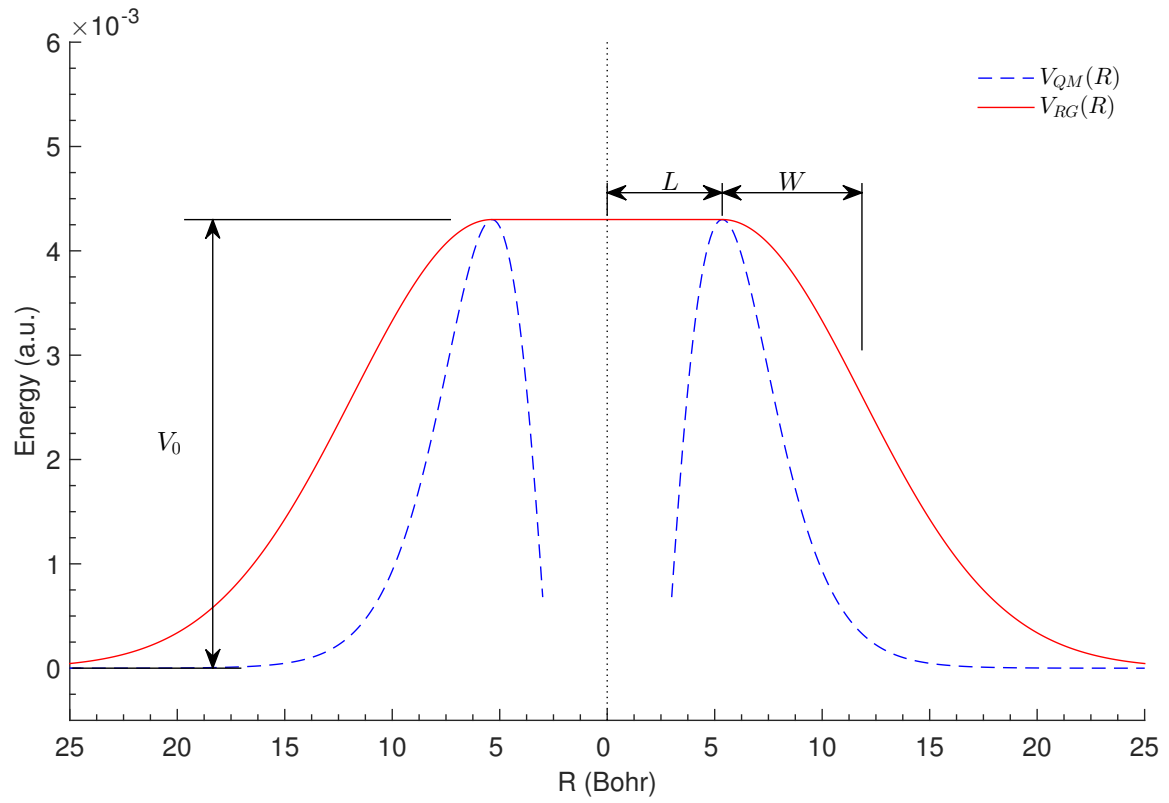


Figure 42. $V_{RG}(R)$ radial coupling function with fit parameter, W , scaled by a factor of 2.6. Data is shown for RbHe, and $V_{QM}(R)$ is plotted for comparison.

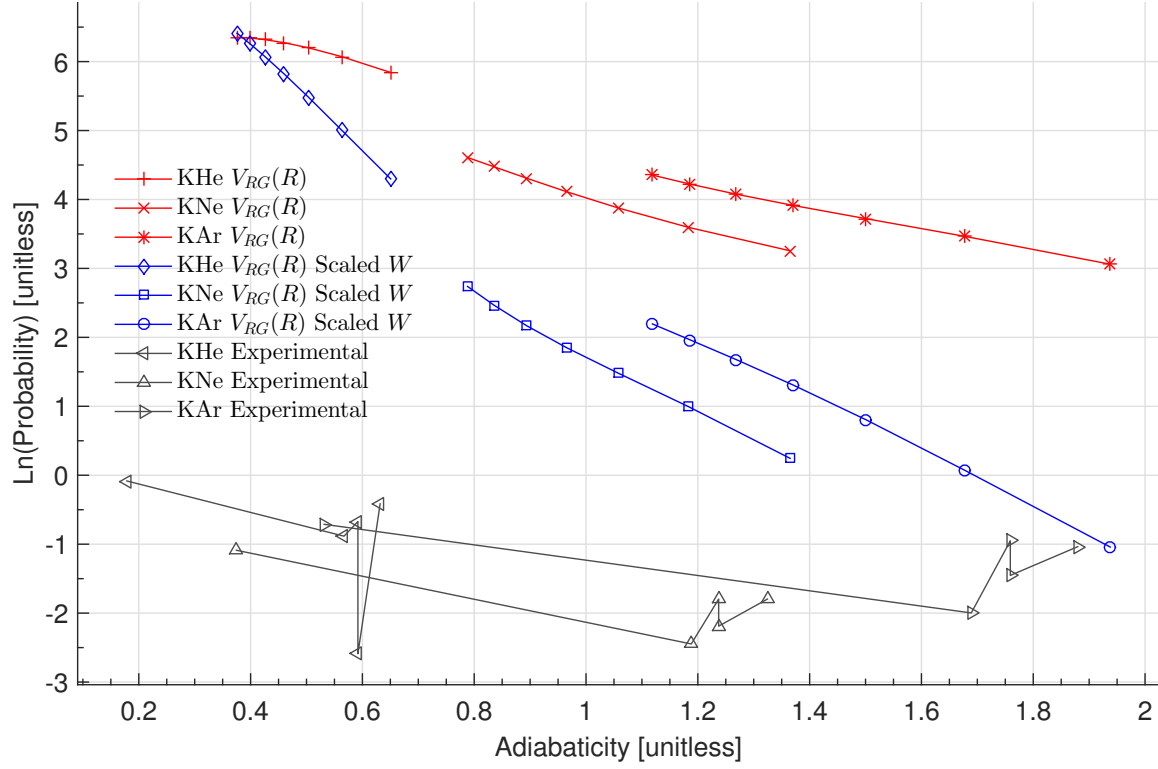


Figure 43. Scaled $V_{RG}(R)$ radial coupling fit parameter, W , for KHe, KNe, and KAr. Experimental data is plotted for comparison. W is scaled by a factor of 2.6.

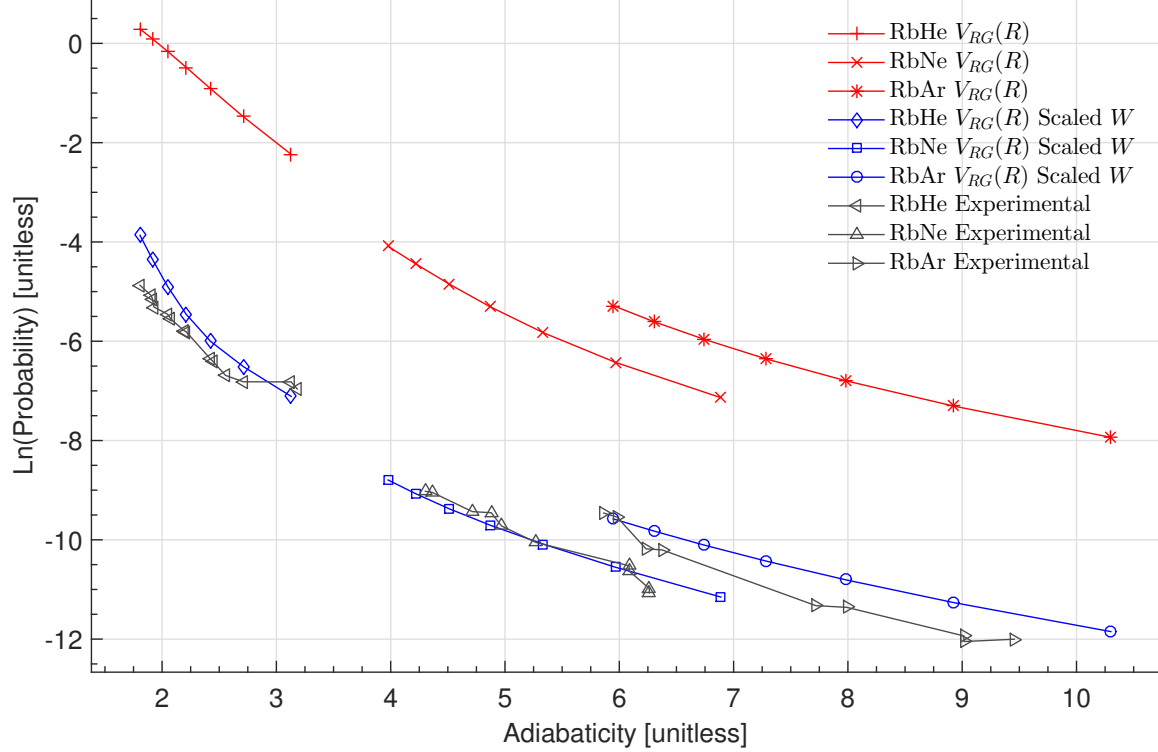


Figure 44. Scaled $V_{RG}(R)$ radial coupling fit parameter, W , for RbHe, RbNe, and RbAr. Experimental data is plotted for comparison. W is scaled by a factor of 2.6.

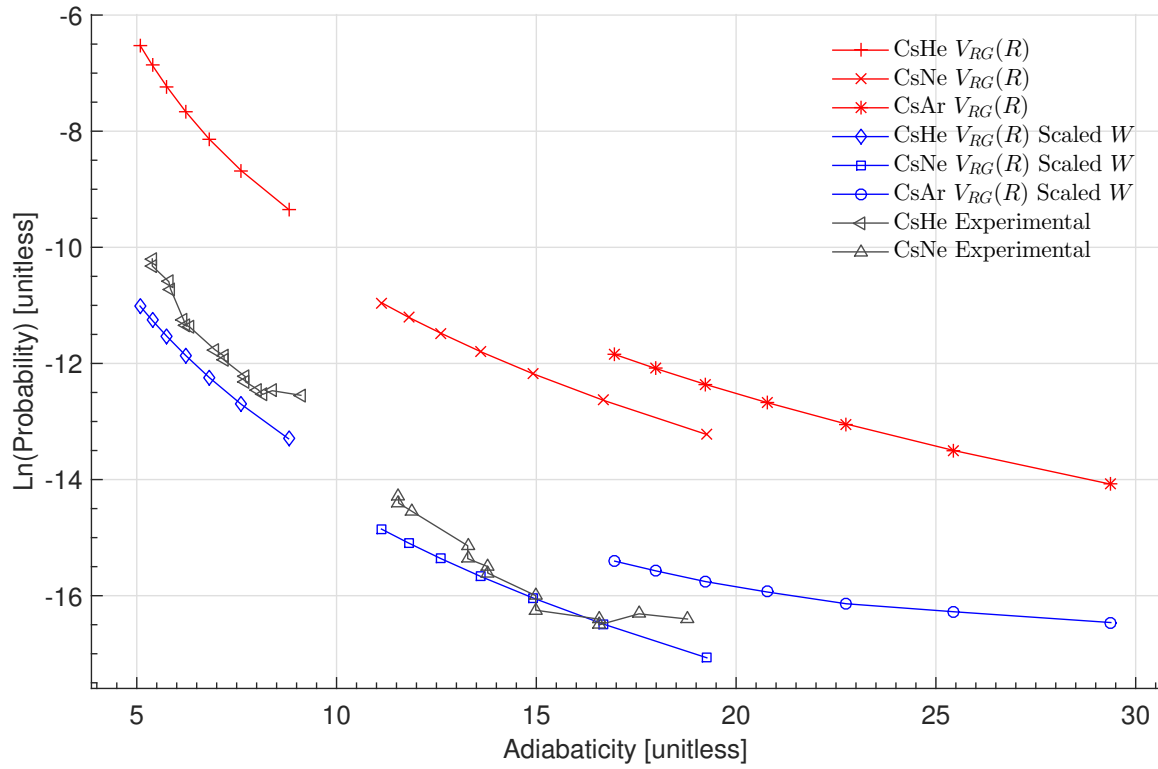


Figure 45. Scaled $V_{RG}(R)$ radial coupling fit parameter, W , for CsHe, CsNe, and CsAr. Experimental data is plotted for comparison. W is scaled by a factor of 2.6.

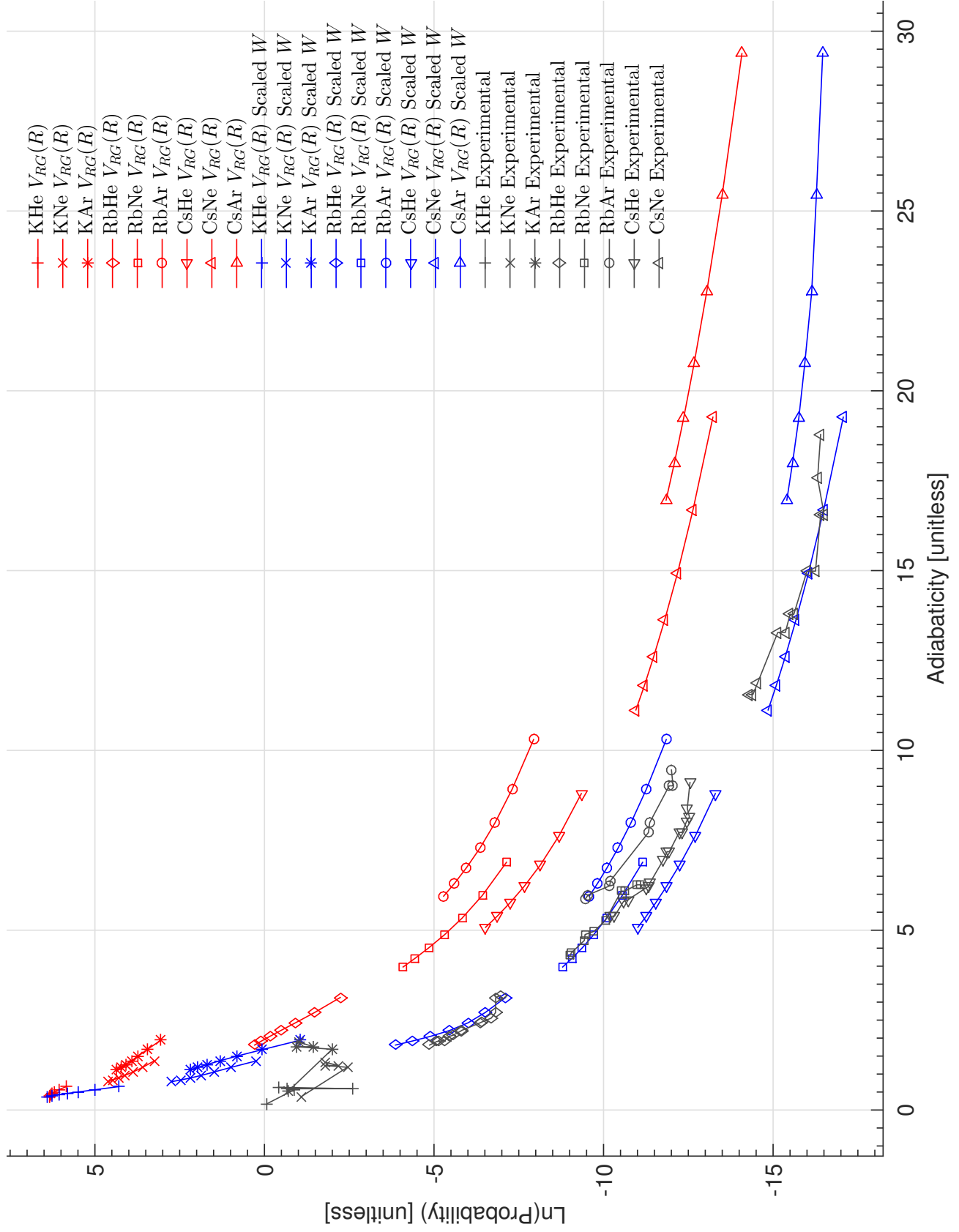


Figure 46. Scaled $V_{RG}(R)$ radial coupling fit parameter, W , for all M+Ng pairs. Experimental data is plotted for comparison. W is scaled by a factor of 2.6.

VI. Conclusion

6.1 Conclusion

There are a few observations that stand out from the results of the calculations based on the semi-classical model presented in this thesis. One of the disappointing observations is that the calculations using the semi-classical model are off by an offset ranging from about $e^3 \approx 20$ (using $V_{RG}(t)$) to $e^8 \approx 3,000$ (using $V_{QM}(R)$), as shown in Figure 47. Another troubling observation is that some of the probabilities for the lighter elements are well above 1, which is of course mathematically nonsense (KHe using $V_{RG}(t)$ is the worst, with a probability of ≈ 500).

Some of the more promising observations include the fact that all of the methods of calculation that were presented in this thesis have the same general curve of $\text{Ln}(\text{Probability})$ vs. Adiabaticity. Another positive observation is that calculations using the analytical approximation of the probability integral match the numerical calculations with $V_{RG}(t)$ very well, supplying cross-validation for both methods. The analytic approximation offers the huge benefit of being able to make quick modifications to the radial coupling function's fit parameters in Mathematica, and having the results show up almost instantaneously. Next, the calculations using $V_{RG}(t)$ match fairly well with calculations using $V_{RG}(R)$. The approximations made in converting $V_{RG}(R)$ to $V_{RG}(t)$ appear to only result in a relatively small offset, without having any significant effect on the shape of the probability curve. The use of the quantum mechanical coupling functions $V_{QM}(R)$, actually introduced a much larger error offset as compared to the rectangular-Gaussian approximations. This may have been due to the different implementation used for this set of coupling functions, namely the energy conservation requirement which was necessary to overcome the difficulty of not having data for $R < 3$ [au]. Adding energy conservation equates with remov-

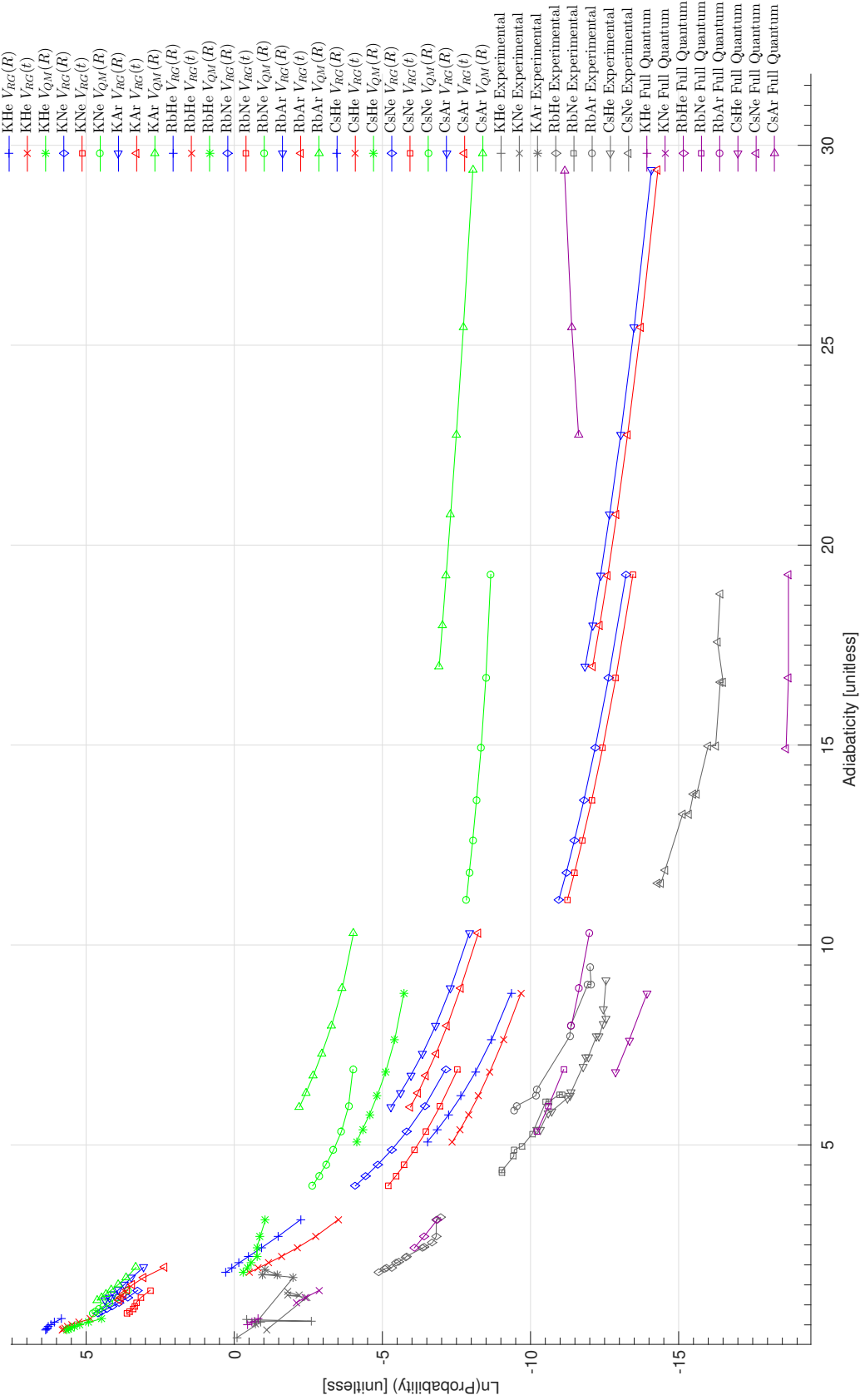


Figure 47. Log(Probability) vs Adiabaticity, raw results for all atomic species (no scaling), along with available experimental data.

ing an approximation, and would therefore be expected to result in a more accurate solution. Getting a less accurate solution, as was seen when comparing the results to experiment data, seems counterintuitive. The radial coupling functions, $V_{QM}(R)$, themselves appear to be validated, at least for potassium and rubidium, through quantum mechanical calculations of temperature-dependent cross sections which were converted to probabilities using the quantum-defect cross sections.

An important thing to note is that the results appear to be very sensitive to the shape of the radial coupling function, V . An area of further research could be to investigate the effect of different trajectories, which would effectively be changing the shape of $V(R(t))$. In its current form, the C code developed for this thesis is able to perform calculations on any of the nine M+Ng pairs presented here within ten minutes on a standard desktop computer, with calculations on some pairs taking only seconds. The code is fairly modular, with $V(R)$ and $R(b, v, t)$ being separate functions. It would be fairly straightforward to introduce different forms of V or R into this code, but care must be taken if the form of V used is no longer an even function. Approximations were made assuming that V was even, as described in Section III.

Bibliography

1. Blank, L, D. E. Weeks, and G. S. Kedziora. “M+Ng potential energy curves including spin-orbit coupling for M = K, Rb, Cs and Ng = He, Ne, Ar”. *Journal of Chemical Physics*, 2012.
2. Curtis F. Gerald and, Patrick O. Wheatley. *Applied Numerical Analysis*. Pearson Education Inc., 7th edition edition, 2004.
3. Eshel, Ben, David E. Weeks, and Glen P. Perram. “The role of adiabaticity in alkali atom fine structure mixing”. *SPIE LASE*, 896207–896207. International Society for Optics and Photonics, 2014.
4. Griffiths, David J. *Introduction to Quantum Mechanics*. Pearson Education, Inc., 2nd edition, 2005.
5. Lewis, Charlton D. *Non-Adiabatic Atomic Transitions: Computational Cross Section Calculations of Alkali Metal - Noble Gas Collisions*. Ph.D. thesis, Air Force Institute of Technology, September 2011.
6. Oppenheim, Alan V. and Ronald W. Schaffer. *Discrete Time Signal Processing*. Pearson Education Inc., 3rd edition edition, 2010.
7. Press, William H., Saul A. Teukolsky, William T. Vetterling, and Brian P. Flannery. *Numerical Recipes in C*. Cambridge University Press, 2nd edition edition, 2002.
8. Weeks, David E. “Fine Structure Transition Probability for M+Ng Collision using the Interaction Function Approximation $V(t)$ ”. Unpublished Notes.

REPORT DOCUMENTATION PAGE

Form Approved
OMB No. 0704-0188

The public reporting burden for this collection of information is estimated to average 1 hour per response, including the time for reviewing instructions, searching existing data sources, gathering and maintaining the data needed, and completing and reviewing the collection of information. Send comments regarding this burden estimate or any other aspect of this collection of information, including suggestions for reducing this burden to Department of Defense, Washington Headquarters Services, Directorate for Information Operations and Reports (0704-0188), 1215 Jefferson Davis Highway, Suite 1204, Arlington, VA 22202-4302. Respondents should be aware that notwithstanding any other provision of law, no person shall be subject to any penalty for failing to comply with a collection of information if it does not display a currently valid OMB control number. **PLEASE DO NOT RETURN YOUR FORM TO THE ABOVE ADDRESS.**

1. REPORT DATE (DD-MM-YYYY) 26-03-2015			2. REPORT TYPE Master's Thesis		3. DATES COVERED (From — To) Sep 2013 - Mar 2015	
4. TITLE AND SUBTITLE A Simple Model for Fine Structure Transitions in Alkali-Metal Noble-Gas Collisions					5a. CONTRACT NUMBER	
					5b. GRANT NUMBER	
					5c. PROGRAM ELEMENT NUMBER	
6. AUTHOR(S) Cardoza, Joseph A., Captain, USAF					5d. PROJECT NUMBER	
					5e. TASK NUMBER	
					5f. WORK UNIT NUMBER	
7. PERFORMING ORGANIZATION NAME(S) AND ADDRESS(ES) Air Force Institute of Technology Graduate School of Engineering and Management (AFIT/EN) 2950 Hobson Way WPAFB OH 45433-7765					8. PERFORMING ORGANIZATION REPORT NUMBER AFIT-ENP-MS-15-M-079	
9. SPONSORING / MONITORING AGENCY NAME(S) AND ADDRESS(ES) High-Energy Laser Joint Technology Office 801 University Blvd Se Ste 209 Albuquerque, NM 87106 505-248-8208, Harro.Ackerman@jto.hpc.mil					10. SPONSOR/MONITOR'S ACRONYM(S) HEL JTO	
					11. SPONSOR/MONITOR'S REPORT NUMBER(S)	
12. DISTRIBUTION / AVAILABILITY STATEMENT DISTRIBUTION STATEMENT A: APPROVED FOR PUBLIC RELEASE; DISTRIBUTION UNLIMITED.						
13. SUPPLEMENTARY NOTES This work is declared a work of the U.S. Government and is not subject to copyright protection in the United States.						
14. ABSTRACT From ranging and tracking applications, to directed energy weapons, laser technology is very important to the military. An instrumental part of laser design and characterization depends on knowledge of transition rates between various atomic energy levels. Of specific interest, is determining the transition probabilities between the $^2P_{3/2}$ and $^2P_{1/2}$ energy levels of an alkali-metal noble-gas laser, which is found in a DPAL. The probabilities of transition, caused by collisions between alkali metal and noble gas atoms, have previously been calculated using a computationally intensive quantum mechanical model. This research project aims to develop a simplified, less intensive method. This is accomplished through the use of a semi-classical approach, where the colliding atoms are modeled as having a classical, straight-line trajectory. The transition probabilities are then calculated using time-dependent perturbation theory, where the coupling between states is obtained by expressing the diabatic coupling potential as a function of time. Numerical solutions to the time-dependent perturbation equations are obtained for various forms of coupling and are compared with an approximate analytic solution.						
15. SUBJECT TERMS Atomic Transition Rates, Alkali-Metal Noble-Gas Collisions						
16. SECURITY CLASSIFICATION OF:			17. LIMITATION OF ABSTRACT	18. NUMBER OF PAGES	19a. NAME OF RESPONSIBLE PERSON	
a. REPORT	b. ABSTRACT	c. THIS PAGE			Dr. David E. Weeks (ENP)	
U	U	U	U	92	19b. TELEPHONE NUMBER (include area code) (937)255-3636 x4561; david.weeks@afit.edu	